RSC Advances

ROYAL SOCIETY OF CHEMISTRY

www.rsc.org/advances

Zinc oxide based photocatalysis: tailoring surface-bulk structure and related interfacial charge carrier dynamics for better environmental applications

S. Girish Kumar and K. S. R. Koteswara Rao*

Department of Physics, Indian Institute of Science, Bangalore-560012, Karnataka, India

E-mail: raoksrk@gmail.com; ksrkrao@physics.iisc.ernet.in

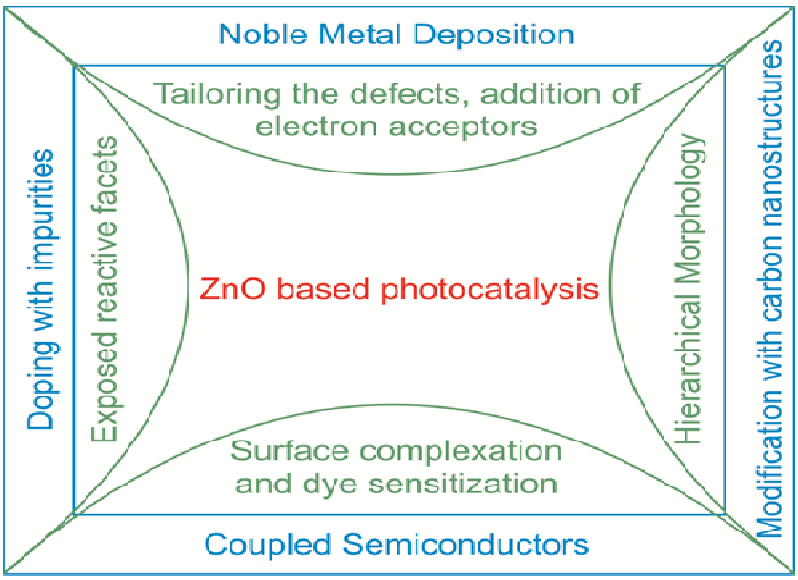

Surface-bulk modification of zinc oxide for efficient photocatalysis

Zinc oxide based photocatalysis: tailoring surface-bulk structure and related interfacial charge carrier dynamics for better environmental applications

S. Girish Kumar and K. S. R. Koteswara Rao*

Department of Physics, Indian Institute of Science, Bangalore-560012, Karnataka, India

e-mail: raoksrk@gmail.com; ksrkrao@physics.iisc.ernet.in

Abstract

As an alternative to the gold standard TiO_2 photocatalyst, the zinc oxide (ZnO) signature as a robust candidate for the wastewater treatment is widespread due to their similarity in charge carrier dynamics upon bandgap excitation and generation of reactive oxygen species in aqueous suspensions with TiO_2. However, the large bandgap of ZnO, massive charge carrier recombination, and the photoinduced corrosion-dissolution at extreme pH conditions together with the formation of inert $Zn(OH)_2$ during the photocatalytic reactions remains as a barrier for its extensive applicability. To this end, the research is intensified to improve the performance of ZnO by tailoring the surface-bulk structure and to alter the photogenerated charge transfer pathways with an intention to inhibit the surface-bulk charge carrier recombination. For the first time, several strategies like, tailoring the intrinsic defects, surface modification with organic compounds, doping with foreign ions, noble metal deposition, heterostructuring with other semiconductors and modification with carbon nanostructures that are successfully employed to improve the photoactivity and stability of ZnO is critically reviewed. Such a modification enhances the charge separation and facilitates the generation of reactive oxygenated free radicals, and also its interaction with the pollutant molecules. The synthetic route to obtain hierarchical nanostructured morphologies and their impact on the photocatalytic performance is explained taking into consideration, the morphological influence and the defect rich chemistry of ZnO.

Finally, the crystal facet engineering of polar and nonpolar facets and their relevance in photocatalysis is outlined. It is with this intention that the review directs further design, tailor and to tune the physicochemical and optoelectronic properties of ZnO for better applications ranging from photocatalysis to photovoltaics.

Acronyms

Aluminium doped ZnO	AZO	Nanoparticle(s)	NP(s)
Carbon nanofibers	CNFs	Nanorod(s)	NR(s)
Carbon nanotubes	CNTs	Nanosheets	NS
Carbon quantum Dots	CQDs	Nanotube(s)	NT(s)
4-chlorophenol	4-CP	Nanowire(s)	NW(s)
Conduction band	CB	4-nitrophenol	4-NP
Conduction band offset	ΔE_c	Orange G	OG
Critical micelle concentration	CMC	Photoluminescence	PL
Crystal violet	CV	Polyaniline	PANI
2,4-dichlorophenol	DCP	Polyvinylpyrrolidone	PVP
N,N-dimethylformamide	DMF	Premicelle concentration	PMC
Electrochemical impedance spectroscopy	EIS	Reduced graphene oxide	RGO
Energy dispersive X-ray spectroscopy	EDS	Rhodamine B	RhB
Ethylenediaminetetraacetic acid	EDTA	Rhodamine 6G	R6G
Ethylene glycol	EG	Salicylic acid	SA
Ethyl violet	EV	Scanning electron microscopy	SEM
Fluorine doped tin oxide	FTO	Sulfur mustard	HD
Fluorescence spectroscopy	FS	Tetrapods	TPs
Functionalized graphene sheets	FGS	*t*-butyl alcohol	TBA
Graphene oxide	GO	*t*-butylphosphonic acid	TBPA
Hexadecylamine	HCA	2,4,6-trichlorophenol	TCP
Hexamethylenetetramine	HMT	Triethanol amine	TEA
Highest occupied molecular orbital	HOMO	Tetraethylammonium hydroxide	TEAOH
Internal electric field	IEF	Tetrahydrofuran	THF
Lowest unoccupied molecular orbital	LUMO	Transmission electron microscopy	TEM
Malachite Green	MG	Tetramethylammonium hydroxide	TMAOH
Mars–Van Krevelen	MVK	Valence band	VB
Methylene blue	MB	Valence band offset	ΔE_v
Methyl orange	MO	Water contact angle	WCA
Methyl red	MR	X-ray photoelectron spectroscopy	XPS
Monocrotophos	MCP	Zinc-ehtylene glycol-acetate	Zn-EG-AC
Multiwalled carbon nanotubes	MWCNTs	Zinc oxide nanowires	ZNWs
Nanorod arrays	NRA	Zero point charge	ZPC
Nanofiber(s)	NF(s)		

1.0 Introduction

Clean energy and pollutant free water/air are the important tasks that we currently face, with a common solution that lies in the design and development of multifunctional nanomaterials for harvesting a maximum light energy from the solar light. Since, environmental pollution has surpassed the threshold of natural purification, an advanced oxidation process seems to be the most effective futuristic waste water treatment methods with high efficiency and low cost. Besides the photo Fenton process,[1-4] the semiconductor photocatalysis as a *'green approach'* is at the forefront in terms of fundamental research and for their technological applications due to its non-selectivity, low temperature and non-energy intensive approach for the complete mineralization of pollutants. The photoinduced charge carrier separation upon bandgap excitation of semiconductors is vital to drive redox reactions and followed by its transfer to solution-phase redox couples is essential to accelerate the overall photocatalytic reaction rates. From the view point of thermodynamics, redox potential of the VB-hole must be positive to generate hydroxyl radicals, and the CB-electron must be negative to inititate dioxygen reduction.[5] As an alternative to the illustrious semiconductors like TiO_2, WO_3, Bi_2O_3, Fe_2O_3, BiOX (X=Cl, Br & I) and $(BiO)_2CO_3$, the ZnO is recently in the spotlight of research efforts due to its stupendous benefits such as low cost and high quantum efficiency as well as a favourable bandgap and the photocatalytic mechanisms.[6-15] The admirable attributes of ZnO such as mechanical-thermal stability, high photosensitivity, inexpensiveness, high redox potential, large bandgap offering an excellent driving force to induce redox reactions, non toxicity, versatility in synthesis with hierarchical morphology, availability of different precursors (common inorganic salts) and their high solubility in various solvents, ease of crystallization, anisotropic growth, and natural abundance manifests its scope in the photocatalysis. The refractive index of ZnO (2.0) is

smaller than TiO_2 (2.5 – 2.7) and hence ZnO scarcely scatters light, thereby making it colorless and boost the transparency. Also, ZnO photocatalyzed reactions are best performed at neutral pH conditions, which is an added merit over its competitors. Furthermore, the emission properties of ZnO have made possible to set up an original catalytic system able to *'sense and shoot'* the environmental contaminants, thus motivating further exploration on the properties of ZnO.[16]

Due to the presence of intrinsic impurities, electron mobility (200 – 300 $cm^2V^{-1}s^{-1}$) and electron lifetime (> 10 s) of ZnO is much higher compared to TiO_2 (0.1 – 4.0 $cm^2V^{-1}s^{-1}$) which reduces the electrical resistance and promotes the electron transfer efficiency.[17-18] Thus, high concentration of photogenerated charge carriers transfer to the surface contributes to an efficient photocatalysis. In addition, the VB of ZnO is positioned slightly below TiO_2 VB, indicating that the hydroxyl radical generated in the former (+3.06 V) has a high oxidation potential compared to the latter (+2.7 V) and the electron derived from the ZnO CB is believed to be more negative than TiO_2 (at pH 0 *vs.* NHE), while the CB edges of both the semiconductors are almost same at neutral pH condition (-0.5 V *vs.* NHE).[19-20] The ZnO absorbs a large fraction of UV spectrum and more light quanta, exhibiting a better performance compared to TiO_2 for pollutant treatment under the light illumination.[21-26] The surface band of ZnO is upward bent in air, indicating that its built in electric field direction is from inner to outer facilitating the hole migration to particle surface, while electrons diffuse to the bulk of particle.[27] The defects like oxygen vacancies, zinc interstitials, oxygen interstitials, and generation of hydrogen peroxide, superoxide and hydroxyl radicals on the ZnO surface are reported to be responsible for photocatalytic activity.[28-33] Although, different radicals/defects mediate the degradation mechanism depending on the surface-bulk modification of ZnO, it is unambiogously accepted that a low degree of charge carrier recombination is vital to achieve a high photocatalytic efficiency.

ZnO crystallizes commonly in a wurtzite structure (space group *P6₃mc*, a=3.25 Å, c=5.20 Å) with n-type conductivity ($Zn_{1+\sigma}O$, $\sigma>0$) having a direct bandgap of 3.37 eV with large excitonic binding energy (60 meV), which is even larger than the thermal energy at RT.[28-33] The specific physicochemical, optoelectronic and magnetic properties of ZnO stimulates its feasible application in various disciplines such as photocatalysis, light emitting diodes, solar cells, gas sensors, pyroelectricity, luminescent materials, pigments, UV shielding materials, surface acoustic wave filters, actuators, spin electronics, short-wavelength optoelectronic devices, varistors, antifungal, and piezodielectric nanogenerators.[34-39]

Despite the versatility, ZnO based photocatalysis attrite of endemic reasons: (i) ZnO do not absorb the visible portion of solar spectrum demanding an expensive UV light for bandgap excitation; (ii) a rapid recombination of charge carriers inevitably obstruct the outward diffusion of charge carriers and consequently slow down the degradation reactions occurring at the semiconductor-liquid interface; (iii) the problems associated with the recovery of ZnO powder from the suspension by the conventional filtration; (iv) the tendency to aggregate during the catalytic reactions and the susceptible to corrosion under UV light. The photocorrosion reactions can be represented as:[40-41]

$$ZnO + 2h^+ + nH_2O \rightarrow Zn(OH)_n^{(2-n)+} + 1/2\,O_2 + nH^+ \qquad (1)$$

where, ‘n’ depends on the pH of the solution. The photodissolution of ZnO initially involves the hole trapping on the surface, followed by a rapid formation of oxygen molecule and fast expulsion of Zn^{2+} from the surface.

$$O^{2-}{}_{surface} + h^+ \rightarrow O^-{}_{surface} \quad (2)$$

$$O^-{}_{surface} + 3O^{2-} + 3h^+ \rightarrow 2(O - O^{2-}) \quad (3)$$

$$O - O^{2-} + 2h^+ \rightarrow O_2 \quad (4)$$

$$2Zn^{2+} \rightarrow 2Zn^{2+}\ (aqueous) \quad (5)$$

The overall reaction can be represented as

$$ZnO + 2h^+ \rightarrow Zn^{2+} + 1/2\ O_2 \quad (6)$$

In addition, the ZnO powder dissolves at strong acidic pH:

$$ZnO + 2H^+ \rightarrow Zn^{2+} + H_2O \quad (7)$$

Under strong alkaline medium, ZnO can undergo dissolution:

$$ZnO + H_2O + 2OH^- \rightarrow Zn(OH)_4^{2-} \quad (8)$$

ZnO passivates to form an inert $Zn(OH)_2$ surface layers upon the UV illumination;

$$2ZnO + 4H_2O + 4h^+ \rightarrow 2Zn(OH)_2 + O_2 + 4H^+ \quad (9)$$

Thus, both strong acidic and alkaline pH may not favour the photocatalytic process.

To overcome these aforementioned obstacles, research is at the rapid pace in modifying the surface-electronic structure of ZnO that largely involves altering the ZnO defect chemistry to benefit photocatalysis under the ambient conditions. Many insightful review articles are concentrated on the synthesis, properties, growth, defects, and other applications of ZnO.[42-47] In contrast, a few seminal review articles associated to the photocatalysis discusses on the effects of an initial reaction parameters like catalyst dosage, concentration of the dye, solution pH and the presence of electron acceptors with a brief approach to afford the visible light response for ZnO.[48-51] Inspired by the advances with interesting and exciting results, the authors have taken up this review on the research progress of ZnO based photocatalysis to pave the way for its

practical applications. The interfacial charge carrier transfer dynamics in each strategies correlating to high activity of modified ZnO are discussed in the light of material properties like catalyst dosage, surface charge density, crystallinity, defects (intrinsic and extrinsic), properties of modifiers, charge carrier generation-separation-recombination dynamics, together with experimental conditions constituting the pollutant structure, pH of the solution, presence of inorganic electrolytes, intensity and wavelength of the excitation source. For the first time, defect-facet-morphological dependence of ZnO on photocatalytic activity is also highlighted.

Footnote to page 8: (i) the excitation source for all those references/ literature dealing with UV light photocatalysis is not mentioned in this review article, for clarity; (ii) UV/visible light indicate that the photocatalytic activity dealt with both UV and visible light illumination; (iii) UV-vis implies that the excitation source used has the emission wavelength in both UV and visible region.

2.0 Fundamental aspects of ZnO based photocatalysis

The underlying mechanism of the photocatalysis comprises the bandgap excitation of ZnO with energetic photons generating exciton pair with holes in the VB and electrons in the CB. These charge carriers may recombine dissipating the input energy as heat or undergoes interfacial charge transfer process either by trapping at metastable surface states or interacts with preadsorbed electron donors/acceptors on the catalyst surface or within the surrounding electrical double layer of charged particles.[7,52-53]

(a) surface sensitization and complexation of ZnO

Microscale ZnO decomposed dyes like CV, MB, OG and MO at a faster rate compared to Degussa P25 under UV-visible light, indicating that the photosensitization of ZnO by dyes

favoured the visible light response with an enhanced charge carrier separation.[54] The excited dye molecule transfers electrons to the ZnO CB, while dye itself converts to cationic radical. The injected electron reacts with dioxygen adsorbed on the ZnO surface to generate a series of active oxygen species, which on the subsequent reaction with the dye molecules results in the degradation.[55-56]

$$\text{Dye} + \text{visible light} \rightarrow \text{Dye}^{*} \quad (10)$$

$$\text{Dye}^{*} + \text{ZnO} \rightarrow \text{Dye}^{\cdot+} + \text{ZnO}(e^{-}) \quad (11)$$

$$\text{ZnO}(e^{-}) + O_2 \rightarrow O_2^{-\cdot} \quad (12)$$

$$O_2^{-\cdot} \xrightarrow{H^{+}} \rightarrow\rightarrow HO_2^{\cdot} + HO^{\cdot} \quad (13)$$

$$\text{Dye}^{\cdot+} + \text{reactive oxygenated radicals} \rightarrow \text{products} \quad (14)$$

In addition, the light to electricity conversion efficiency of 0.23% was obtained for ZnO based dye sensitized solar cells compared to Degussa P25 (0.0024%) counterpart. This is an important report to realize simultaneously both dye degradation and the generation of renewable energy source. The ZnO sensitized heteroaggregate (CoTPPS+TAPPI) was efficient for RhB degradation under the visible light compared to ZnO-CoTPPS, ZnO-TAPPI and ZnO.[57] The heteroaggregates formed by intermolecular electrostatic force of attraction between positively charged TAAPI {tetrakis(4-trimethylaminophyenyl) porphyrin} and negatively charged CoTPPS {tetrakis(4-sulfonatophenyl) porphyrin cobalt (II)} extends the composite absorption into a wider spectral range compared to porphyrin monomer. The loading of water soluble porphyrin enhances the hydrophilic character of ZnO microrods facilitating its dispersion in the aqueous solution. In addition, the redox potentials of heteroaggregates align with the energy level of ZnO to promote an electron injection from excited state of porphyrin into the ZnO CB and suppress the carrier recombination.[57] In the sensitization process, electron transfer and recombination

between sensitizer and ZnO together with their redox potentials govern the kinetics of electron injection.

Kamat *et al.*[16] reported *'sense and shoot'* approach by monitoring the quenching of relative emission intensity of ZnO with the organic compounds like 4-chlorocatechol, catechol and 4-CP. These phenolic compounds scavenge the photogenerated holes and compete with the charge carrier recombination that is responsible for the emission properties (Fig. 1). Surprisingly, the original emission was restored following the exposure of the film to deionized water indicating the interaction between ZnO and phenolic compounds was purely physisorption. The varying degree of emission quenching for these compounds arises from differences in the adsorption and their ability to scavenge holes on the ZnO surface. The experimental illustration of increased emission during photocatalysis confirms that the emission recovery was purely associated with the degradation of aromatic intermediates in aqueous solution. In comparison to TiO_2, surface complexation of 4-CP on the ZnO surface *via* -Zn-O-Ph-Cl linkage extended the photoresponse to visible range and accelerated the degradation rate of 4-CP.[58] The PL studies indicated a slight decrease of visible emission, suggesting the surface complex are formed mainly on the defect sites (oxygen vacancies), that improved the photostability of ZnO. This surface complex is formed *via* condensation reaction;

$$-Zn-OH-+OH-Ph-Cl \rightarrow -Zn-O-Ph-Cl+H_2O \qquad (15)$$

Unlike the conventional dye sensitization process, visible light irradiation of the above surface complex excite the electron directly from the ground state of the adsorbate to ZnO CB through ligand to metal charge transfer process, provided there exists a significant electronic coupling between the adsorbate orbitals and Zn 'd' orbitals. The similar complexation and degradation pathways for DCP and phenol was noticed under the visible light.[58] The acetate capped ZnO

crystals (h-ZnO) promoted the degradation of MO and MR at pH 6 but was susceptible to corrosion at extreme pH conditions.[59] In contrast, HCA/ TBPA capped ZnO (nh-ZnO) showed a weaker pH dependence for degradation and high resistance to photocorrosion attributed to its hydrophobic nature. The phosphonic acid bonds to ZnO surface strongly *via* bi/tri dentate geometry, as opposed to an acetate ligand, which anchors weakly *via* unidentate fashion. Thus, the high density of surface sites is expected to be passivated by HCA or TBPA resulting in lower activity. In addition, the long alkyl chain can impose significant barrier towards the adsorption of target molecules. The intermediates formed during the degradation were retarded to a large extent on nh-ZnO surface compared to h-ZnO.[59] The activity of colloidal ZnO for MO degradation at various calcination temperatures followed an order: 150 > 300 > 500 ˚C in correlation with monodentate, bidentate capped and the free acetate group respectively. With an increase in calcination temperature, the acetate group decomposes and leads to a larger particle size with a loss in photoactivity.[60] The modification of ZnO with Co(II) acetate and trimethylsilanolate inhibited the degradation of 4-NP, attributed to the elimination of defect sites (oxygen vacancies) on ZnO surface that was crucial for a photoactivity.[61] Such surface modification with a suitable reagent could significantly improve the stability of ZnO. The integration of organic and inorganic compounds into the semiconductor NPs is driving to an adventurous new set of nanoscale functional architectures aspiring for enormous applications.

(b) Effect of crystallite size

The efficiency of ZnO synthesized by solvothermal route (80 ˚C for 24 h, followed by calcination at 400 ˚C for 6 h) using TEAOH and methanol showed a high activity for RhB degradation under the visible light compared to the samples prepared with ethanol and propanol solvents (Fig. 2).[62] The crystallite size of ZnO increased with the length of the carbon chain of

the solvent that can be interpreted by considering the dielectric constant of methanol (32), ethanol (25) and propanol (21). In general, the solvent with a low dielectric constant likely to induce faster and uncontrolled precipitation kinetics and also leads to the supersaturation of Zn^{2+} ions due to the lower solubility of zinc salts. This offer the driving force for nucleation and growth of ZnO NPs with reduced nucleation time and higher solid particle growth. The smaller crystallite size with the methanol solvent leads to a larger surface area and quantization in the bandgap facilitates the easy electron injection from excited dye to ZnO CB. Upon replacing TMAOH in synthetic route, crystallinity seems to be overriding factor against the surface area in governing the photocatalysis. The decolorization of MO for a distinct size ZnO followed the order: nanometer (50 nm) > sub micron (200 nm) > micron grade (1000 nm).[63] This tendency was attributed to: (i) the amount of dispersed particles per volume in the reaction solution will increase, consequently improving the photon absorption ability; (ii) an increased surface area promotes the adsorption of the dye molecules on the catalyst surface; (iii) the coupling of exciton pairs will be suppressed. Surprisingly, ZnO with a particle diameter of 10 nm showed lower activity as compared to sub micron sized counterpart. Dodd *et al.*[64] also reported that the optimal size of ~33 nm resulted in the enhanced hydroxyl radical generation, while reducing the particle size (~28 nm) lowered the tendency as a result of increased surface recombination.[65] Casey *et al.*[66] reported that the photoactivity increased significantly by a factor of 2 to 3 as the mean crystallite size was reduced from 100 to 20 nm. The ZnO prepared by precipitation method from zinc acetate, zinc nitrate and zinc sulfate showed a high activity for RhB degradation compared to the sample obtained through citrate method.[67] In the latter case, a two step heat treatment at 300 $^{\circ}$C (4 h) and 500 $^{\circ}$C (or 600 $^{\circ}$C, 2 h) was necessary to remove the organic residues and to induce the crystallization of ZnO respectively, while the former involved a single step of

calcination (500 °C, 2 h) for nitrate or acetate precursor and 800 °C for sulphate precursor. The additional organic residues in the citrate method were originated by the formation of citrate complexes. In contrast, the precipitation method produced a crystalline surface devoid of contaminants, which was beneficial to photocatalysis. The activity of ZnO with respect to a precursor obtained *via* citrate method followed the sequence: zinc acetate > zinc nitrate > zinc sulphate, while those prepared through precipitation method showed almost similar activity. The parameters like the surface area, agglomeration and sintering temperature, which varied with the synthesis route and counter anion of zinc precursor, did not exhibited any influence on the degradation kinetics.[67]

The photoactivity does not increase monotonically with decrease in the particle size in all the cases and the relationship between size dependence and the catalytic efficiency is a close-knit. The proper size is indispensable to balance the specific surface area, crystallinity and the surface-bulk carrier recombination probability, so as to obtain a better performance.

(c) influence of reaction pH, electron acceptors and degradation pathways

The photocatalytic activity for Acid Brown 14 dye degradation under natural solar light with various catalysts followed the order: ZnO > TiO_2 > α-Fe_2O_3 > ZrO_2 > CdS > WO_3 > SnO_2, mainly attributed to the absorption of more light quanta and a large fraction of solar spectrum by ZnO.[68] The photocatalytic oxidation of NO with ZnO-$TiO_{2-x}N_x$ produced NO_2 gas and HNO_3 as major products, while HNO_2 as a minor compound with acids gets adsorbed on the catalyst surface under UV/visible light.[69] The NO_x molecule may react with a superoxide radical to nitrate anion and finally HNO_3 formed deactivates the catalyst surface.

$$NO + 2OH \rightarrow NO_2 + H_2O \quad (16)$$

$$NO_2 + HO^{\bullet} \rightarrow NO_3^- + H^+ \quad (17)$$

$$NO_x + O_2^{-\cdot} \rightarrow NO_3^- \quad (18)$$

The degradation of phenol was favoured in weakly acidic or neutral pH conditions and was effective under the solar light compared to an artificial visible light illumination.[70] The ZPC of ZnO NPs is in the range of 8 – 9 and that the electrical property changes with pH value of dispersion.[71] Hence, the surface charge density will be positive in an acidic or weak basic medium and negative under a strong alkaline condition. In a weak acidic solution, the phenol molecules remain undissociated to deliver a strong adsorption of phenol on the ZnO surface resulting in an efficient degradation. Under alkaline conditions, phenolate intermediates experience an electrostatic repulsion from the ZnO surface resulting in the poor adsorption of pollutant and consequent decline in the degradation rate. It is worth to mention that commercial ZnO supplied from Merck chemicals was less susceptible to photocorrosion and retained its activity even after recycling for five subsequent runs.[70] The degradation and mineralization of SA *via* Langmuir-Hinshelwood mechanism was effective in the neutral pH, attributed to the electrostatic force of attraction between salicylate anion and the positively charged ZnO. A significant loss in activity was observed only after the fifth run of recycling test.[72] The methyl parathion degradation followed a first order kinetics on ZnO and TiO_2 surface, with the latter being more effective in complete mineralization.[73] The optimum catalyst dosage was found to be 200 mgL^{-1} and 500 mgL^{-1} for TiO_2 and ZnO respectively, attributed to the difference in their characteristics such as crystal phase, specific surface area, grain size, density of defects, electron-hole recombination kinetics, charge carrier mobility and the surface acid-base properties. At a lower catalyst dosage, absorption of light controls the photocatalytic process due to the limited

catalyst surface, whereas the aggregation and scattering of light would be detrimental at high catalyst loading. The degradation was enhanced with peroxydisulfate as electron scavenger through the generation of strong oxidizing agent sulfate radical:[74]

$$S_2O_8^{2-} + e^- \rightarrow SO_4^{2-} + SO_4^{-\cdot} \quad (19)$$

$$SO_4^{-\cdot} + e^- \rightarrow SO_4^{2-} \quad (20)$$

$$SO_4^{-\cdot} + H_2O \rightarrow SO_4^{2-} + HO^{\cdot} + H^+ \quad (21)$$

$$SO_4^{-\cdot} + RH \rightarrow ..... \rightarrow SO_4^{2-} + CO_2 \quad (22)$$

The toxicity of the treated solution was reduced with TiO_2, while the release of Zn^{2+} ions as a result of photodissolution increased the toxicity for ZnO. The mineralization studies revealed the absence of phosphate ion due to insoluble $Zn_3(PO_4)_2$ formation, which was otherwise present with the titania dispersion indicating different degradation pathways on these two metal oxides.[73] The degradation of Acid Red 14 was improved in the presence of H_2O_2 at neutral pH under UV-C source (100 – 280 nm), while ethanol addition suppressed the reaction kinetics confirming the hydroxyl radical participation in the degradation mechanism.[20] The H_2O_2 served as better electron acceptor than the dioxygen to trap CB electron at a faster rate or undergoes direct photolysis to produce hydroxyl radicals.[7a]

$$H_2O_2 + h\nu \rightarrow 2OH^{\cdot} \quad (23)$$

$$H_2O_2 + O_2^{-\cdot} \rightarrow OH^{\cdot} + OH^- + O_2 \quad (24)$$

$$H_2O_2 + e^- \rightarrow OH^{\cdot} + OH^- \quad (25)$$

But higher dose of H_2O_2 served as hydroxyl radical scavenger or hole scavenger suppressing the degradation rate. The free radicals may also recombine to form neutral species.

$$H_2O_2 + h^+ \rightarrow O_2H^{\cdot} + H^+ \quad (26)$$

$$H_2O_2 + OH^{\cdot} \rightarrow O_2H^{\cdot} + H_2O \quad (27)$$

$$O_2H^{\cdot} + OH^{\cdot} \rightarrow H_2O + O_2 \quad (28)$$

In contrast, degradation of Acid Red 18 was suppressed with H_2O_2, but accelerated with $(NH_4)_2S_2O_8$ and $KBrO_3$. This unusual decrease was due to low adsorption of H_2O_2 on the ZnO surface.[74c] The degradation of HD proceeded through the formation of byproducts such as thiodiglycol, hemisulfar mustard, divinyl sulfide, 2-chloroethyl vinyl sulfide on the surface of ZnO NPs under the dark and visible light irradiation.[75] However, HD sulfoxide, HD sulfone, 1, 3-dithiane, 2-chloroethanol and CH_3CHO along with the hydrolysis and the elimination products were formed under the sunlight and an UV-A light illumination. In the former case, degradation through elimination and surface complexation reactions played a dominant role, while the photocatalytic reactions involving C-S bond cleavage, an oxidation of carbon and sulphur atoms were observed in the latter case.[75] The ZnO exhibited a superior visible light activity for the Basic Blue 11 degradation compared to TiO_2.[76] The rapid degradation rate at alkaline conditions (pH 10) was attributed to the better adsorption of dye on ZnO surface and generation of more hydroxyl radicals in the reaction system. Interestingly, the degradation was considerably better at pH 3 as compared to the neutral conditions. The positively charged ZnO surface promotes the migration of electron from interior of nanocrystal to the surface and prevents the carrier recombination. The degradation mechanism was followed by both N-dealkylation and oxidation pathways (pH 9). In another study, the degradation of EV followed oxidative degradation (cleavage of chromophore) at acidic pH and through N-de-ethylation leading to N-de-ethylated EV species along with their N-hydroxyethylated intermediates under alkaline medium. The

former preceded *via* formation of carbon centered radical, while latter was through the generation of nitrogen centered radical. [77]

(d) influence of excitation source and radical scavenger

The photocatalytic degradation of metamitron herbicide under a mixed UV-A (315 – 400 nm) and UV-B (280 – 315 nm) light source was efficient at acidic pH (2.1 – 4) and inhibited with anions like carbonate and sulphate, while chloride showed a weak influence.[78] The surface sites available at the ZnO-metamitron interface for adsorption and electron transfer between catalyst and substrate was blocked by the anions that are very resistant towards oxidation. These deposited anions deactivate the catalyst surface towards the targeted pollutant and also scavenges the hydroxyl radicals in the solution. The generated carbonate or sulphate radicals although behave as oxidants, has lower oxidation potential compared to the hydroxyl radicals.[74,78]

$$OH^{\cdot} + CO_3^{2-} \rightarrow OH^- + CO_3^{-\cdot} \quad (29)$$

$$OH^{\cdot} + HCO_3^- \rightarrow H_2O + CO_3^{-\cdot} \quad (30)$$

$$Cl^- + h^+ \rightarrow Cl^{\cdot} \quad (31)$$

$$Cl^{\cdot} + Cl^- \rightarrow Cl_2^{-\cdot} \quad (32)$$

$$OH^{\cdot} + Cl^- \rightarrow Cl^{\cdot} + OH^- \quad (33)$$

$$SO_4^{2-} + h^+ \rightarrow SO_4^{-\cdot} \quad (34)$$

$$SO_4^{2-} + OH^{\cdot} \rightarrow SO_4^{-\cdot} + OH^- \quad (35)$$

The ZnO effectively oxidized the iodide ion under the influence of increased air flow rate and decreased water content in the reaction medium.[79] The high water content promotes an indirect recombination *via* trapping CB electrons by hydroxyl radical. The hole reacts with the adsorbed iodide ion to form iodine atom and further reacts with iodide ion to produce I_2^-, which undergoes a disproportionate reaction to form tri-iodide and iodide ions.

$$I^- + h^+ \rightarrow I \quad (36)$$

$$I + I^- \rightarrow I_2^- \quad (37)$$

$$2I_2^- \rightarrow I_3^- + I^- \quad (38)$$

The coupling of photo Electro Fenton process with the immobilized ZnO was effective for decolorising Basic Yellow 28 compared to their individual process at pH 3 using CNT-poly tetrafluoroethylene cathode and Pt sheet anode in the presence of Na_2SO_4 electrolyte.[80] This was a consequence of an enhanced generation of hydroxyl radical from both electrocatalysis and photo Fenton process.

$$\text{at anode}: H_2O \rightarrow 1/2\ O_2 + 2H^+ + 2e^- \quad (39)$$

$$\text{at cathode}: O_2 + 2H^+ + 2e^- \rightarrow H_2O_2 \quad (40)$$

$$Fe^{2+} + H_2O_2 \rightarrow Fe^{3+} + HO^{\cdot} + H_2O \quad (41)$$

$$Fe^{3+} + e^- \rightarrow Fe^{2+} \quad (42)$$

The excitation source UV-C was found to be more powerful for photoelectrochemical degradation compared to UV-B and UV-A, which was due to the hydroxyl radical production arising from photolysis of H_2O_2. The initial step in the degradation mechanism involved the hydroxylation of the dye leading to 1,2,3,3-tetramethyl indoline and 4-methoxy benzenamine followed by subsequent hydroxyl radical attack leads to the formation of simple aliphatic acids.[80]

(e) defect mediated photocatalysis

Nanoscopic ZnO embedded in nafion membranes resulted in the faster degradation of RhB compared to the ZnO powder.[81] Initially, blank nafion was soaked in an aqueous zinc nitrate solution overnight to facilitate Zn^{2+} ion exchange. The Zn^{2+}-nafion was then soaked in C_2H_5OH (ZNE) or NaOH (ZNA) to introduce hydroxyl anions. The $Zn(OH)_2$ formed is unstable in hydrophilic cavities (reverse micelles), which can either dehydrolyze to give ZnO or reacts

with a hydroxyl anion to form the growth units of $[Zn(OH)_4]^{2-}$, followed by its polymerization results in ZnO nuclei. The ZNE showed a superior activity and an excellent photostability compared to ZNA despite both the sample had comparable particle size, crystal structure, morphology and surface area. The PL evidenced a large concentration of oxygen defects; oxygen vacancy/interstitial oxygen with ZNE as a result of rapid crystal growth. Under UV excitation, electrons are trapped by oxygen vacancy, while holes are captured at interstitial oxygen to restrain recombination (Fig. 3). The ethanol swelled the membrane film and made the entrance of hydroxide ion easy and uniform. This modified ZnO did not lose its activity even after ten times of recycling. The concentration of Zn^{2+} ion in the solution after the photoreaction was ~0.0148 mg/L for ZnO-nafion film, while it was ~0.2318 mg/L with the commercial ZnO.[82] These nafion membranes form an excellent support for semiconductor nanocrystals because of improved chemical stability, exceptional mechanical strength and high optical quality. The advantages for nafion-templating approach to synthesize metal oxide NPs are: (i) it provides a stable matrix to prevent the agglomeration and corrosion of embedded NPs; (ii) NPs embedded are easy to operate and can be recycled for catalytic purpose; (iii) nafion membrane has small absorbance in the UV-visible region and their hydrophilic cavities and the channels possess a strong polarity and an excellent ion-exchange properties.[83-85] These features enhance the adsorptive capacity of materials, leading to the enrichment of pollutants on the catalyst surface. The hybrid effect between 1.0% monomolecular-layer PANI dispersed on the ZnO surface inhibited the photocorossion and also improved the activity for MB degradation under UV/visible light.[86] The degradation was quenched with EDTA (hole scavenger) for ZnO system, and with EDTA or TBA (hydroxyl radical scavenger) for ZnO-PANI system. This indicates that holes were dominant oxidising agent in the former case, while both holes and hydroxyl radical contributes to

photocatalysis in the latter under UV light. In contrast, hydroxyl radicals predominately participated in the degradation of MB for the composite under the visible light. Under UV light, VB holes transfers to the HOMO of PANI and then migrates to the catalyst surface directly oxidizing the contaminants. Under the visible light, PANI absorbs the incident photons and the excited electron is transferred from its LUMO to the ZnO CB.[86] The coating of PANI *via* cold-plasma treatment technique intentionally introduced the defects (oxygen vacancy and interstitial zinc) and enhanced the activity of PANI-ZnO for MO and 4-CP degradation.[87] In addition, PANI effectively stabilized these defects on the surface of ZnO even after prolonged UV illumination. The surface oxygen vacancy traps the electron from ZnO CB and LUMO of PANI to suppress charge recombination process (Fig. 4). Additionally, an increased donor density due to the presence of Zn_i (Zn_i^+ and Zn_i^0) and V_o (V_o^+ and V_o^0) improve the charge transport and shift the Fermi level towards the CB, which facilitate the charge separation at the semiconductor-electrolyte interface and ultimately supplement the photocatalytic efficiency. The PANI behaves like a p-type semiconductor, which is an excellent hole transporting material and has become better choice for preparing organic-inorganic hybrid photocatalysts. The oxygen deficient ZnO obtained from calcination of ZnO_2 was found to be efficient for the decomposition of DCP under visible light.[88] The oxygen defects are introduced during the decomposition of O_2^{2-} and were tailored by heat treatment at various temperatures. At high calcination temperature (800 $^{\circ}$C, 2 h), pale yellow colour of oxygen deficient ZnO transformed to white color. However, annealing under argon atmosphere preserved visible light absorption edge as the oxygen vacancies are retained under oxygen free condition. The impurity states associated these high oxygen vacancies becomes more delocalized, overlaps with the VB edge, and raises the position of VB making the ZnO more efficient for the visible light absorption. The photocatalytic activity of

oxygen deficient ZnO gradually decreased with increase in the calcination temperature from 400 to 800 °C, which was in agreement with the concentration of oxygen vacancies. However, very low oxygen vacancies did not exert any impact on optical properties. In contrast, oxygen deficiency was not observed for ZnO that was prepared by the calcination of $Zn(OH)_2$.[88] Thus, the electronic and optical properties of ZnO are strongly dependent on the nature and concentration of defects generated during the crystallization process. For ZnO based photocatalysis, excitation at high energy wavelength (254 nm) triggers both photolysis and photocatalysis,[89] however, low energy (340 nm) induces only photocatalysis due to its close association with the bandgap absorption. This indicates an increase in the surface or near surface reactions with the latter excitation source, and that former operates by MVK type mechanism, where the oxygen from the crystal lattice is removed and used in the oxidation reaction. Based on a series of experiments, Ali *et al.*[90] reported that a different degradation mechanism of MB was operated for different ZnO films at different excitation wavelengths, with a competition between two distinctive mechanisms; conventional redox radicals and lattice oxygen driven oxidation. The surface photocatalyzed radical formation was prominent for highly aligned and more crystalline morphologies of ZnO having plentiful oxygen. The lattice oxygen mediated photodegradation was significant for less aligned with more amorphous morphologies having more defects. The high energy associated with 254 nm allows activation energy barrier to overcome for lattice oxygen abstraction and a high number of lattice defects lowers the overall activation energy. However, MVK type mechanism deactivates the catalyst surface thereby inhibiting the redox reactions.[90] Despite the debate concerning the exact role of defects in photocatalysis, it is generally accepted that the surface defects (states) acts as shallow trapping sites, while the localized bulk defects promotes the recombination process. The defects mediated

photocatalysis are vital to realize the photocatalysis pathways, as these defects not only modulate the photoactivity, but are also inherent in pristine metal oxides.

Based on the above results, it can be surmised that heterogeneous photocatalysis is a delicate function of catalyst dosage, particle size, surface acid-base properties, defect density, surface anchored groups, photocatalyst stability, substrate concentration and their redox levels, pollutants molecular structure, presence of electron scavengers beside oxygen, presence of inorganic electrolytes, formation of active free radicals, solution pH, affinity of pollutants and intermediates to react with free radicals, degradation pathways, intensity and wavelength of excitation source.

3.0 Morphological dependence of ZnO on the photocatalytic activity

The further improvement in the photoactivity of ZnO can be realized by providing a suitable geometric structure for an effective carrier transfer pathways. The ZnO has the richest morphologies that are very complex and diversified, which can be easily manipulated with a desirable structure and allows for rational tailoring of surface to volume ratios. The capability to control the particle morphology and understanding the surface signatures of ZnO governed by the particle size and shape may be vital in constructing nanoscale electronic devices. The growth of metal oxides in an aqueous solution is influenced by variable parameters such as temperature, precursor chemistry, chelating agents, solvents, precursor concentration, mineralizers, inorganic electrolytes, templates and pH of the solution.[91-94] The Zn(II) exists as Zn^{2+}, $Zn(OH)_2$, $Zn(OH)_3^-$ and $Zn(OH)_4^{2-}$ in aqueous solution and their concentration ratio depends on pH of the reaction medium. In general, relatively a large quantity of $Zn(OH)_4^{2-}$ under alkaline conditions acts as seeds for the nucleation of ZnO growth units.

The photocatalytic activity of ZnO towards resorcinol degradation followed the order: spherical shape > rod-like > flake-like. The activity of sperhical shape was due to the formation of a nonfaceted morphology comprising high surface area, small crystalline size distribution, and high concentration of electron (oxygen vacancies) and hole traps (oxygen interstitials).[95] The appreciable activity of a rod-like was attributed to the presence of a zinc-terminated {0001} and an oxygen terminated $\{000\bar{1}\}$ polar faces having high surface energy. However, the formation of smooth {1101} and {1010} facets without high surface energy for flake-like morphology resulted in poor activity. These morphologies were tuned by changing the capping agent, Triton X-100 concentration from PMC to CMC during the synthesis step (Fig. 5).[96] In the case of PMC ($2.1x10^{-4}$ mol/L), high yield of ZnO nanoflakes were obtained. During the particle formation, monomers (capping agent) adsorb onto the preferred crystallographic planes and alter the growth kinetics. Thus, growth along all preferred directions will be retarded to produce nanoflake-like morphology during the nucleation stage. The nanoflakes are aggregated due to their nanoscale forces. The spherical micelles are formed at their first CMC ($3.2x10^{-4}$ mol/L) leads to the formation of spherical NPs. Due to the smaller dimension of spherical shaped granular particles, the polar fields generated in each particle will be weaker.[97] Consequently, a lower propensity of agglomeration between single particles leads to an unagglomerated assembly of NPs formation. The second CMC ($1.3x10^{-3}$ mol/L) indicates the structural transition from spherical micelle to rod-like ones to facilitate the formation of NRs. The collective behaviour of the van der Waals forces and the electrostatic interaction support the self-aggregation of ZnO NRs.[98]

Flower-like ZnO thin film (160 nm thick) deposited on the FTO substrate *via* spray pyrolysis (400 ˚C) was photoelectrochemically active for the degradation of organic pollutants like toluene, SA and 4-CP under the natural solar light due to the large content of surface oxygen

vacancies and high surface area.[99] Mesoporous ZnO prepared by solution combustion route using oxalic acid as fuel surpassed its activity for the degradation of OG dye compared to ZnO prepared with other fuels like citric acid, dextrose, glycine, oxalyl dihydrazide, and urea.[100] The furnace temperature was varied between 350 – 450 $^{\circ}$C depending on the number of carbon atoms in fuel and also on the nature of groups. The equivalence ratio (Φ) defined as absolute value of ratio of oxidizer valency to reducer valency was < 1 for citric acid and dextrose, greater than unity for glycine, oxalic acid and urea, unit for oxalyl dihydrazide fuel. The ZnO with a low crystallite size and a high strain was obtained for Φ < 1, likely due to the smoldering combustion, which arise at a combustion temperature of < 650 $^{\circ}$C.[101] This results in an improper crystal growth favouring the formation of small crystals. For Φ≥1, the maximum amount of heat will be produced rendering the proper crystal growth. The morphology of ZnO was agglomerated, irregular, spherical, cylindrical, flower-like for citric acid, dextrose, glycine and oxalyl dihydrazide, oxalic acid and urea respectively. The surface area of the catalyst had no correlation with its activity in this study.

The nanostar ZnO assembled from NRs obtained under hydrothermal conditions (160 ˚C, 2 h) with gelatin under aqueous ammonia was active for MO degradation. The surface and capacious interspaces nanostars provided more opportunity for the diffusion and mass transportation of MO and hydroxyl radicals during the photocatalytic reactions.[102] However, NS, microrods, microsheets and hexagonal prism were observed using NaOH, ethanediamine, urea and HMT respectively. The optimum amount of gelatin to obtain nanostar was found to be 0.02 g and high content (0.036 g) favored the formation of peanut-like structure. The carboxylic groups of gelatin binds to metallic ions *via* coordination or electrostatic interactions to form complexes like gelatin-$Zn(NH_3)_4^{2+}$ and gelatin-$Zn(OH)_4^{2-}$. The gelatin biomolecule are mainly dispersed as

random coils in the solution and behave as soft biotemplate to tailor the shape of ZnO NPs under the reaction conditions. The ZnO nuclei generated from above complexes grow in free space and aggregates through the orientation and alignment to decrease the free energy, forming NRs at the initial stages. The gelatin then confines the growth of ZnO NRs and transforms into star-like *via* Ostwald ripening process.[102] The ZnO NFs (78 nm) was active for the degradation of RhB, Amido Black 10B and Acid Fuchsin compared to the ZnO NPs (30 nm) under the visible light, although, the latter one had a smaller particle size.[103] The porous structure of the nanofibrous mats improved the contacting surface areas between the catalyst and the dye molecules, while an aggregation of NPs in solution lowered its efficiency. The ZnO TPs showed high efficiency for the MO, Acid Orange 7, MB and R6G degradation compared to the NPs, although lower concentration of the hydroxyl radicals and a reactive oxygen radical was observed for the TPs structure.[104] Due to the low concentration of non-radiative defects, PL decay was the longest for the TPs, while a rapid decay of luminescence was observed for a small size NPs attributed to the non-radiative quenching at the surface defects/impurities. In another study, an abundant surface states and the high surface-to-volume ratio of the ZnO TPs exhibited high activity for the RhB degradation.[105] The EDS confirmed the oxygen deficiencies in the TPs structure (atomic ratio of Zn and O is 51.2:48.8), which served as the reactive electron capture centres. Both PL and photosensitivity measurements revealed a high density of surface states that would be beneficial for photocatalytic and device fabrication.[105] The photoactivity of ZnO TPs surpassed the irregular shaped ZnO NPs towards MO degradation ascribed to a 3D branched morphology, which resisted the aggregation during photocatalytic reactions.[63] From the geometrical point of view, the TPs nanostructures assembled into the 3D networks may act as an ideal candidate to harvest the maximum number of photons from a light source. In the reaction solution, the TPs

provide all contactable surfaces, spatial stearic effect against the dense agglomeration owing to its unique structure with four arms growing from one centre and multiple pathways for the diffusion of the reactants and the products.

Highly oriented ZnO NRA synthesized on zinc foil exhibited best activity for the 4-CP degradation compared to a ZnO NR grown on a titanium substrate. The cross sectional SEM observation revealed that the rods with typical lengths of about 500 nm are well separated from each other but densely aligned and a preferential growth occurs along the c-axis perpendicular to the substrate. In contrast, the hexagonal rods were packed in disordered manner for ZnO grown on Ti-foil. In this study, the zinc foil was used both as zinc ion source and as a substrate for the direct growth of NRA.[106] The unique surface features of well aligned NRs and an excess appearance of polar-{0001} facets in the NRA served as the most active sites for the photocatalysis.[107] In addition, the NRA exhibited remarkable activity with little loss even after a fifth run without any change in morphology. The enhanced interfacial charge transfer can be achieved in such 1D material, since the delocalization of carriers is increased owing to their free moving throughout the length of the crystal with minor resistance. Thus, an occurrence of surface trapping states reduces and a more efficient charge separation will be ensured.[108]

Porous ZnO nanopyramids with a greater density of basic sites exhibited a high rate of adsorption and degradation for the acidic dyes such as Fluorescein, Acid Green, Acid Blue and the Acid Black compared to the ZnO nanopyramids without pores and the ZnO mesoporous ellipsoids, but remained insensitive for the adsorption of basic dyes (RhB and Basic Red).[109] Thus, integration in adsorption and photocatalysis facilitates the porous nanopyramids to have contact and react with more dyes per unit time. This ZnO had unique structural features such as high specific surface area (127.7 m^2/g), uniform nanopores (4.7 nm) and large pore volume and

was assembled from 4.7 nm ZnO nanocrystal building blocks with an oriented attachment without any template assistance.[109] The meso-macro porous ZnO NS prepared by one step polyol refluxing process (198 ˚C, 4 h) rapidly degraded MB compared to the ZnO dense NS without any porous structure and/or ZnO nanospheres.[110] The EG (polyol) in the synthesis step played a crucial role in the formation of NS; (i) it has relatively high dielectric constant and most of the metal species are soluble providing a suitable growth conditions for NS; (ii) it lowers the hydrolysis rate of the metal oxides; (iii) it also served as a reducing agent.[111,112] In contrast, the presence of nitrilotriacetic acid and PVP in the reaction system resulted in dense NS and nanospheres respectively.[110] The photoactivity of ZnO hollow spheres for RhB degradation obtained under hydrothermal conditions (180 ˚C, 24 h) of glucose-$ZnCl_2$ mixtures increased with increase in the molar ratio of glucose to zinc ions up to 15, which is attributed to the combined effects of multiple factors such as porous structure, enhancement in the carrier redox potential and the formation of bimodal meso-macroporous structure.[113] The formation of hollow sphere proceeded through three steps: (i) dehydration of glucose with subsequent carbonization results in the formation of carbon spheres with hydrophilic functional groups like –C=O and –OH groups; (ii) entrapment of Zn^{2+} ions into the hydrophilic shell *via* coordination/electrostatic interaction; (iii) removal of carbon spheres, densification and cross-linking of incorporating metal cations in the layer *via* heat treatment leading to hollow sphere formation. In addition, this hollow sphere was stable against photocorrosion at neutral pH and was easily separated from the slurry system by simple filtration or sedimentation due to their large weight, weak Brownian motion and good mobility. These hollow spheres possess unusual hierarchically nanoporous structure, which allows more efficient transport for the reactant molecules to reach the active sites on the framework walls by enhancing the photocatalytic efficiency. Also, hollow spheres

allow multiple reflections of the UV-visible light within the interior cavity that facilitates more efficient usage of a light source.[114] The activity was reduced after grinding the hollow spheres suggesting that the solvent entrapment and sequestration within the enclosed spheres were beneficial for the photocatalysis. The porous structure of the ZnO plates (sintered at 700 $^{\circ}$C, 1 h) was efficient for the Reactive Orange 16 and the Reactive Red 180 dye degradation.[115] The memory of the ZnO plates was evident in retaining the photoactivity after recycling test when kept under dark.[116] The illuminated surface becomes less negatively charged during the photocatalytic process, when positive holes are drawn to the illuminated surface by the layer of space charge region. Conversely, the crystal attains negative charge when the catalyst is kept under darkness. In order to balance the charge, surface diffusion take place and restrain the hole trapping rate under UV illumination, thus retaining the activity instead of deactivation. Compared to the powder form, the plate structure significantly reduced the cost and time for the catalyst removal from the suspension allowing a better recycling and re-use of plates.[115] The rate constants for MO degradation were 1.03, 1.73 and 1.96 h^{-1} for ZnO solid nanospheres, hollow nanospheres and yolk-shell nanospheres respectively, which were in exact (linear) correlation with the intensity of visible light emission in the PL spectra.[117] The evolution of morphology for the zinc citrate microspheres with aging time followed the pathway: solid microspheres to hollow microspheres *via* yolk-shell microspheres according to Ostwald ripening mechanism associated with progressive redistribution of matter from the cores to shells of microspheres, as the cores have higher energy due to their larger curvatures compared to outer shells.[118] Thus, the inner cores gradually dissolve into shells are consumed and shrink with an increase in aging time. Simultaneously, zinc citrate redeposit on outer shell, which increases the shell thickness leading to the yolk-shell microspheres. Thus, the growth of a shell and shrinkage of cores

continues with aging time. The core eventually disappears after aging for 12 h, leaving behind a spherical hollow sphere (Fig. 6). This ripening process is a classic phenomenon in particle growth, wherein the growth of the larger particles takes place at the expense of the smaller particles due to the high solubility of latter.[118] Novel ZnO composed of a core (pyramid)-shell (nanosheet) composite with an open and porous nanostructural surface layers exhibited excellent activity and durability for MO degradation against NPs, NS and nanoneedles.[119] Additionally, a higher redox potential of size quantized NS (~10 nm) that stand on the micro-conic particles promotes the electron transfer from conductive band of a nanosheet with high electric potential to those of a core-part micropyramid with low electric potential.[120] The vertical and net-like or grid-like arrangement of the NS as well as the conic shape of ZnO micro/nanostructures successfully avoid the aggregation and preserve its large specific surface area. Based on the experimental observation, it was proposed that the initial step involves the formation of ZnO hexagonal pyramid-like nanocrystals followed by the buildup of NS network on the facets of pre-formed ZnO microcrystals. This two step growth mode was favoured only for a certain release rate of Zn^{2+} ions (in this study, Zn foil was used as zinc source and the ratio of $V_{\text{distilled water}}$ /$V_{\text{ehtylene diamine}}$ = 3:37 to 1: 7), since a high growth rate leads to a single morphology (one step growth) and a low growth rate resulted into a qausi-equilibrium growth leading to the vertically arranged NRA on a Zn foil. Also, replacing Zn foil with zinc nitrate resulted in irregular shaped particles.[119] The high performance of ZnO NT arrays compared to ZnO NRA for NO_x degradation was ascribed to unique surface features of its well aligned structure. The NTs differ from NRs from the prospect of having a hollow cavity structure.[69] Noticeably, the NT arrays with outer and inner surface have a relatively large surface area (~ twice) compared to the NRA with the same length and the diameter. The peculiar tubular structure provides more interfaces

for NO decomposition increasing the activity of NT arrays. In addition, incident light is preferably trapped in the NT arrays and reduplicatively gets absorbed both inside and outside of the tubes facilitating easy carrier generation.[69]

The spherical particles of the ZnO surpassed its activity for MB degradation compared to NRs and a mixed morphology of particles and rods attributed to the presence of large amount of oxygen vacancies, which traps CB electrons temporarily to reduce the surface recombination.[121] Furthermore, the oxygen vacancies favour adsorption of oxygen to capture CB electrons, simultaneously producing oxygenated free radicals. These morphologies were fine tuned by varying the concentration of hydroxyl anion from 50 to 400 mM NaOH through a soft chemical approach (Fig. 7). At low concentration, spherical NPs (~ 8nm) were formed due to uniform crystal growth as the concentration of the hydroxyl anion was very low to favour anisotropic growth. While at higher concentration of the hydroxyl anion, ZnO growth along {0001} surface was blocked by the binding of $[Zn(OH)_4]^{2-}$ and changed the surface free energy favouring the growth of $\{000\bar{1}\}$ surface to form NRs (length 30-40 nm). However, at intermediate concentration of 200 mM, both uniform as well as anisotropic crystal growth occur leading to the formation of both NPs and NRs. The chemical reaction for ZnO nanostructure formation is as follows;

$$Zn^{2+} + 2OH^- \rightarrow Zn(OH)_2 \quad (43)$$

$$Zn(OH)_2 \rightarrow ZnO + H_2O \quad (44)$$

$$Zn(OH)_2 + 2OH^- \rightarrow [Zn(OH)_4]^{2-} \quad (45)$$

$$[Zn(OH)_4]^{2-} \rightarrow ZnO + H_2O + OH^- \quad (46)$$

The $Zn(OH)_2$ is unstable and hydrolyse directly to ZnO nuclei or react with a hydroxyl anion to form a growth unit of $[Zn(OH)_4]^{2-}$ followed by the polymerization to form ZnO nucleus. The abundant concentration of hydroxyl anion favours the formation of $[Zn(OH)_4]^{2-}$ intermediate,

which are likely to control the surface morphology of ZnO.[121] Thin films of ZnO microrods with an hexagonal shape of submicron size diameter was active for MB degradation compared to ZnS, although latter was more striking for MB adsorption.[122] The morphology of ZnO remained same after the photocatalytic reaction, while the surface of a ZnS microrod was occupied by dye molecules with partial damage in some areas. However, both ZnS and ZnO lost their activity after three cycles of subsequent runs.

The high performance of a sheet-like ZnO for MO degradation compared to a flower-like and a sphere-like was attributed to a large quantization in the bandgap as the mean thickness of the sheets was comparable to Bohr radius of ZnO.[123] This enables the materials to harvest maximum number of photons from the excitation source producing surplus charge carriers thereby enhancing the activity.[124] The photodegradation was faster than mineralization, indicating the high resistance of accumulated byproducts to react with free radicals. Two steps were followed to obtain such a morphology; (i) formation of ZnO sphere as a seed on quartz substrate; (ii) hydrothermal growth of ZnO in an aqueous solution by the reaction of zinc nitrate and HMT, with latter to provide a controlled supply of hydroxide ions. The HMT also reacts with water to produce NH_3, which subsequently forms NH_4^+ ions. Thus, two tetrahedral complexes $[Zn(NH_3)_4]^{2+}$ and $[Zn(OH)_4]^{2-}$ served as precursors for ZnO nucleation. The flower-like NS were formed epitaxially from the seeds after hydrothermal reaction (150 $^{\circ}$C, 4 h), which transforms to sheet-like ZnO at 6 h without agglomeration of ZnO seeds.[123] The combined effects of surface roughness, crystallinity, and an appropriate film thickness of porous ZnO obtained by the chemical bath deposition from a methanolic solution of zinc acetate (0.05 mol/L) and calcined at 500 $^{\circ}$C (1 h) was active for MO degradation compared to those calcined at 300 $^{\circ}$C and 800 $^{\circ}$C, and with different precursor concentrations.[125] At a low precursor content (0.01-0.05

mol/L), the morphology of a porous ZnO film was nest-like assemblies, while globular aggregates was observed at 0.1 mol/L. The porous structure originates from the formation of a flake-like layered zinc acetate, which stand on the alumina substrate with its edge pointing to the surface normal direction and forms a highly porous 2D nest-like structure. The nest-like porous structure also provides enough surface roughness, which is advantageous for the adsorption of pollutants during the photocatalytic reactions. The globular agglomerates easily depart from the film during the photocatalysis because of a low adhesion with substrates and also an effective surface area absorbing the photons from the excitation source drastically reduces, which lowers the activity.[125] The degradation of MB with respect to a ZnO morphology followed the order: flower > oblate > hexagonal sphere > hexagonal biprism > nut-like > NRs, indicating different morphologies display large differences in their activity.[126] The high performance of flower-like ZnO was attributed to more exposure of polar surface and hence more hydroxyl radicals would be formed to participate in redox reactions.[127] These morphologies were obtained by varying the Zn^{2+}:NaOH and Zn^{2+}:TEA ratio under hydrothermal conditions (140 ˚C, 12 h). The NRs were observed without an addition of TEA, while a nut-like structure was formed in the absence of NaOH, revealing the concentration of hydroxyl ions was indispensible for obtaining such diverse morphologies (Fig. 8). Initially, TEA will hydrolyze to produce the hydroxyl ions (Eq. 47), resulting in $Zn(OH)_2$, which further transforms to ZnO after calcination (Eqs 43-46).

$$TEA + H_2O \leftrightarrow [TEA]^+ + OH^- \qquad (47)$$

With increase in the content of NaOH, an excess hydroxyl anion favours the formation of $[Zn(OH)_4]^{2-}$, which transforms to ZnO nuclei at a concentration above its critical solubility.[91-93] These zinc hydroxyl complexes preferentially adsorb on the ZnO nuclei, which lifts the growth along the direction of c-axis and leads to hexagonal biprism shape. When $[Zn(OH)_4]^{2-}$ ions are

relatively insufficient, TEA molecules will occupy the dominant position and served as the structure-directing and assembling agent resulting in a nut-like, a hexagonal sphere-like, an oblate and flower-like structures.[126] The photoactivity towards phenol degradation with respect to various solvents (morphology) followed the sequence: THF (cauliflower-like)> decane (truncated hexagonal conical) > water (tubular and a rod-like) > toluene (hourglass-like) > ethanol (NRs) > acetone (spherical shape).[128] The ZnO synthesized in water were less homogeneous compared to those prepared in organic solvents, as the zinc precursor was better dispersed in the latter. The solvents like THF, ethanol and acetone have high vapor pressure, which limits the growth of ZnO nuclei to favour the NPs nucleation. The aggregation of these NPs and formation of clusters reduced the overall surface area and the surface energy. In contrast, the larger ZnO crystals with faceted morphologies were obtained for relatively a low saturated vapor pressure solvent such as decane, toluene, and water.

These varied nanostructured morphologies encourage charge carrier separation, besides enhancing the surface reactions, that ultimately results in rapid decomposition of organic pollutants. The morphological stability even after recycling many times implies the resistance towards agglomeration and low degree of byproducts accumulation on the catalyst surface during the degradation reactions. The hierarchical structure combining the features of nanoscaled building blocks, not only show unique properties different from those of bulk, but also provide more opportunity for the surface photochemical reaction to realize the morphology dependent surface reactivity.[129] It is therefore desirable to develop a facile protocol for the morphology controlled ZnO with low cost precursors and without special equipments, harsh experimental conditions or toxic reagents. Despite having a comprehensive study relating to the effects of synthesis parameters on the formation of ZnO, the literature is not quite convincing in

establishing relationships among the synthesis parameters, morphological properties and the photocatalytic activity. Understanding such interdependence will provide an insight into the origin of the chemistry behind the photocatalysis, which will advance our capability to utilize ZnO nanocrystals.

4.0 Photocatalytic activity of metal ion doped ZnO

Doping of metal oxides (TiO_2 or ZnO) with foreign ions/impurities initially changes the coordination environment of host metal ion in the lattice and also modifies the electronic band structure *via* introducing localized electronic energy levels within the bandgap states. The former alters the pristine defect structure affecting the mobility of charge carriers, while the latter endows the more efficient manipulation of incident photons. The impurity level of dopant situated either above VB or below CB momentarily traps the photogenerated charge carriers, thus affecting their redox pathways.[130]

(a) Doping with alkali metal ions

The Li (10 %)-ZnO was more active for the degradation of 4-NP under visible light compared to Na-ZnO and K-ZnO, primarily due to electron trapping ability of Li^+ ions, small crystallite size and high surface roughness.[131] The bandgap widening and an efficient charge carrier transfer process were identified as factors responsible for the sunlight driven activity of Mg (0.1 %)-ZnO for MB degradation.[132] The increase in optical bandgap energy by Mg^{2+} doping was attributed to the Moss-Burstein effect caused by electrons generated from the oxygen vacancies.[133] The substitution of Zn^{2+} by Mg^{2+} intensify the oxygen vacancies and the electron concentration due to the differences in electronegativity and ionic radius between the host (Zn) and the guest (Mg). This increase in carrier density lifts the Fermi level into CB of degenerate

semiconductor, resulting in the bandgap widening. The cubic MgO crystallized at higher Mg^{2+} doping (0.2 %) served as recombination centers.[132]

(b) doping with transition metal ions

The enhancement in defect concentration of ZnO by Zr^{4+} (1.5 wt.%) doping resulted in faster resorcinol degradation.[95] The small crystallite size decreases the diffusion path length for the movement of charge carriers from bulk to surface and the size quantization of bandgap enhanced the redox potential of charge carriers. However, a complete mineralization was observed only at 365 nm excitation source rather than at 254 nm. The UV light photolysis indicated that the intermediates formed during the course of degradation absorb light energy at 254 nm to a significant extent, thus shunting the photons away from the ZnO surface. Since resorcinol do not absorb at 365 nm, complete absorption of light by Zr-ZnO facilitated the generation of reactive free radicals in the solution that accounts for complete mineralization. The doping of Ta^{5+} into ZnO by a modified Pechini-type method using water soluble peroxo-citrato tantalum complexes as Ta^{5+} source was positive for MB degradation under the visible light, attributed to a competitive trade off among the crystallinity, surface hydroxyl groups and specific surface area.[134] It was predicted that the crystallinity dominates over the other two factors in enhancing the efficiency. The activity at different annealing temperatures of Ta(1mol %)-ZnO followed the order: 700 > 800 > 900 > 600 > 500 $^{\circ}$C. As the annealing temperature increases, the crystallinity is improved with the loss of surface hydroxyl groups and surface area. The degradation rate increased by two fold with a change in pH of the dye solution from 5 to 8 and declined at higher pH values. The high degree of hydroxylation combined with efficient adsorption between cationic MB and surface negatively charged Ta-ZnO contributes to overall efficiency at pH 8. Although the adsorption of MB was drastically improved at pH > 8, the

density of hydroxyl group decreased and the rupture of hydroxylation on the catalyst surface suppressed the activity. The degradation rate with respect to the dopant content followed the order: 1 > 1.5 > 0.5 > 2.0 > 3.0 mol %.[135] The particle size increased, resulting in the loss of surface area with increase in dopant concentration (> 1 mol %) and an orthorhombic $ZnTa_2O_6$ was formed at very high content of Ta^{5+} (4 mol %). The substitution of Ta^{5+} into the host Zn^{2+} resulted in the formation of defects like zinc and oxygen vacancies, which forms an intermediate electronic level within the bandgap enabling the visible light absorption and also restrain the carriers from recombination.

$$\text{Null} = V''_{Zn} + V^{\cdot\cdot}_{o} \quad (48)$$

$$Ta_2O_5 \xrightarrow{ZnO} 2Ta^{\cdot\cdot\cdot}_{Zn} + 3V''_{Zn} + 5O_o \quad (49)$$

$$O_o \rightarrow V^{\cdot\cdot}_{o} + 1/2\, O_2 + 2e^- \quad (50)$$

The oxygen vacancy forms a deep donor at ~1.0 eV below the bottom of CB and the zinc vacancy defect is relatively shallow at ~0.4 eV above the top of VB.[136] The doping changed the morphology of ZnO from NR to NPs with a spheroidal shape. The catalyst still retained its activity even after storing for 90 days in air, attesting an excellent stability because of high crystallinity.

The defect free Cr (~3 at.%)-ZnO obtained *via* solvothermal treatment (120 $^{\circ}$C, 12 h) in ethanolic solution under alkaline medium showed visible light activity towards MO degradation.[137] The visible light response was originated from the 'sp-d' exchange interactions between CB electrons and localized 'd' electrons of Cr^{3+} ions, which substitutes for Zn^{2+} ions.[138] The 's-d' and 'p-d' exchange interactions leads to a negative and a positive correction to CB and VB edges, respectively, resulting in red shift in the bandgap absorption.[139] The Mn(1%)-ZnO obtained by the wet chemical precipitation technique was detrimental to MB degradation under

UV light, but was beneficial under the visible light.[140] The contribution from donor states (oxygen vacancies and interstitial zinc) and acceptor states (zinc vacancies and interstitial oxygen) enhanced the optical absorption in the visible region and thus the photoactivity.[141] The Mn-ZnO creates electron-hole pairs at the tail states of CB and VB, respectively, under the visible light. The excited electron transfers to adsorbed MB molecule on the particle surface and disrupts its conjugated system leading to its complete decomposition. The VB holes react with water or hydroxide ions to generate hydroxyl radicals, which further degrade the pollutant molecules.[140] In another study, both Mn (1%)-ZnO and ZnO obtained by conventional method (slow crystallization process) showed a low activity for MB degradation under the visible light against the defect rich (zinc interstitials and oxygen vacancies) ZnO, which was crystallized under microwave conditions.[142] The heating of precursor solution occur locally due to the molecular rotation of the medium arising from their interaction with the electromagnetic fields of incoming microwave radiations. This assist a quick energy supply for the reaction, resulting in faster nucleation and growth of nanocrystallites.[143] The rapid inclusion of zinc and oxygen atoms into the crystal lattice creates interstitial defects, which induce the mid gap states and serves as intermediate steps for the electrons and holes during the photoexcitation process. This means that instead of absorbing one UV-photon, an electron arrives at the CB by utilizing multiple photons from the visible light. In the case of conventional heat treatment to induce crystallization, heat passes through convection from the walls of a container towards the centre and takes a long time before establishing thermal equilibrium between the precursor and its surroundings. Thus, thermal decomposition of the precursor contents and subsequent formation/crystallization of ZnO or Mn-ZnO occur very slowly resulting in the formation of nearly defect free nanocrystals. The doping of Mn^{2+} (2 mol %) was positive, while Co^{2+} (1 – 5 mol %) incorporation was

detrimental for the generation of hydroxyl radicals, wherein, these doped catalysts were prepared by a three stage process, consisting of a high energy mechanical milling, heat treatment and washing.[144] It was proposed that Co^{2+} doping served as recombination centers, while the presence of secondary phase like Mn_3O_4 and $Mn_{3-x}Zn_xO_4$ favoured charge separation in Mn-ZnO. Casey *et al.*[66] and Barick *et al.*[145] suggested that dopants like Fe^{2+}, Ni^{2+}, Co^{2+}, and Mn^{2+} were not beneficial to enhance the photoactivity of ZnO. Interestingly, Co-ZnO with bicrystalline wurtzite-zinc blende phases showed high activity for MB and phenol degradation under visible light.[146] The cobalt doping induced red shift in the visible light absorption and homojunction between the mixed phases together with increased surface oxygen vacancies promoted the charge carrier generation-separation pathways. The undoped ZnO had wurtzite structure and that doping of Co^{2+} led to the formation of CoO having zinc blende crystal structure, which served as substrate for the growth of ZnO in zinc blende phase. This is the rarest report on the activity of mixed phase ZnO and further research should focus on tuning the ratios of mixed phases and to understand the charge carrier transfer pathways.

The doping of Ni^{2+} (1 – 15 wt. %) into ZnO thin film *via* combined sol-gel and dip coating method was detrimental for MG degradation under UV/visible light, despite Ni^{2+} doping reduced the crystallite size of the catalyst.[147] The Ni^{2+} served as p-type dopant in ZnO and acts as recombination centre.[148] The decrease of effective charge carrier concentration lowers the band bending near the crystallite surface, thus suppressing the driving force for the charge carrier separation. However, the photostability of both the films were excellent as revealed by SEM images wherein ganglia-like hills and wrinkles morphology of the films were not changed even after recycling for three subsequent runs. In contrast, an increase in doping concentration of Ni from 0 to 5 % into ZnO NRs increased the degradation of RhB, as the dopant induced the

distortion of the local electric field and the charge carriers were trapped around the dopant. At a higher dopant concentration (~10 %), the bandgap of a doped catalyst decreases, reducing the energy of excited electrons and the excess dopant promoted the recombination process.[149] The doping of Pd^{2+} into ZnO although decreased the surface area, improved the activity for MO degradation.[150] The Pd^{2+} doping introduced a new electronic energy level within the bandgap states, which served as a shallow trap level for charge carriers. The charge carriers were efficiently separated with increase in Pd^{2+} content from 2 to 3% followed by a sudden decrease at high concentration. At this optimum dopant concentration, the surface barrier becomes higher and the space charge region becomes narrower. The electron-hole pairs within the region are efficiently separated by large electric field traversing the barrier and promote the charge carrier generation-separation-transfer pathways. For higher dopant concentration, the space charge region becomes very narrow and the penetration depth of light into ZnO greatly exceeds the space charge layer, facilitating the carrier recombination.[151]

The sequence in activity of Cu-ZnO with different dopant content for MO degradation was in correlation with FS technique; lower the intensity, higher the activity.[152] Since FS emission arises from the recombination of excited charge carriers, lower FS intensity indicates a reduced recombination. Thus, Cu-ZnO with 0.5 wt. % of Cu^{2+} was beneficial and higher dopant level was found to hamper the activity. The doped Cu^{2+} traps the electron and detraps to adsorbed oxygen to produce superoxide radicals, while the surface hydroxyl groups traps the holes to form hydroxyl radicals. The optimum heat treatment for this catalyst was found to be 350 $^{\circ}$C (3 h).[152] The Cu-doped Zn-ZnO composite modified by a surface carbon species exhibited the visible light activity for Reactive Brilliant Blue KN-R dye degradation.[153] In the preparation method, CO_2 dissolved in solution was converted to carbon that adhered onto the composite

surface. The doping of copper promotes the crystal growth of ZnO, inhibits the phase transfer of metallic Zn to ZnO and enhances the absorption in the visible region. The composite with a 2.0 at.% Cu loading under the hydrothermal treatment (180 $^{\circ}$C, 2 h) was reported to have high activity, which was ascribed to: (i) substituted Cu^{2+} served as a deep acceptor along with oxygen vacancy, which substantially improved the electron transport properties;[154] (ii) metallic zinc clusters acted as electron sinks due to Schottky barrier formation at Zn-ZnO interface, in which the bulk Zn is surrounded by ZnO shell; (iii) surface carbonaceous species have high propensity for adsorbing the reactants, that facilitates the transfer of reactants to active sites and thus improve the surface chemical reactions.[155] The formation of $(Cu,Zn)_7(SO_4)_2(OH)_{10}.3H_2O$ impurity at higher copper doping level (4 – 6 at.%) did not influenced the activity. The surface doping of copper ($Cu_{1+\delta}O$) on ZnO enhanced the reaction rate towards the decomposition of OG and MB under UV/visible light. The optimum concentration of copper was found to be 1.5 and 0.5 mol % for the catalysts prepared by aqueous method and solid state reaction respectively.[156]

(c) doping with rare earth ions

The Nd^{3+}(1%)-ZnO nanoneedles synthesized *via* an ultrasonic-assisted method was active for MB degradation, as Nd^{3+} served as electron scavengers to inhibit the recombination.[157] The doping of Ln^{3+} (Nd^{3+}-4 wt.%, Sm^{3+}- 8 wt.% and La^{3+}- 4 wt.%) into the ZnO matrix by the polymer pyrolysis method was promising for the 4-NP degradation attributed to the change in strucutral properties such as the surface area and the crystallite size.[158] An suitable loading of the dopant is compulsory for producing a significant potential difference between surface and the centre of particles to separate the photoinduced electron-hole pairs, as the excess Ln_2O_3 covering the ZnO surface may facilitate the carrier recombination. The secondary phase of La_2O_3 nucleated at ≥ 3 mol % doping of La^{3+} into the ZnO matrix *via* precipitation route, while it was

observed at 10 mol % La^{3+} in ball milling method, indicating a high degree of dopant solubility at room temperature in the latter.[159] The doping of La^{3+} (1 mol %) into the ZnO matrix was constructive in the former and detrimental in the latter case for MB degradation, mainly attributed to an increase and decrease of oxygen vacancies after doping, respectively. The relative photonic efficiency of La(0.8 wt. %)-ZnO for TCP and MCP degradation was relatively higher compared to ZnO under the excitation wavelength of 254 nm and 365 nm.[160,161] This was attributed to combined factors of large surface area, quantized bandgap and high density of oxygen vacancies which collectively leads to efficient adsorption of pollutant on catalyst surface, high redox potential potential for charge carriers and enhanced production of hydroxyl radicals respectively. The charge carrier separation was effective with 254 nm excitation source, as it excites the electron with high kinetic energy and hence they escape from the recombination channels. The degradation rate reached a maximum at pH 10 for MCP and declined thereafter. Since MCP is not protonated at pH > 10, electrostatic repulsion between the surface charges on the adsorbent and adsorbate leads to an inefficient adsorption. The low reaction kinetics at the acidic pH was due to the over coverage of MCP on ZnO surface, which prevents the catalyst from photon absorption.[161] The Ce^{4+} doping changed the morphology of ZnO from nanoplates to nanospheres and enhanced the activity for MB degradation (pH 5.4 – 9). In this study, a simple refluxing method (90 ˚C) was used to incorporate Ce^{4+} into ZnO lattice. The Ce^{4+} content of 0.05 mol %, refluxing time of 9 h, catalyst dosage of 0.15 g and calcination temperature of 400 $^{\circ}$C (2 h) was found to be optimized conditions to obtain high performance.[162] The photoactivity of Ce-Ag-ZnO towards Napthol Blue Black dye decomposition was increased under solar light up to pH 9 and declined thereafter, exactly correlating to dye adsorption on the catalyst surface at different pH conditions.[163] The synergistic effect between silver and Ce^{4+} (Lewis acid) to trap a

CB electron with subsequent transfer to the adsorbed oxygen was responsible for such a high activity (Fig. 9).

The doping of foreign ions into ZnO appear to be alternative approach to modify the physical (crystallite size & surface area), electronic (bandgap energy and defect concentration) and morphological features, making them suitable for photocatalytic applications. However, literature reveals widespread disagreement related to above these properties; (i) shift in bandgap towards visible region is observed with transition metal ion doping, while quantization in the bandgap is noticed upon doping with alkali metal ion and rare earth ion doping; (ii) change in crystallite size do not correlate with bandgap energy; (iii) morphological changes after doping is unclear as it may originate from counter anion of the precursor also; (iv) change in defect density distribution-defect free or defect rich is almost impossible to predict owing to its dependence with experimental conditions; (v) dopants can either inhibit or promote the crystal growth; (vi) precipitation of impure dopant oxides may change the chemical composition of ZnO itself. The corrosion-dissolution of ZnO at extreme pH conditions leaches the substituted metal ion from the matrix, thus creating toxicity. These issues must be taken into consideration for designing the doped ZnO nanostructure in near future.

5.0 doping with nitrogen (N-ZnO or $ZnO_{1-x}N_x$)

The cation doping usually produces additional defects or impurities in ZnO, which may act as recombination centers. In contrast, doping with non-metals having small radii are promising candidates because they easily substitute for lattice oxygen sites of ZnO or occupy interstitial sites. Due to its larger solubility in metal oxides and comparable size with oxygen, nitrogen is widely used as a dopant to modify the electronic structures of metal oxides as only

small formation energy is required for the substitution process. In addition, low electronegativity and low ionization energy of nitrogen compared to oxygen reduces the electron density around the doped nitrogen in the pristine oxide.[164]

(a) photoactivity of N-ZnO

Highly crystalline N-ZnO obtained *via* vacuum atmosphere method (380 ˚C, 2 h) using melamine as nitrogen source was active for the degradation of MO under simulated daylight illumination.[165] The melamine transformed into isocyanic acid upon heating (120 ˚C), that reacted with residual oxygen or water in the vacuum tube chamber to form ammonia, which subsequently mix with ZnO to form N-ZnO.

$$NH_3 \leftrightarrow NH^{2-} + 2H^+ \quad (51)$$

$$xNH^{2-} + ZnO \leftrightarrow ZnO_{1-x}N_x + xH_2O \quad (52)$$

In addition, melamine combines with oxygen and small amount of N_2 was also generated, further promoting the nitrogen doping into ZnO *via* diffusion of nitrogen atoms. Interestingly, un-reacted isocyanic acid transformed to melamine during the cooling process, which could be collected for reuse.[165] The surface doping of nitrogen on the ZnO TPs showed the visible light activity for Bisphenol A degradation.[166] It was proposed that the nitrogen forms isolated N 2p states above VBM intensifies the absorption in the visible region. The electron-hole pairs generated between N 2p states and CB of Zn 3d levels are separated through trapping from surface adsorbed oxygen and the hydroxyl groups, respectively. The N-ZnO prepared by the decomposition of zinc nitrate in air (350 °C, 3 h) showed high performance for Cr(VI) reduction and MO oxidation under visible light.[167] However, the activity of N-ZnO was lower for MO oxidation and better for Cr(VI) reduction compared to a pure ZnO under UV light. Based on the First principle calculations, it was proposed that the nitrogen doping into ZnO will cause the

appearance of a redundant carrier, i.e., hole near the top of VB. The mutual exclusion effect between holes will enable the carriers to form a narrow-deep acceptor level in the energy gap and induces a conductivity conversion of N-ZnO from n-type to p-type, which was also supported by iodometric titrations.[168] Thus, photoformed holes move towards the interior of the p-type semiconductor under illumination, while electron migrates to the surface to favour the reduction process. In another study, N-ZnO obtained by using zinc nitrate under solvothermal conditions (260 ˚C, 20 min followed by calcination at 400 ˚C, 2 h), showed appreciable performance towards RhB degradation.[169] The increased oxygen defects, improved absorption ability of incident photons and extended carrier lifetime were responsible for high activity. In the synthesis step, zinc nitrate coordinate to oleylamine and form zinc-oleylamine complex (130 ˚C), followed by pyrolysis to form N-ZnO at high temperatures. The oleylamine served as structure directing agent, influencing the nucleation and aggregation process of NPs, which are ultimately assembled to microspheres with mesoporous structure. Liu and co-workers[170] suggested that substitutional nitrogen doping in semi-crystallized ZnO NPs was effective towards RhB degradation under visible light. In contrast, such successful doping failed in highly crystallized ZnO, during the calcination in gaseous ammonia atmosphere (400 ˚C, 30 min). The partially disordered structure and defects in the surface layers of semicrystallized ZnO serve as reactive sites (energetic) for the substitution of nitrogen during the heating process. In contrast, long-range order surface structure of crystallized ZnO requires high energy for the substitution of nitrogen into oxygen which could not be accomplished at 400 ˚C. The N-ZnO bundle-like NPs obtained from ZnOHF precursor demonstrated exceptional visible light induced water oxidation without applied bias, and the activity was further enhanced by loading IrO_2 co-catalyst.[171] The ZnOHF decomposed to ZnO and HF during the heat treatment in NH_3 gas flow (973 K). The

ZnO intermediate is subsequently doped with nitrogen, while HF reacts with ammonia gas to form NH_4F flake-like byproduct. However, this N-ZnO was less active for MB degradation under visible light. As the mechanism for water oxidation and pollutant degradation are entirely different, it was suggested that the surface of N-ZnO possesses energetic sites for oxygen evolution, while lacks reactive sites for pollutant degradation. The ZnO will be partially reduced in highly reductive atmosphere and resulting Zn vaporizes due to its low melting point at high calcination temperature (1073 K).[171] The doping of nitrogen as N_o acceptor states was detrimental for MO degradation.[172] The PL studies indicated that N-related defects increased with increase in nitrogen content accompanied by rapid recombination process. The heavily doped (N_o) acceptor states provide large number of internal holes, which may hinder the formation of photogenerated holes.

(b) coupling of N-ZnO with other semiconductors

The glass-ZnO-$ZnO_{1-x}N_x$ and glass-$ZnO_{1-x}N_x$-ZnO heterojunction was positive for humic acid degradation, indicating the synergism between ZnO and $ZnO_{1-x}N_x$.[173] However, activity was found to depend on mode of the light illuminating the composite; (i) the former was active when light was illuminated from film to glass side, as hole accumulates on $ZnO_{1-x}N_x$ layer to produce more hydroxyl radicals that react with pollutants. While few carriers will be generated in the outer ZnO layer and inability of humic acid to diffuse into $ZnO_{1-x}N_x$ layer in the latter case resulted in low efficiency; (ii) the glass-$ZnO_{1-x}N_x$-ZnO was beneficial when light was illuminated from glass to film side attributed to efficient absorption of visible light by the $ZnO_{1-x}N_x$ layer. In the case of glass-ZnO-$ZnO_{1-x}N_x$, most of the incident light will be lost *via* diffused reflection in ZnO layer and outer $ZnO_{1-x}N_x$ may poorly absorb the incident photons.

The nitrogen doping into ZnO *via* spray pyrolysis at 600 °C improved the activity for CH_3CHO decomposition under the visible light. [174] The nitrogen atom existed in two chemical forms: one was site-N (nitrogen substituting oxygen atoms of ZnO), while the second was residual nitrogen that was originated from the precursors. Further improvement in the performance of N-ZnO was achieved by coupling with WO_3 (or V_2O_5) under UV/visible light, while the efficiency was hampered in the case of Fe_2O_3.[175-177] The nitrogen content in the catalyst increased monotonically with increase in WO_3 (or V_2O_5) additive amount, while it was insensitive by the addition of Fe_2O_3. The highest activity was observed at 0.7 wt.% of Fe and 5.8 wt.% for W series powders at the spray pyrolysis temperature of 800 °C and 1000 °C, respectively. Under the visible light, the nitrogen dopant forms an energy state above the VB of ZnO serving as a "stepping stone" for electron transfer from VB to the impurity level and from impurity level to the ZnO CB. The electron then transfers to WO_3 (or V_2O_5) CB, while the hole migrates in the opposite direction. Tennakone *et al*.[178] reported that W(VI) in WO_3 could easily be reduced to W(V) by excited electrons and may be reoxidized to W(VI) by detrapping them to an adsorbed oxygen. In contrast, CB and VB of Fe_2O_3 sandwiches between ZnO band edges, and thus both electron and hole transfers in one direction resulting in the recombination. The high activity of V_2O_5-$ZnO_{1-x}N_x$ compared to WO_3-$ZnO_{1-x}N_x$ was probably due to the larger difference in the CB edge between V_2O_5 and ZnO, which facilitates thermodynamically faster electron transfer process. A typical feature of sprayed catalysts is the homogeneous distribution of ingredients throughout the particle surface, as they are derived from a homogeneous solution.[174-177] The fabrication of hybrid SnO_2 NFs decorated with surface bound N-ZnO showed high performance for RhB degradation under UV/visible light.[179] According to the band energy diagram, photoelectrons generated in the CB of SnO_2 and holes in ZnO VB can be separated at

the heterojunction by a favourable bias between the two sides. In addition, a lower resistance caused by the formation of oxygen vacancies upon nitrogen doping indicates an easy carrier transport and enhancement in the VB of ZnO.

Compared to broad literature on N-TiO_2, N-ZnO is seldom investigated, due to inconvenience associated with realizing nitrogen doping process by the commonly developed synthesis routes. The undesired transformation of substituted nitrogen to molecular nitrogen at the elevated temperature impairs the understanding of doping process itself. However, low-temperature doping quite often leads to poorly crystallized samples that cannot guarantee always high activity. At the atomic level, the homogeneous distribution of nitrogen dopant throughout the matrix is essential for narrowing the bandgap of semiconductor, while surface doping often leads to localized states which may not be very effective for visible light response. The efficiency of N-ZnO reported so far is not satisfactory and still provides a room for further investigation.

6.0 Deposition with noble metals

Metal oxide-metal heterojunctions represent a novel class of advanced functional materials that have attracted tremendous interest owing to their promising applications in various fields.[180] The deposition of metal NPs on semiconductor surface is gainful, in which particle size could be controlled independently and very narrow size distribution can be obtained. It is assumed that metal NPs modifies the reactive sites and the deposited noble metal itself serves as a catalyst to decompose the pollutants.[181] The metal islands captures the photoinduced charge carriers and intensify the light absorption in semiconductor oxides, with both effects facilitate the redox reactions and amplify the photocatalytic efficiency.[180] The double layer charging around the metal NPs facilitates the storage of electrons within them.[182]

6.1 Photocatalytic activity of Ag deposited ZnO (Ag-ZnO)

The Ag (1.0 wt.%)-ZnO obtained by deposition-precipitation method showed high activity for MO degradation due to the maximum distribution of Ag and Ag-ZnO interface with low concentration of surface oxygen defects. However, a sample obtained by coprecipitation did not dispersed well in dye solution resulting in very low UV light utilizing efficiency.[183] The Ag NPs distributed along the hollow interior of ZnO NRs, supported over Si (100) wafers switches from superhydrophobic with WCA > 150° to superhydrophillic having WCA < 10° and also evidenced an inflexion point at ~ 110° under UV/visible light.[184] The visible light was less effective in inducing superhydrophilicity, as WCA < 10° reached after irradiation of 150 min, while it was otherwise attained in 8 min under UV illumination (Fig. 10). The surface recovered its superhydrophobic character after storing the samples in dark (full recovery after 5 days). It was proposed that the ZnO close to Ag NPs behaved as a superhydrophillic surface because of the hydroxyl enrichment under the light illuminating conditions. The Ag NPs (1.66 wt.%)-ZnO microrods with an interface between {100} plane of ZnO (0.28 nm) and {101} plane of Ag (0.235 nm) showed a strong performance for MB degradation under UV/visible light and its efficiency was maintained even after five consecutive runs.[185] The high crystallinity of ZnO (20 nm) and Ag (20-50 nm) are responsible for high performance, while a low concentration of surface defects in micro/nano configured structure improved the photostability. These structures possess an overall dimension in micrometer with nanosized units. The assembled nanosized units are stabilized to ensure an improved structural stability that reduces the aggregation. The Ag islands on ZnO surface act as an electron wells to inhibit the recombination and the plasmatic effect of Ag NPs promote the photocatalytic activity (Fig. 11). The dimer type Ag-ZnO NRs was synthesized by the solvothermal method (160 ˚C, 24 h), wherein, Ag metals were embedded in

the ZnO NR *via* Zn-O….Ag bond formation. The PL spectra revealed that the oxygen vacancy defect density increased upto 5 at. % of Ag and decreased thereafter, exactly correlating to an observed efficiency of Ag-ZnO for MO degradation.[186] The formation of oxygen vacancies was due to the intermolecular dehydrolysis of precursors to form ZnO-Ag_2O heterostructure, followed by a treatment with ethanol under solvothermal conditions.

$$Zn(OH)_4^{2-} + 2Ag(OH)_4^{2-} \rightarrow ZnO - Ag_2O \xrightarrow{ethanol - solvothermal} Ag - ZnO_x(1-x)V_o^{\cdot\cdot} \quad (53)$$

Surprisingly, the concentration of ZnO after Ag deposition did not had any effect on the degradation rate. This composite had an excellent stability because of the surface-to-volume ratio of ZnO and an intimate contact between Ag and ZnO. According to the proposed mechanism, an electron transfer from ZnO to Ag or to oxygen defects and finally to the solution effectively suppress the recombination process.[186] Highly ordered ZnO NRA fabricated *via* wet chemical route and photodeposited with Ag (0.05 M $AgNO_3$) was promising for MB degradation, without loss in the activity even after a five consecutive runs.[187] The ZnO microspheres modified with Ag NPs, prepared by "one pot" strategy in EG medium performed better for RhB degradation.[188] The EG served as a reaction medium for the formation of ZnO *via* a forced hydrolysis and also reduced Ag^+ to Ag metal. The efficiency with respect to Ag content followed the sequence: 2.5 > 1.25 > 0.625 > 5.0 mol %. Thus, the deposition of Ag clusters with an appropriate amount on ZnO surface captures and transfers the CB electrons to adsorbed species. The Ag NPs were found to aggregate and or the size of Ag particles increased at high Ag content, promoting the recombination process. In addition, the large particle size of the composite easily settled from the reaction system within 10 min even without centrifugation.[188] The deposition of 0.2 wt.% Ag around the oxygen vacancy sites on the ZnO surface reduced the defects, improved the

photostability and the efficiency for CV degradation without any change in the crystal structure even after recycling for many times.[189] The CB electrons trapped by Ag either reacts with chemisorbed/physisorbed/dissolved oxygen in the dye solution to form a reactive oxygen species. The suppression of degradation kinetics under the argon ambient revealed that the active oxygen formed by the reaction of CB electron and the oxygen chemisorbed on Ag was the potential oxidant responsible for the dye degradation. This suggests that the metallic Ag promotes the reaction between chemisorbed oxygen and CB electrons to promote charge separation and the photostability. Although PL revealed lowest intensity for 6.7% Ag-ZnO, photoelectrochemical measurements indicated a reduced photocurrent as the holes get trapped by a large number of negatively charged Ag particles that are detrimental to photocatalytic reactions.[190] This process of hole capture proceeds through a non-radiative pathway, which cannot be detected by PL measurements. The hydrothermal synthesis (120 ˚C, 6 h) of Ag(6.2%)-ZnO in the presence of HMT resulted in faster degradation of RhB.[191] During the composite preparation, HMT transforms to NH_3 and HCHO, which served as a precipitating agent for ZnO formation and as a reducing agent for Ag^+ to metallic silver respectively. Pure ZnO exhibits pillar and bundle-like morphology, while addition of silver resulted in a rod-like structure. In contrast, an increase in HMT concentration resulted in a pillar-like morphology, as it prevents the influence of silver on the equilibrium between Zn^{2+} and NH_3. The UV emission of ZnO was enhanced after depositing with Ag due to an increase in the concentration of excitons, as a result of interface between Ag islands and ZnO.[191]

The Ag (3 mol%)-ZnO prepared by a non aqueous sol-gel process exhibited higher activity compared to Degussa P25 and unmodified ZnO for the degradation of R6G under the sunlight.[192] The segregation of Ag around the ZnO grain boundaries (when calcined at 400 ˚C, 2

h) inhibits the grain growth and provides more surface active sites, which enables the charge carriers to react with the surface adsorbed molecules to form active free radicals. The Ag modification was detrimental at high temperature (800 – 1000 $^{\circ}$C), as Ag promoted the densification and grain growth of ZnO by forming the high surface energy silver islands, which reduced the surface active sites for the pollutant adsorption as well as photon absorption. The degradation of R6G on Ag-ZnO surface takes place by the multiple charge transfer pathways under the visible light (Fig. 12). The high reduction potential of R6G was found to be a vital factor that dominate the electron transfer process and thereby defines the degradation pathway.[192] The optimum Ag content towards hydrogen evolution from water-methanol mixture was found to be 1.6 and 8.3 mol % under UV-*vis* and solar light respectively.[193] The better dispersion of Ag NPs and large exposure of ZnO surface facilitated efficient light absorption in the former case, while formation of Ag_2O-ZnO heterojunction additionally promoted the activity in the latter case.[194] The electron transferred from ZnO CB to Ag NPs effectively reduced the H^+ to H_2 on its surface, while the holes oxidize the alcohol.

The worm-like Ag (2.8 at.%)-ZnO core-shell composite with the single crystal Ag NWs serving as core, on which a dense ZnO particles grow as the shell exhibits maximum activity for RhB degradation.[195] The synthesis route involved the dispersion of single crystal Ag NWs into a mixed zinc acetate and TEA aqueous solution. The ZnO particle seeds are then partially deposited onto the surface of Ag NWs to form nucleation sites for the subsequent growth. During the early stages of ultrasonication, ZnO crystal nuclei are formed on Ag lateral surface by the reduction reaction of zinc acetate. The initial particle seeds so formed continually aggregate and crystallize in the course of reaction time, leading to an increased diameter of ZnO shell. Finally, a dense and complex worm-like heterostructure was formed.[195] Gu *et al.*[196] reported a high

activity of dendrite like Ag (8 at.%)-ZnO, wherein the ZnO NRs were grown hetero- epitaxially on the Ag NWs of {111} and {100} lateral surfaces. This heterostructure formation involved two steps: (i) the single crystal Ag NWs with a truncated-rhombic cross-section is dispersed in zinc nitrate and HMT solution. The Ag NWs has four {111} and {100} lateral surfaces, on which ZnO NRs were grown; (ii) the nucleus of crytstalline ZnO was formed on the Ag lateral surfaces by the thermal decomposition of Zn^{2+} amino complex, followed by preferential growth along <0001> direction during the continuous chemical reaction. Thus, the ZnO NRs grow vertically to the length direction of Ag NWs to minimize the interaction or competition among themselves. Finally, an ultrathin ZNWs or NTs also grow from ZnO NRs.[196]

6.2 Photocatalytic activity of M-ZnO (M= deposited with Pd, Pt and Au)

The photocatalytic performance of ZnO was improved after depositing with Pd (0.5 wt.%) for the degradation of gas phase n-C_7H_{16} and phenol in the liquid phase.[27,197] The lattice oxygen on the ZnO surface was reduced after Pd deposition accompanied by an enhancement in the adsorbed oxygen content as well as surface hydroxyl groups. The electron transfer from CB of ZnO to deposited metal and the adsorbed oxygen depends on the size and distribution of metal on the semiconductor surface. If the sizes of metal NPs are too large, its Fermi level will be lower than that of adsorbed oxygen and the electrons cannot move uphill. In contrast, the Fermi level of very small size metal NPs lies above the CB of ZnO itself due to the size quantized effect, thus disabling the electron transfer from ZnO CB to metal NPs. Thus, an optimal particle size is essential for the metal NPs, to ensure its Fermi energy level to lie between ZnO CB and the adsorbed oxygen to facilitate unidirectional electron transfer from ZnO CB to the metal NPs and then to adsorbed oxygen.[198]

The Pt-ZnO porous nanocages were fabricated through the incorporation of Pt into ZnO porous shells by an ultrasonic irradiation-assisted two step etching of Zn-ZnO core-shell NPs colloids.[199] The diameter of Pt clusters was tuned from 2.5 to 1.1 nm with a change in ultrasonic power from 160 to 400 W and the size distribution becomes narrower. The first step of H_2PtCl_6 etching induces the core hollowing and Pt incorporates through the diffusion-redox-deposition process. The second step of $C_4H_6O_6$ etching induces the nanoshell opening due to an amphoteric nature of ZnO. These nanocages were active for MO degradation, which is attributed to its outstanding features: (i) abundant nanoscale Schottky barriers will be formed because of their small size and high density of embedded Pt clusters, which endue these nanocages with strong interface to separate the charge carriers; (ii) a hollow and porous structure increases the specific surface area and the active sites for redox reactions.[199]

The Au-ZnO hybrid with a hexagonal pyramid-like morphology was active for RhB degradation.[200] These nanopyramids possess a narrow size distribution, comprising Au NPs as the tip and hexagonal ZnO nanopyramids as the tail. In the presence of oleylamine and dodecanol as the solvent and capping agent, respectively, ZnO nanopyramids epitaxially grow over the presynthesized Au seeds, wherein Au decorates at the basal surface of hexagonal ZnO nanopyramids ({0001} polar plane) as a result of lower interfacial energy at polar-metal interface.[201] In another report, a multifunctional hybrid structure of Au NPs and a 3D hierarchical flower-like ZnO comprising of a large specific surface area and a small Au NPs was positive for RhB degradation.[202] The morphology of Au-ZnO was very stable and the efficiency was retained even after three runs, underlining its extraordinary stability and reuse in the photocatalysis. The unique features of this composite are: (i) the interspaces in a flower-like nanostructures allowed facile diffusion and the mass transportation of RhB molecules and hydroxyl radicals during the

photochemical reactions; (ii) a strong electronic interaction between the plasmonic Au NPs and ZnO resulted in efficient charge transfer process; (iii) the Au NPs on ZnO surface lowers the work function[203] and the adsorbed oxygen at the interface between Au and ZnO, facilitates an easy electron transfer to oxygen, which produces the reactive oxygenated species to enhance the degradation reaction. The Au (25.5%)-ZnO NRs surpassed its activity for RhB and 4-CP degradation over ZnO NRs.[204] In this study, gold was decorated on ZnO NRs *via* galvanic displacement reactions at room temperature with an aid of Cu foil and $CoCl_2$ solution. The dynamic force for a galvanic displacement reaction stems from the difference in half-cell potentials between metal ions to be reduced and a substrate to be oxidized. For the deposition of metal NPs, the half cell potential of a reduced species must be higher than that of an oxidized substrate. Consequently, Au NPs with a narrow size distribution can be directly deposited onto a Cu foil without any additional reducing or capping agents. The $CoCl_2$ improves the hindrance towards homogeneous nucleation, while an autocatalytic growth of particles rapidly depletes the gold monomer concentration in the solution, with both the effects collectively favours a heterogeneous nucleation. The mechanism of phenol degradation involved the steps; (i) scission of ring C-Cl bond gives a short lived hydroxyphenyl radical, which combines with a proton to form phenol followed by *o*-hydroxylation results in catechol; (ii) 4-chlorocatechol resulting from the hydroxylation of 4-CP, undergoes *p*-dechlorination and subsequently reacts with the protons in the presence of a CB electron forms catechol; (iii) oxidative hydroxylation of the catechol and phenol gives hydroxyhydroquinone and hydroquinone. Finally, phenolic rings are opened to form aliphatic compounds, which on continuous oxidation leads to mineralization (Fig. 13).[204] The thiolate protected Au NPs (2 wt.%) decorated on ZnO exhibited an enhanced activity without requiring any thermal activation for both oxidative (R6G degradation) and reductive

(thionine degradation) pathways under visible light,[205] which was in contrast to TiO_2 with thiolate-protected gold NPs.[206] The presence of ligands on Au NPs imposed a large kinetic barrier for an electron transfer from TiO_2 to the gold NPs and thus catalytic activity were accelerated only after removing the ligand after thermal treatment. In contrast, a thermal treatment of Au-ZnO did not improve the activity significantly, indicating that an electron transfer through linker ligand to Au NPs occurs at relatively shorter time scale. The strong electrostatic force of attraction between a negatively charged carboxylate anion of glutathione molecule and positively charged ZnO surface under neutral pH conditions resulted in Au-ZnO without any additives. The monodispersed Au NPs surface avoids both direct and trap related charge carrier recombination channels by extracting electrons from the photoexcited ZnO and supress the recombination within the metal oxide.[205] The photocatalytic activity increased with increase in gold size from 1.1 to 2.8 nm which was in accordance with electron transfer rate from ZnO to Au NPs that followed size-dependent capacitance model. Thus, both photocatalytic and electron transfer rate can be controlled by the size of mediating gold capacitors.[207]

The Au (3 wt. %)-ZnO obtained by the flame spray pyrolysis was effective for MB degradation, while Pt (1 – 3 wt.%)-ZnO exhibited poor efficiency, although PL revealed the low degree of carrier recombination for both the composites.[208] The deposition of Pt renders an ohmic contact, which neither induces the Fermi level shift towards more negative potentials nor stores the photogenerated electrons, but rather discharges them into the electrolyte.[209,210] In contrast, the Schottky contact between Au and ZnO facilitated efficient charge separation and induce the Fermi level equilibration between Au and ZnO. The metallic gold has unusual capacity to store electrons without facilitating their discharge into the solution and thus the photogenerated electrons get distributed between semiconductor and the metal layer. However,

such an ohmic contact promotes the efficiency of certain photocatalytic reactions.[211] The photoactivity of Au-ZnO NRs for MO degradation was found to have dependence on the diameter and the densities of Au NPs on the ZnO surface. For instance, Au deposited on ZnO NRs using 10^{-4} – 10^{-5} M $HAuCl_4$ with photoirradiation for 30 min exhibited high activity compared to other reaction conditions (10^{-3} or 10^{-4} M $HAuCl_4$,10 min).[212] The maximum activity was observed for Au NPs < 15 nm and activity declined for 30 nm. It was suggested that the Au NPs with a smaller diameter and high density on the surface of ZnO NRs induce greater reduction in the built-in potential barrier due to a large shift in the Fermi level with CB.[182,210] At higher metal loadings, the intensity of incident light for the ZnO absorption will be reduced by the scattering due to larger Au NPs on tips. In addition, formation of a Schottky barrier at the junction of ZnO NRs and Au NPs inhibits the electron injection from the semiconductor to metal.[209,213] The charge distribution between UV-irradiated ZnO and gold NPs results in the Fermi level equilibration. Additionally, the transfer of electrons to the metal nanocore followed by equilibration continues until the Fermi level reaches close to the CB edge of ZnO and that each injected electron within a gold NP shifts the Fermi level by 0.1 V, which obviously increases the photopotential of nanocomposite electrode.[210,214] The different optimal content of metal NPs on ZnO surface for maximising the photoactivity as reported by several research groups is due to the varied morphologies of composite, crystallinity of metal or ZnO, charge density distribution and density of interface contacts.

The multiple role of deposited metal like altering (increase or decrease) the surface defect concentration, increase of chemisorbed oxygen and hydroxyl group density, improved charge carrier separation and visible light response together with change in morphology, makes it an ideal candidate for modifying the electronic properties of ZnO. The size of deposited metal,

crystallinity of metal oxide, segregation of metal on the surface defective site of ZnO and dispersivity of metal-ZnO composite in the reaction solution are the decisive factors to dictate the photocatalysis. The disadvantage of metal aggregation to clusters and relatively a low coverage on metal oxide surface at high and low loadings, respectively, affects the photocatalytic properties of the composite materials.[196,215] The decoration of noble metal onto varied morphology of ZnO under wide variety of preparative methods attests its structural stability that is required for photocatalysis. More importantly, this composite easily settles down and retains its efficiency even after many times of recycling without agglomeration of particulates. Rather than surface deposition, further research must focus on metal core or metal embedded within metal oxide for practical applications. However, the exact role of a deposited metal resulting in such an enhancement is yet to be realized at the nanoscale regime. The combination of well defined metal NPs with ZnO opens the avenue to develop tunable nanoscale materials, whose reactivity can be controlled by varying their intrinsic and extrinsic properties.

7.0 Coupled semiconductors

The electronic-coupling of semiconductors with different bandgaps to form heterojunctions has become a principal focus, because of their unique properties arising from the interfacial interaction at the nanoscale that are not encountered in the individual nanomaterials.[216] A solid interfacial structure is a underlying factor in establishing the charge transfer behavior between the different semiconductors in their heterostructure and thus their photocatalytic activities. It is widely accepted that an extended carrier lifetime and an enhancement in the interfacial charge transfer to the targeted substrates can be attained by such heterostructures, through the formation of heterojunction interface or intrinsic staggered band

offset.[217] This improvement was related to the interface electric field that is built in junctions, originated from the band bending and vectorial transfer of electrons and holes in the composite. Although, the pure ZnO has defect rich chemistry, intense interest is devoted in hybridising with another nanophase materials, which is advantageous to overcome some intrinsic defects of ZnO and to impart new physicochemical and optoelectronic properties in order to extend its applications in diverse fields.

7.1 Coupling of ZnO with metal oxides

(a) Photocatalytic activity of ZnO-TiO_2

The photocurrent generation and MB degradation was enhanced for ZnO NRs-TiO_2 composite (Zn/Ti molar ratio of 2:1) under UV-*vis* illumination, as the large surface area enabled the maximum light harvesting ability and improved electron transport properties.[218] The deposition of titania NPs on the ZnO NR passivates the surface recombination centers and act as a radial energy barrier that can repel electrons from the surface of ZnO NRs. Alternatively, the electron transport within a single crystalline ZnO NR will be much faster and surface fields within each NR reinforces the charge separation because of longer diffusion length for charge carriers.[219] The preserved crystallinity of TiO_2 NPs and ZnO NRs permit an efficient electron injection and transport within the composites. The Mott-Schottky plot revealed a large negative shift of CB and a high donor density ascribed to the high concentration of surface states.[218] The dispersion of titania on ZnO reduces the defect density and inhibits the photocorrosion.[54] Anatase TiO_2 immobilized on single crystalline TPs like ZnO enhanced the phenol degradation under Hg lamp without a cut-off filter, while its activity was lower compared to Degussa P25 under the excitation wavelength of > 340 nm. The close match between {101} crystal plane of anatase with

'a' and 'b' values of hexagonal ZnO, facilitates an efficient heterojunction *via* epitaxial growth mechanism.[220] The highly crystalline ZnO-TiO_2 prepared by the direct mixing of sol and calcination (500 ˚C, 2 h) was active for MO degradation.[221] The activity exhibited a linear tendency of rate constant against the value of Ti/(Ti+Zn), excluding at 75% because of the poor crystallization. This fact was confirmed by the increment in degradation rate with increase in calcination time to 5 – 10 h. The derived linear fit followed the relation:

$$k = 0.297 + 0.438\ x\left(\frac{Ti}{Ti + Zn}\right) \qquad (54)$$

Alternatively, treating the above composite with 7 – 28% NH_3 atmosphere (24 h, room temperature) and calcination at 500-700 ˚C for 2 h, also improved the crystallization and promoted anatase to rutile phase transition, consequently enhancing the photoactivity.[222] The dominant hexagonal $ZnTiO_3$ was observed at 700 ˚C for NH_3 treated composite, while both cubic and hexagonal $ZnTiO_3$ phases were formed for untreated composite. However, poorly crystallized composite prepared by in situ mixing of sol followed by calcination showed very low activity.[221]

Macro-mesoporous thick films of ZnO-TiO_2 with homogeneously distributed open porosity were promising for MO degradation.[223] The macroporous channels improves the light harvesting capacity by enhancing the light transfer paths for photon energy distribution onto the mesoporous network. Such a structure-in-structure arrangement favours a molecular transport control and prevents the catalyst deactivation by the inert deposits. Thus, the macro-meso-porous structures offer a readily accessible pore-walls for molecules and also diminish the pressure drop over a monolithic material.[223] However, the composite activity was lower than a pure TiO_2, indicating that the presence of ZnO was found to hamper the composite activity.[224] It was

proposed that the TiO_2 particles was surrounded by ZnO film and an optical excitation results in the electron accumulation in ZnO film, while holes are confined to the particles, which reduces the number of sites available for degradation.[223] The sulfated ZnO-TiO_2 obtained *via* modified sol-gel route and calcination (550 °C, 4 h) using citric acid as a complex reagent with zinc sulfate showed superior performance for MO degradation compared to the composite prepared with zinc chloride and zinc nitrate precursors, indicating the role of sulfate group in high activity.[225] In addition, sulfate group restrained anatase phase even at a high calcination temperature in the composite. The sulfated ZnO-TiO_2 showed superacid behaviour, which favours transfer of CB electrons to the surface resulting in an efficient charge carrier separation. The activity was reduced after washing with water due to the removal of sulfate groups and also on calcination at 700 °C (4 h) because of the sulfate group decomposition, increase in the rutile content and formation of impure $ZnTiO_3$.[225]

The self-supporting ZnO-TiO_2 fabricated by the tape casting and lamination process followed by calcination (600 °C, 3 h) exhibited high activity for Remazol Brilliant Red F3B degradation. At this temperature, the interdiffusion between ZnO and TiO_2 greatly prevented the binary compound formation and coarsening of particles that favoured an efficient photocatalysis.[226] The formation of less active phases like Zn_2TiO_4 and $Zn_2Ti_3O_8$ reduced the activity of the composite at high calcination temperature (650-700 °C). The tricomponent ZnO-TiO_2-SnO_2 prepared by the sol-gel method using Sn(Zn)/Ti molar ratio of 0.05 and calcined at 500 °C (3 h) was beneficial for MO degradation compared to a composite obtained by solid state reaction under UV/visible light.[227] The XPS revealed the formation of Ti^{3+} species, indicating a lot of oxygen vacancies in the sol-gel composite. The TiO_2 has a CB edge sandwiched between ZnO and SnO_2 giving a "staggered" type-II heterojunction at the composite interface. Under the

light illumination, an electron transfers from ZnO to TiO_2 to SnO_2, while a hole migrates in the opposite direction to favour charge separation (Fig. 14). The loss of crystallinity and rutile formation at high Sn(Zn)/Ti molar ratio lowered the activity. In another study, ZnO-TiO_2-SnO_2 (4:1:1) synthesized via solid state reaction (calcined at 500 °C, 2 h) was remarkably active for MO degradation compared to TiO_2 and SnO_2, but has lower in activity compared to ZnO.[228] This situation was due to the presence of a highly active ZnO in association with a low active SnO_2 in the tricomponent system. The activity decreased with an increase in calcination temperature (≥ 700 °C), due to the nucleation of photoinactive inverse spinel Zn_2TiO_4 and Zn_2SnO_4 polymorphs and was completely inert after thermal treatment at 1300 °C (42 h), since all the oxides reacted to form solid solution $Zn_2Ti_{0.5}Sn_{0.5}O_4$.[228] The photocatalytic activity of ZnO NT arrays-$TiO_{2-x}N_y$ and ZnO hollow sphere-TiO_2 towards NO_x decomposition decreased with increase in the emission wavelength of the excitation source.[69,229] The vectorial electron transfer from takes place from ZnO CB to $TiO_{2-x}N_y$ (or TiO_2) CB, while hole transfers in the opposite direction to facilitate charge separation. In addition, additional energy level created by Ti_5O_9, binds the excited electrons and also enabled the exciton formation by the light with lower energy.[229]

The advantage of ZnO-TiO_2 stems from the high absorbance of ZnO and a better stability of TiO_2. The three binary compounds formed in this system are Zn_2TiO_4 (cubic), $ZnTiO_3$ (cubic or hexagonal) and $Zn_2Ti_3O_8$ (cubic),[230] and any of these solid compound nucleates *via* solid state reaction depending on the annealing ambient, crystal structure of ZnO and TiO_2 together with their relative content. As a consequence of structural resemblance, $Zn_2Ti_3O_8$ and $ZnTiO_3$ was formed with anatase and rutile respectively. Both $ZnTiO_3$ and $Zn_2Ti_3O_8$ are stable phases below 900 °C, while Zn_2TiO_4 is most stable above this temperature.[226] In fact, $Zn_2Ti_3O_8$ is known to be a defect form of inverse spinel structure of Zn_2TiO_4 because of missing Ti ions in the lattice.

(b) Photocatalytic activity of ZnO-SnO_2

The ZnO-SnO_2 NFs synthesized by a combined sol-gel and electrospinning technique showed a high activity for RhB degradation compared to the ZnO NFs and SnO_2 NFs, due to the arrangement of stable heterojunction and a large specific surface area.[231] The average grain size of ZnO (42 nm) in the composite was larger than that of a pure ZnO (30 nm), while an average grain size of SnO_2 (13 nm) in a coupled system was smaller against a pure SnO_2 (31 nm). These electronspun-NFs composite could be reclaimed easily by sedimentation without any loss of activity due to their 1D nanostructural property. A mesoporous network structured semicrystalline SnO_2-high crystalline ZnO was active for MO degradation.[232] This was due to the presence of more surface reaction sites, which favoured an adsorption and transportation of dye molecules. The TEM image revealed a multipod framework for the composite and each NP is attached to several other NPs, indicating the formation of a stable heterojunction. In another study, the degradation of MB using mesoporous ZnO-SnO_2 was collapsed in acidic medium and improved in basic conditions, which was rationalized on the basis of surface charge density of SnO_2 (PZC 4) and ZnO. Adsorption of cationic dye will be favoured on negatively charged metal oxide surface under alkaline medium.[233] A high roughness of ZnO-SnO_2 thin films was beneficial for MB degradation upon calcination (500 $^{\circ}$C, 1 h) with Zn:Sn atomic percent of 80:20. In addition, this composite film was very resistant to acid etching with respect to photostability.[234] The maximum photocatalytic activity of ZnO-SnO_2 prepared by co-precipitation method towards MO degradation was observed at 33.3 mol % of SnO_2 at an annealing temperature of 500 $^{\circ}$C (10 h).[235] The grain size of ZnO and SnO_2 was smaller in the composite compared to their respective pure phases, indicating that the mutual interference of

SnO_2 and ZnO on the particle growth dynamics. The activity reduced at a high temperature treatment (≥ 700 °C), as ZnO reacts with SnO_2 (4.8 – 95.2 mol%) to form a less photoactive Zn_2SnO_4, which was otherwise observed at 1000 °C in a solid state reaction method.[236] The uniform coating and tight decoration of SnO_2 NPs on ZnO NRs resulted in a high performance for RhB degradation. The PL investigation revealed a decreased UV emission for the composite compared to the bare ZnO NRs, which reflects spatial charge separation rooted from type-II band alignment.[237] An extremely high adhesion of SnO_2 NPs on ZnO NRs was observed even after ultrasonicating the composite in ethanolic medium. This composite was achieved by two step thermal evaporation approach; (i) ZnO NRs was obtained through the thermal evaporation of zinc powder; (ii) SnO_2 was coated on pre-fabricated ZnO NRs from thermal disproportionation of SnO powder.

$$Zn_{(s)} + O_{(g)} \xrightarrow{600\ ^\circ C} ZnO_{(s)} \qquad (55)$$

$$SnO_{(s)} \xrightarrow{800\ ^\circ C} Sn_{(g)} + SnO_{2(s)} \qquad (56)$$

Hydrogen generation was observed from dye sensitized SnO_2 (10-15 nm) attached to the large ZnO (~600 nm) particles under visible light in the presence of hole scavenger and Pt co-catalyst.[238] Based on the series of modifications, it was found that the premixing of ZnO and SnO_2 prior to dying, the presence of a dye on SnO_2 and Pt islands on ZnO favoured hydrogen evolution. A photon that is absorbed by a dye molecule on the surface of a SnO_2, injects electron that traverse across few SnO_2 crystallites without losing energy to reach ZnO CB at a distance of 120 nm from the ZnO surface, suggesting the involvement of hot electrons with ballistic transport. The electrons on ZnO CB are then captured by Pt islets to initiate water reduction.

$$2H_2O + 2e^- \rightarrow 2OH^- + H_2 \qquad (57)$$

The bandgap, work function and electron affinity of ZnO are 3.37 eV, 5.2 eV and 4.3 eV, while that of SnO_2 are 3.5 eV, 4.9 eV and 4.5 eV respectively. The VB of ZnO is positioned between CB and VB of SnO_2 and CB of ZnO is positioned above VB and CB of SnO_2. Accordingly, ZnO-SnO_2 heterojunction involves, the vectorial transfer of electron from ZnO to SnO_2 and hole transfer in the reverse direction. Hence, this heterojunction not only serves as a source of carriers but also act as a sink for electrons and holes. The XPS revealed ΔE_v=0.7±0.05 eV and ΔE_c=0.2±0.05 eV for this heterojunction.[233] The surface acid-base properties, low cost and cheap availability of SnO_2 and ZnO with compatibility of some specific crystallographic planes to form heterojunction would be very useful for further design of this bicomponent system.[239]

(c) Photocatalytic activity of ZnO coupled with other metal oxides

The ZnO-CuO prepared by coordination-oxidation-homogeneous coprecipitation method exhibited a better activity for MO degradation under UV-*vis* light.[240] The composite was prepared by using metallic copper as Cu^{2+} source, NH_3 as coordination agent, air as oxidizer and ammonium bicarbonate as precipitating agent along with ZnO. The change in the activity of the composite was in agreement with the analysis of particle growth dynamics. The activation energy for the growth dynamics at low (≤ 450 °C) and high temperature (≥ 450 °C) regions are 14.94 kJ/mol and 59.84 kJ/mol, respectively. At low temperatures, crystal particles with a small size, an incomplete crystal lattice, and many vacancies will be obtained leading to a low crystal grain growth activation energy, which contributes for a high photocatalytic activity. While grain growth will be rapid, resulting in the loss of surface area and surface activity at high temperature. Thus, the vacancies will be reduced and hence the crystal grain growth activation energy

increases. In addition, the ZnO-CuO was also effective for the treatment of real textile wastewater containing MO and MB dyes under the visible light.[241]

The ZnO-ZnO_2 with small ZnO_2 granules fused at the surface of a prismatic ZnO exhibited a significant activity for MO decomposition, due to the presence of either structural or energetic heterogeneity within the interfacial region of the composite.[242] As obtained ZnO_2 from the aqueous reaction of zinc sulfate and H_2O_2 under alkaline medium was less active due to its poor crystalline nature. The hydrothermal treatment (120-180 ˚C, 2 h) of ZnO_2 gradually transformed to ZnO and high photoactivity was noticed in the range of 140 – 150 °C, while pure ZnO obtained at 180 °C showed poor performance (Fig. 15). The difference in electronic band structure between ZnO and ZnO_2 (4.12 eV) results in a potential gradient at the interface and interfacial structural defects served as a trap site for excitons to suppress recombination.[242]

The ball milling of n-ZnO in water doped with p-$CaFe_2O_4$ exhibited a better activity for MB degradation, attributed to a stable integrated micro p-n heterojunction.[243] The activity increased with increase in the content of p-$CaFe_2O_4$ up to 1.0 wt.% and decreased thereafter, as the absorption of light and the generation of electron-hole pairs were lowered together with a decrease in space charge region on the particle surface. When the ball milling time were 3, 6, 12, and 24 h, degradation efficiencies are 50.8, 73.4, 78.7 and 75.6%, respectively. With an increase in the ball milling time, specific surface area and the number of active sites per unit weight of the catalyst increases, thus enhancing the activity. Beyond this optimum time, it is proposed that a fresh surface formed by the high energy ball milling possesses a robust surface energy and prefer to agglomerate with a loss in surface area. In the process of ball milling, the crystal lattice of $CaFe_2O_4$ and ZnO are vulnerable to severe plastic deformation that induces stress and strain. This creates a crystal lattice distortion and many defects are formed within the particles, which

will have high surface energy. Under this situation, the activation energy for the diffusion of elements decreases to a large extent and allows facile atomic or ionic diffusion among the elements at room temperature. When the activity of a powder system is sufficiently high, the collision between balls and the grains of powder will produce a rise in the interface temperature, which induces a coupling reaction between the semiconductors.[243,244] The ZnO-$ZnFe_2O_4$ was ineffective for MG degradation for all the contents of $ZnFe_2O_4$ both in thin film and powder form.[245] Interstingly, ZnO-$ZnFe_2O_4$ core-shell nanocable was active for RhB degradation under visible light. The nanocable arrays configuration are associated with large surface-to-volume ratio, leading to optical path increase of incident light in the structure and suppress reflection, thus enhancing the light absorption. In this composite, the unidirectional electron transfer takes place from excited dye to $ZnFe_2O_4$ CB to ZnO CB, while holes are left in VBM of $ZnFe_2O_4$. The degradation of RhB with composite involved both de-ethylation and destruction of chromophore, while only latter mechanism was observed with methanol.[246] The ZnO-Ag_3PO_4 at an optimum content of 3 wt.% Ag_3PO_4 prepared by the ball milling was active for RhB degradation under the visible light.[247] As evidenced by XPS studies, the ΔE_v and ΔE_c for this heterostructure was found to be 0.3 eV and 1.05 eV±0.05 eV, respectively. The reaction rate was suppressed with isopropanol compared to the benzoquinone indicating that the hydroxyl radicals were the dominant oxidative species in the degradation mechanism. During the photocatalytic process, the holes resided on ZnO VB induce oxidation reactions, while electrons accumulated on Ag_3PO_4 CB triggers hydrogen peroxide generation. It was proposed that the CB and VB levels of Ag_3PO_4 were positioned at 0.45 eV and 2.9 eV (vs NHE), respectively.[248] The bottom of CB was mainly composed of hybridized Ag 5s, 5p and small quantity of P 3s orbitals, while the top of VB constitute hybridized Ag 4d and O 2p orbitals.[247]

The ZnO-AZO thin film with a AZO thickness of 30 nm increased the degradation efficiency of RhB and MB, while it was lowered for 80-200 nm.[249] This was ascribed to IEF differences induced by dissimilarity in carrier concentration between AZO (1.5 x 10^{18} cm^{-3}) and ZnO single crystal (8.8 x 10^{16} cm^{-3}). The difference in the Fermi levels of AZO and ZnO single crystal gave rise to a built in potential of 0.07 eV, IEF with maximum intensity (E_m) of 5.2x10^4 V cm^{-1} and width of 27 nm. When ZnO is excited by UV light, most of the charge carriers are produced in a thin effective absorption layer, which is about a 100 nm below the surface.[250] Thus, IEF lies completely within the light absorption layer and the charge carriers are efficiently separated for 30 nm AZO film thickness. When the thickness is further increased (80 – 100 nm), part of IEF will be located in the effective absorption layer and thus, the separation efficiency will be near the edge of light absorption layer. Under this circumstances, only a few electron-hole pairs will be generated in the thickness zone of IEF, because of exponential attenuation of UV light (Fig. 16). In fact, AZO thin film with a higher thickness (200 nm) had a lower efficiency compared to ZnO itself, as the charge carriers are completely generated in AZO, which owns more recombination centers than ZnO single crystals.[249] The incorporation of In_2O_3 to ZNWs resulted in the visible light response and glucose oxidation *via* photoelectrochemical approach at a potential bias of 0.8 V.[251] The linear sweep voltammetry and EIS studies revealed the generation of larger number of charge carriers with charge transfer rate constant (3.23 s^{-1}) and a very low charge transport resistance (19083 Ω) for this composite compared to the pure ZNWs (1.41 s^{-1} & 47400 Ω). The In_2O_3 has a bandgap of 2.8 eV, with its both VB and CB are situated slightly above the corresponding energy levels of ZnO.[252] Under visible light, electrons will be excited from VB to CB of In_2O_3 and a transient photocurrent is generated leaving the holes to participate in glucose oxidation. Due to the high electron mobility and geometry of

vertically aligned ZNWs, the injected electrons are effectively collected as a result of reduction in the electron transport resistance distance in the photoanode. However, a high loading of In_2O_3 increases the shell thickness on ZNWs and creates a large number of grain boundaries. Thus, electrons in In_2O_3 have to travel a longer distance to reach the ZNWs, resulting in the increased charge transfer resistance and lower the separation efficiency.[251]

The small size and high surface-to-volume ratio of mesoporous spindle-like Fe_2O_3-ZnO core-shell contributed to faster RhB degradation under UV/visible light.[253] The electrons in the CB of α-Fe_2O_3 core transfers to the ZnO CB shell driven by decrease in the potential energy. Thus, the confined potential of excited electron-hole pair reduces their interaction with traps on the surface and environment. This heterostructure was obtained by the seed mediated growth route and the ZnO shell formation involved two steps; adsorption on the surface of monodispersed seeds and growth under a heat treatment (Fig. 17). The presence of spindle-like hematite seeds favours the growth of ZnO *via* heterogeneous nucleation, rather than forming separate nuclei by homogeneous nucleation. The gaps in single α-Fe_2O_3 seed is distributed between both the grain boundaries and the spindle-like particle is composed of small nanocrystals and overall particle surface is quite rough. This feature endows α-Fe_2O_3 seeds to have high adsorption capacity for zinc ions. The adsorbed zinc precursor reacts with NH_3 to form $Zn(OH)_2$, which transforms to a layer ZnO shell during the thermal treatment (550 ˚C, 2 h).[253] The ZnO-NiO (cubic) NFs exhibits a high activity for RhB degradation compared to their individual components.[254] Under UV light, electron transfers from CB of NiO to ZnO CB, while hole migrates in opposite direction. The p-NiO (E_g=3.5 eV) has high hole mobility and low lattice mismatch with ZnO, which benefits the formation of a stable p-n heterojunction.[255] In

addition, PL studies indicated a high concentration of oxygen vacancy defects for the composite that improves the charge carrier separation.[254]

7.2 Photocatalytic activity of ZnO-Metal sulphide

The sensitization of ZnO *via* electronic coupling with narrow bandgap photosensitizer is a viable approach to exploit the utilization of solar spectrum. The conventional charge transfer between narrow and wide bandgap semiconductors is beneficial to isolate the oxidation and reduction reaction, as the electrons and holes dwell on different semiconductor surfaces. For an efficient transfer of electrons between sensitizer and ZnO, CB energy level of ZnO must lie lower than the excited state or CB edge of the sensitizer. In this perspective, CdS with wurtzite polymorph is more desirable because of similar lattice structure with ZnO, thus establishing a close interaction between these two semiconductors.

The ZnO-CdS displayed an appreciable activity for RhB degradation under the simulated sunlight, attributed to an extended photoresponse and an increased charge carrier separation.[256] The nanostructures were composed of 3D flower-like ZnO microstructures coated with cubic CdS NPs. The composite preparation involved two stages: flower-like ZnO was dispersed in an aqueous solution of $CdCl_2$ by ultrasonic agitation to facilitate the adsorption of Cd^{2+} ions on the ZnO surface, followed by the addition of sodium sulphide, results in the uniform coating of CdS. Due to the rapid precipitation and low reaction temperature, a small size CdS NPs was formed. This coarse-surface structure enhanced the dye adsorption and diminishes the reflection of incident light to benefit the photocatalytic reactions.[257] The ZnO-CdS system has a "staggered type" type-II band alignment, which means ZnO CB is located between CB and VB of CdS.[258] Under the visible light, an electron migrates from the CB of CdS to ZnO CB, while holes do not

transfer in the opposite direction, as CdS VB being more cathodic than ZnO. The electrons accumulated on ZnO initiates dioxygen reduction, while the holes in CdS react with water adhering to its surface to generate hydroxyl radicals or they can also directly oxidize organic molecules. The performance was found to have dependence on CdS loading; with CdS prepared by 2.5 g L^{-1} $CdCl_2$ and 1.25 g L^{-1} of thiourea showed a high activity compared to other conditions.[259] The reaction rate suppressed drastically in the presence EDTA and slightly with dimethyl sulfoxide (electron quencher), indicating that holes are the main active species in the degradation mechanism. For a higher CdS loading (5.0 g L^{-1} $CdCl_2$ and 2.5 g L^{-1} of thiourea), the activity reduced due to the formation of $Zn_{1-x}Cd_xS$ ternary compound, which hinders the sensitization process by transporting the electrons from CdS to this transition layer, without being transported to ZnO due to the lower position of $Zn_{1-x}Cd_xS$ CB.[260] In this study, the composite was prepared with an aid of ultrasound irradiation. When a ZnO microsphere is added to the reaction system, the hydrogen and hydroxyl radicals are formed from the ultrasound induced dissociation of water molecules. The hydrogen radicals act as a reducing species and trigger thiourea decomposition to form S^{2-}, which reacts with Cd^{2+} to form CdS NPs. The ultrasound induced cavitations provide a clean ZnO microsphere surface for the adhesion of S^{2-} (or CdS), facilitating an intimate contact between the two semiconductors.

$$H_2O \rightarrow H^{\bullet} + OH^{\bullet} \quad (58)$$

$$2H^{\bullet} + RS \rightarrow H_2S + R^{\bullet}(RS = H_2NCSNH_2) \quad (59)$$

$$S^{2-} + Cd^{2+} \rightarrow CdS \quad (60)$$

$$n(CdS) + ZnO \rightarrow ZnO - CdS \quad (61)$$

Kundu *et al.*[260] also reported that minimum CdS loading (4.1 wt. %) resulted in the faster MB degradation, while large bandgap of CdS and decrease of surface hydroxyl groups on ZnO surface at high loading (5.4 – 11.7 wt.%) was detrimental. In the synthetic route, cadmium nitrate

was rapidly evaporated on ZnO NRs followed by the addition of Na_2S with varied concentration. The composite formation was controlled by two competiting processes: dissolution of precursor phase in aqueous solution and their conversion to sulfide. At a low concentration of Na_2S, the rate of sulfiding is much slower than the rate of dissolution and therefore most of the precursor film dissolves before being converted to sulfide phase. Conversely, most of the film is converted to sulfide phase as the conversion rate is much faster than the dissolution rate at a high concentration, while fine CdS NPs are formed on the substrate at an optimum concentration of Na_2S.[260] The controlled heterogeneous nucleation of CdS NPs on ZnO TPs resulted in stable heterojunction that was active for MB degradation under visible light.[261] The CdS formation on ZnO-TPs preceded *via* an ion-by-ion mechanism as DMF was used as solvent for the growth of CdS in the neutral environment. It is likely that the Cd^{2+} ions adsorbed on ZnO surface acts as a "nucleation seed" for CdS formation. The slow dissociation of thiourea with DMF enables to controls the S^{2-} concentration through temperature setting and also avoids bulk precipitation of CdS.[262] This synthetic route is an alternative way for preserving ZnO nanostructured morphology from the damages induced by the standard alkaline chemical bath deposition process and does not require the addition of any surfactants or passivating agents. Thus, superior activity originates from a well dispersed and relatively suitable coverage of CdS NPs on ZnO surface.

The core-shell NRA of ZnO-CdS, with shell thickness of 30 nm showed a high activity under the simulated solar light for RhB degradation.[263] The study of decay kinetics indicated that the average carrier lifetime of core-shell NRA is longer than that of uncoated ZnO NRs due to the charge separation, as the electrons resides in the core and holes accumulates in the shell. The time required for an electron transfer is about 18 ps, which is smaller than the electron lifetime in CdS.[264] Once the electron diffuse into the CB of ZnO, the probability of its decay is small

because there can be no free holes in the VB of ZnO under the visible light. This heterostructure was designed by surface functionalization of ZnO by citric acid followed by the slow addition of Cd^{2+} and S^{2-}, because the normal CdS exchange process is so fast that ZnO core can be destroyed during the deposition process. During the synthesis, citric acid adsorbs on the surface of ZnO NRs *via* carboxyl group with an outward orientation of –OH functional groups. The negative charges on the functionalized surfaces of ZnO attracts Cd^{2+} and thin $Cd(OH)_2$ layers were formed. After the addition of sodium sulphide, CdS shell layer is formed on the surface of ZnO NRs *via* substitution of OH^- by S^{2-} ions. With increase in the amount of citric acid, CdS shell layers became gradually uniform along with an increase in the shell thickness (Fig. 18). The well defined ZnO-CdS grown on indium tinoxide substrate was active for 3,4-dihydroxy benzoic acid degradation under the visible light.[265] In this study, CdS layer was thinner than the room temperature diffusion length of electrons, which facilitates the ballistic process of charge transfer pathways. Also, CdS layer was discontinuous and too thin to support the interfacial depletion layer. Hence, a macroscopic potential barrier does not exist at the ZnO-CdS interface. The ZnO-CdS was active for Eriochrome Black T degradation under visible light, wherein ZnO NRA were obtained by electrochemical deposition on FTO substrate and CdS was then coated by the chemical bath deposition.[266] The optimal loading of CdS corresponds to a deposition time of 40 min, at which ZnO-CdS showed a significant visible light response compared to a low deposition time (3 min) where the visible light response was not observed. Interestingly, a blue shift in CdS absorption was observed for the deposition time of 10-20 min, indicating that NPs were subjected to strain during the growth on ZnO. It was proposed that an initial voltage pulse and time is very important to get homogeneously distributed seed layer of ZnO for a subsequent growth of ZnO NRs on FTO substrate. In other words, ZnO NRs was grown in short clusters and

was deposited on primary ZnO crystals in the absence of a voltage pulse. A shorter time (0.5 h) leads to low seed density, while longer time (3 h) results in the formation of continuous layer of ZnO on FTO with initial voltage pulse. Contrarily, ZnO NRs deposited for 1.5 h had a high density, long length, small diameter with narrow size distribution and a smooth surface. Unfortunately, this composite was susceptible for photocorrosion after 2 h of degradation reactions.

The ZnO-ZnS core-shell NRs (with a molar ratio of ZnS/ZnO is 0.6) synthesized by water bath route (ZnO conversion to ZnO-ZnS *via* surface sulfidation) showed maximum hydrogen production under UV and solar light with quantum efficiencies of 22 and 13%, respectively from water-glycerol mixture.[267] The CB of ZnS lies more negative than ZnO, while VB of ZnO is positive than ZnS, facilitating the electron and hole transfer in the opposite direction. The hole can be trapped by surface hydrdoxyl groups, which later oxidizes glycerol to CO_2 and the electron on the ZnO surface reduces protons to hydrogen. A small energy gap difference between ZnS VB and O_2/H_2O energy levels, together with high oxidative power of surface chemisorbed hydroxyl groups on ZnS as well contributes to the overall efficiency. In addition, this composite was found be thermally active (40 – 80 ˚C) under UV light.[267] The ZnO-CuS obtained by decorating CuO on ZnO NTs, followed by the addition of thioacetamide (80 ˚C, 1 h) was active to decompose MB at neutral pH conditions under visible light.[268] The decline in degradation with silver nitrate and increase in reaction with ammonium oxalate (hole scavenger) suggests that electron driven hydroxyl radicals was found to be major pathway that actively take part in photocatalysis. The type-II band alignment between p-CuS and n-ZnO leads transfer of electrons from CB of CuS to ZnO CB, while holes in the VB of CuS oxidize water to generate hydroxyl radicals.

The heterostructuring of ZnO with lattice matched or dissimilar materials passivate the surface recombination centers and resist it from photocorrosion. The versatility of ZnO to get decorated by variety of semiconductors with distinctive morphology under different experimental conditions highlights its stable and suitable surface properties. In addition, formation of impurity phases, interdiffusion among the coupled components resulting in alteration of electronic energy levels and change in interfacial defect structure remains a great challenge to fabricate impurity free heterojunctions. The organization pattern, crystallographic structures, electron affinity/work function, charge carrier mobility, mechanical adhesion, band bending, nature of surface/interface/bulk defects, and shape of each component in an integrated heterostructure determines their physical-chemical-electronic properties and their performance.[216c] The heterostructure formation is limited by the band edge positions and poor interfacial structure of the composite. While the former can be overcome by a suitable choice of the material or by tuning the bandgap of the sensitizer, the latter still remains as a great task from the view point of creating a favourable interface structure. Since much of literature discusses on the growth of secondary phase semiconductor on prenucleated ones, the one pot synthesis involving simultaneous nucleation of both the semiconductors with a modified surface/interface needs to be further investigated for developing cost-effective approaches.

8.0 Modification with carbon structures

8.1 Doping with carbon (C-ZnO)

The carbon doping is reported to be very active for visible light induced photocatalysis and promotes the charge carrier separation by channelling the photoexcited electrons to nanosized carbons on the surface of catalyst.[269] Heating of zinc chloride and EG (160 $^{\circ}$C)

followed by calcination (600 °C, 2 h) resulted in C-ZnO which mineralized the HCHO under the irradiation of indoor fluorescent lamp.[270] After 60 min of irradiation, CO_2 concentration increased up to 780 ppm for C-ZnO and only 595 ppm was observed for N-TiO_2. This difference was attributed to the extended visible absorption edge (400-700 nm) for C-ZnO, while N-TiO_2 showed weak absorption at ~500 nm. In addition, PL revealed low intense signal for C-ZnO than N-TiO_2 suggesting effective charge carrier separation in the former case. The flower-like C-ZnO obtained from $Zn_5(CO_3)_2(OH)_6$ was active towards RhB degradation under visible light. This was attributed to high oxidative powder for C-ZnO as a result of downward shift in the energy band structure and to its organized morphological features that enhanced the light absorption due to multiple reflection of trapped incident light. The decline in the activity at higher thermal treatment (> 500 °C) was due to the oxidation of lattice carbon and collapse of mesoporous structure.[271] The C-ZnO obtained from a solution of zinc nitrate, HMT and Vitamin-C through heating (95 °C, 1 h) and calcination (500 °C, 2 h) exhibited the visible light activity for Orange II degradation.[272] The rod-like structure for ZnO was observed with HMT, while the aspect ratio of rods decreased with the addition of Vitamin-C, indicating the supressed growth along [001] direction.[273] The $–COO^-$ and –OH groups of Vitamin-C adsorb onto the positively charged Zn^{2+} (0001) surface, thus blocking the contact between growth units and (0001) crystal surface. Under these conditions, growth along the six symmetric directions (nonpolar plane) was enhanced. During calcination, ZnO crystallizes and combustion of carbon takes place followed by rearrangement of host-guest atoms to render the substitution of carbide ions at lattice oxygen sites.[272] The visible light performance of carbon doped strings of ZnO was demonstrated in 4-NP degradation and photoelectrochemical water splitting.[274] The efficiency of bare ZnO (0.016%)

was lower than for C-ZnO (0.18%). The efficiency of water splitting was calculated using the formula;

$$\eta = \frac{I\,(1.23 - V_{app})}{P_{light}} \qquad (62)$$

where V_{app} is applied voltage, I is measured current density, and P_{light} is the power density of illumination. In this study, the surface reconstructed monolayers of poly(styrene-*block*-2-vinylpyridine) diblock copolymer (PS-*b*-P2VP) inverse micelles were used as template to obtain the ZnO NPs under the oxygen plasma. The partially removed polymer was then cross-linked by UV light under vacuum followed by carbonization (600 $^{\circ}$C, 1 h) in an inert atmosphere leads to the carbon doping as carbonate species in ZnO lattice. This creates a new energy level above the VB *via* hybridization of O 2p and C 2p orbitals to give visible light response and the carbon network on the surface may act as channel to divert excitons, consequently supressing the recombination pathways (Fig. 19). The 3D mesoporous C-ZnO obtained by solvothermal route (160 ˚C, 24 h) in EG using glucose as a carbon source showed a maximum adsorption capacity of CR (162 mgg^{-1}) and a high visible light activity for the degradation of CR and RhB.[275] Based on experimental studies, it was concluded that both glucose and EG played an important role in the formation of hamburger-like nanoarchitecture for C-ZnO. The anionic functional group of the EG and glucose interacts with (0001) plane of the ZnO to lower its surface free energy, resulting in an equiaxed or spherical morphology. The complex mixture of the aromatic compounds and the oligosaccharides formed as a result of the chemical reactions of glucose under solvothermal condition increases the viscosity of the resulting solution (polymerization step). The growth of a 3D "twinning superstructure" occurs at this juncture, which takes place by the continuous adjoinment of additional oligosaccharides on the surface of ZnO subunits. This

kind of twinning is allowed due to the adsorption of polymers, which counterbalance and perhaps overcompensates the like charges on these faces, and the self assembly of these subunits may continue *via* stacking of their polar faces of the opposite charge facing each other.[276] As the heating time is extended, the carbonaceous polysaccharides adhered on the Zn^{2+} transforms to C-ZnO, with carbon atom occupying interstitital sites in ZnO. Thus, the glucose confines the growth of ZnO and also serves as an assembly agent to construct NPs into a 3D hamburger-like mesoporous superstructure.

The doping of carbon at substitutional/interstitial or as carbonate ion results in only visible light absorption, and its role as charge carrier traps is still far from critical discussion. Similar to nitrogen dopant, the expulsion of doped carbon from ZnO lattice at high temperature treatment is the major drawback for this approach. Therefore extra caution is required to balance between carbon doping and crystallization during the preparative step.

8.2 Modification with other carbon forms

Highly crystalline 1D ZnO grown on CNFs substrate without any aggregation showed better performance for RhB degradation.[277] The photogenerated electron may freely move towards the surface of CNFs and the VB holes migrate to the surface and reacts with the surface adsorbed water or hydroxyl groups to produce the hydroxyl radicals. The PL studies also revealed the efficient charge carrier separation in this heterostructure as conductive 1D CNFs serves as an ideal electron pathways.[278] The coverage density of ZnO NPs coating on the CNFs surface was tuned by adjusting the molar ratio of zinc precursor to CNFs during the hydrothermal synthesis (180 ˚C, 12 h). The solar light activity of ZnO-activated carbon increased with increase in pH up to 9, and remains constant even though the adsorption of Direct Blue 53

molecules is negligible at alkaline medium.[279] It was concluded that the degradation not only takes place on the catalyst surface but also near to its vicinity. The synergistic effect was attributed to the adsorption of dye on the activated carbon, which later diffuses to ZnO located at the pores followed by subsequent degradation (Fig. 20). The carbon coated ZnO NRs obtained by the microwave-assisted method resulted in a faster decomposition of MB under visible light.[280] This was achieved by modifying the surface of ZnO NRs by amino groups through the interaction with (3-aminopropyl)triethoxysilane and then grafted by glucose followed by microwave irradiation to stimulate the transformation of glucose into carbon (Fig. 21). The high activity was attributed to: (i) amorphous carbon has good adsorptive capacity and hence MB concentration can be enriched on the ZnO surface for photocatalytic reactions. The driving force for dye adsorption is mainly through the interaction between graphitic carbon and aromatic rings of the dye molecules.[281] (ii) coating of a low work function amorphous carbon (3.5 – 4.0 eV) improved the light absorption properties of ZnO. The CB electrons of ZnO move freely to the surface of carbon particles, directing the charge carriers to flow in the opposite direction; (iii) uniform and well dispersed carbon coating increased the corrosion resistance for ZnO giving a better stability.[280] The bare ZnO lost its photocatalytic activity after calcining at ≥ 700 ˚C, while ZnO-C retained for activity even at 1000 ˚C, indicating that surface carbon improved the thermal stability of ZnO.[282] The ZnO-C prepared by simple solvothermal treatment (160 ˚C, 24 h) of zinc acetate and ethanol with iodine was active for RhB degradation under visible light.[283] The iodine promoted the oxidation of ethanol and resulted in the formation of carbon, which self-assembled with ZnO to form composite spheres. The extent of carbonization and hence the photocatalytic activity was influenced by the amount of iodine used, and optimum was found to be 0.2 g (carbon fraction is 30%). During the process, iodine catalyzed both alcoholysis of zinc ions and

carbonization of ethanol. A controlled experiment with only iodine and ethanol did not initiate any carbon formation, signifying that carbonization of ethanol occurred due to the combining effect between iodine and zinc ions. The surface hybridization of ZnO with graphite-like carbon layers suppressed the grain coalescence and the crystal growth giving an exceptional photo and thermal stability.[284] The degree of graphitization was dependent both on graphitization temperature and the mass ratio of carbon in the synthetic procedure, and the best ratio of 16.9 wt. % was reported towards MB degradation even at extreme pH conditions. At lower carbon content, coalescence and the crystal growth was not efficiently suppressed, while high carbon content shielded the light reaching the catalyst surface, with both effects hampered the photoactivity. The degradation mechanism was mediated by the hydroxyl radicals on the ZnO surface, while it was mediated by a direct reaction with holes on the surface and in the solution bulk attributed to an enhanced adsorption of MB on the surface of ZnO-C.

The coating of carbon enhances the adsorption of pollutant on catalyst surface simultaneously facilitating both adsorption and photocatalysis. It is interesting to note that carbon coating on ZnO surface can be achieved by cheaply available precursors like citric acid, alcohols and polysaccharides. The change in surface structure of ZnO after carbon coating and their influence in degradation reactions require indepth study.

8.3 Modification with graphene and g-C_3N_4

Materials with delocalized conjugate π-structures are extensively investigated in electron transfer processes, as they reduce recombination *via* capturing the photogenerated electrons from CB of semiconductor and transport them to adsorbed oxygen for the production of reactive oxygen species. A delocalized π-structure material coupled with a semiconductor serve as a unique “dyade” type of structure forming a common conjugated system and improves the

photocatalytic performance in the entire spectral range.[285] As a rising star of carbon family, graphene composed of single, bi and few layers of carbon atoms forming six membered rings has gained attraction because of its multifaceted physicochemical and optoelectronic properties. In particular, its unique 2D structure and plenty of π-electrons in graphene provides a suitable platform for the growth of stable inorganic semiconductors.[286] It is reported that the confinement effect of graphene plane would favour the dispersion and stability of ZnO, while ZnO particles on graphene sheet will act as a kind of chemical obstacle to prevent the graphene from agglomeration and retains its high specific surface area.[287]

The ZnO-FGS in which ZnO NPs were homogeneously dispersed on FGS showed a high activity for R6G decomposition.[288] This composite was prepared by a thermal treatment method, wherein the addition of PVP stabilized GO sheets and promoted the nucleation of ZnO followed by their deposition on the carbon sheets. An increase in the photon absorbance caused by FGS and the electron transfer pathways between a highly crystalline ZnO and FGS contributed to overall efficiency. The degradation of MB and MO with the ZnO-GO under the visible light was further improved by annealing under N_2 atmosphere (400 $^{\circ}$C, 2 h).[289] The composite preparation involved two distinctive stages: (i) the dissolution of zinc chloride in GO suspension renders Zn^{2+} ions to get adsorbed on the surface of GO sheets due to their bonding with negatively charged oxygen containing functional groups *via* electrostatic force; (ii) the crystal growth units of $Zn(OH)_4^{2-}$ and ZnO^{2-} formed under alkaline medium may combine with the functional groups of GO sheets *via* an intermolecular hydrogen bonding or coordinate bonds that acts as anchor sites for ZnO NPs. With subsequent heating at 90 $^{\circ}$C (6 h), the ZnO nuclei will be formed. The degradation mechanism initially involved the excitation of MB followed by an electron transfer to ZnO CB *via* GO sheets, which are later captured by adsorbed oxygen to produce reactive

oxygen radicals. Finally, MB^{*+} is degraded by itself or by the attack of reactive oxygen species (Fig. 22). Further, a large surface area and hierarchical porosity of flower-like ZnO anchored onto GO enhanced the adsorption and mass transfer of dyes and oxygen species.[289] The fabrication of ZnO-graphene *via* solvothermal reaction (150 ˚C, 8 h) of Zn-EG-Ac complex and GO in ethanol solvent was beneficial for RhB decomposition.[287] The reaction system possessed the following characteristics: (i) abundant functional groups in Zn-EG-Ac complex interacts with the functional groups (-COOH, -OH) of GO and hydrolyse *in situ* on GO to form a well dispersed ZnO NPs without using an external alkali; (ii) Zn-EG-Ac has relatively high stability in ethanol, which promotes the growth of ZnO on graphene rather than the homogeneous nucleation in the reaction medium; (iii) ethanol facilitated GO reduction and also slowed down the liberation of Zn^{2+} to produce a fine ZnO NPs tightly decorated on graphene. In another study, ZnO-graphene composite prepared by chemical deposition route was also active for RhB degradation under UV/visible light.[290] The redox potentials of RhB and RhB* are 0.95 V and -1.42 V (*vs* NHE), while the work function is -5.45 and -3.08 eV (*vs* vacuum), respectively. Comparing the potential of CB (-4.05 eV) and VB (-7.25 eV) of ZnO with work function of graphene (-4.42 eV),[291] the direct electron transfer from RhB* to graphene seems to be thermodynamically more favorable (Fig. 23).[292] In addition, the composite also served as filtration membranes to remove the dye molecules from water. The graphene sheets densely decorated by the ZnO NS resulted in the good combination for Cr(VI) reduction.[293] The photogenerated electron reduces Cr(VI), while the hole oxidizes water molecules.

$$Cr_2O_7^{2-} + 14H^+ + 6e^- \rightarrow 2Cr^{3+} + 7H_2O \quad (63)$$

$$2H_2O + 4h^+ \rightarrow O_2 + 4H^+ \quad (64)$$

The presence of graphene increases the light absorption intensity as a result of increase in the surface electric charge of oxides in the composite and modifies the charge carrier dynamics during an irradiation, thus promoting the activity. The activity decreases at a higher content of graphene (> 1.0 wt.%) due to: (i) graphene absorbs the UV light and there exists a light harvesting competition between ZnO and graphene; (ii) an excess graphene acts as a recombination centres.[294] The ZnO-graphene obtained *via* heat treatment of the ZnO-GO (200 °C, 2 h) containing 2.5% graphene exhibited a high visible light activity for MB degradation compared to the ZnO-MWCNTs and retains 80% of the initial activity even after five times of recycling.[295] The TEM images revealed that both sides of GO sheets are closely coated with ZnO particles (average size of 5 nm) in relatively high density to form a sandwich-structure stacks layer upon layer, that favoured a strong electronic interactions. The PL studies revealed that the presence of graphene eliminates the surface defects of ZnO particles. However, the ZnO particles will peel off the graphene sheets and the graphene structure will be destructed slowly during the durability test. Also, the impurity or inorganic anions occupy the active centers and hampers the photocatalyst performance.[295]

The ZnO-graphene hybrid containing 2 wt.% of graphene obtained *via* reduction of GO with hydrazine was visible light active for MB degradation, accompanied by the participation of both superoxide and hydroxyl radicals in the solution as well as direct hole oxidation.[296] By this *in situ* reduction method, ZnO NPs could efficiently separate the graphene sheets and retard the restacking of graphene sheets. The defect sites on GO served as nucleation sites for ZnO, resulting in less agglomerated particles. For this method, Gayathri *et al.*[297] reported the optimum amount of ZnO (600 mg of Zn^{2+} ion precursor in the synthesis step) showed higher activity compared to low (300 mg) and high (900 mg) amount, despite the other catalysts showed very

low PL intensity. The increase of Zn^{2+} concentration makes the ZnO NPs to stick to the surface of graphene sheets and prevented the graphene sheets from combining as a result of weak van der Waals forces between the graphene layers. However, graphene sheets stacked together at low concentration of Zn^{2+} and appears like ZnO on multilayered graphene, due to the loss of 2D planar structure.[297] The microwave assisted irradiation method to synthesize ZnO-RGO in diethylene glycol medium was powerful for the decolorization of self-photosensitized dyes (RhB and MB) under the visible light, but was ineffective for the benzoic acid degradation.[298] This result indicated that the decolorization of dyes is mainly due to the photosensitization process, rather than the excitation of ZnO-RGO nanohybrids. In this case, electron transfer takes place from the dye* to ZnO or through RGO, which contributes to an effective charge carrier separation. A high loading of ZnO was detrimental (0.0092 – 0.0115 M zinc acetate in the preparation step), as it may reduce the quantity of photogenerated charges due to unfavorable morphology and poor charge carrier transfer through ZnO nanocrystals. The ZnO-RGO synthesized by UV-assisted photocatalytic reduction of graphite oxide by ZnO in ethanol was efficient for Cr(VI) ion removal, due to an increased light absorption intensity and range with reduced carrier recombination.[299] In addition, this composite also served as a good adsorbent for colour removal under the dark conditions.[300]

The soft material g-C_3N_4 (E_g 2.7 eV) as an analogue of graphite, possesses stacked 2D structure, with tri-s-triazine building units connected with planar amino groups in each layer and weak van der Waals forces between layers. It is exceptionally stable under light illumination in the wide pH range (0 – 14), thus making it potential candidate for many green energy applications.[301,302]

The ZnO hybridized with g-C_3N_4 (ZnO:g-C_3N_4) *via* the monolayer dispersion method showed a high activity for MB degradation under UV/visible light at 3% loading of g-C_3N_4.[303] This enhancement was mainly due to π-stacking type adsorption between MB and g-C_3N_4, was similar to the conjugation between graphene and aromatic molecule. The MB can be adsorbed on g-C_3N_4 surface with offset face to face orientation *via* π-π conjugation until an adsorption-desorption equilibrium is reached. The superior adsorption capacity was a worthy complement for the high activity of hybridized g-C_3N_4:ZnO. The suppression of dye degradation with EDTA and TBA confirms the dominant involvement of holes and hydroxyl radicals under the UV and visible light photocatalysis, respectively. Under UV light, hole transfers from ZnO to HOMO of g-C_3N_4 resulting in an efficient charge separation and also suppresses the photocorrosion of ZnO. The g-C_3N_4 absorbs the visible light to induce π-π* transition from HOMO to LUMO. The LUMO potential of C_3N_4 is -1.12 eV,[304] which is more negative than the CB of ZnO (-0.5 eV) and the excited electrons is directly injected to the CB of ZnO. The g-$C_3N_4^+$ radical could accept electrons from the fragments of MB degradation and returns to the ground state.[303] The formation of chemically bonded interface between g-C_3N_4 and ZnO originates from condensation reaction between the triazine amino group and the surface hydroxyl groups of ZnO. The concentration of Zn^{2+} ion after the degradation of MO and 4-NP under the visible light using this composite was found to be much lower than the pure ZnO, attesting its long term stability in aqueous solution.[305] The activity increased with an enhancement in the ZnO content upto 15.6 wt.% and reduced at higher values (58.1 wt.%), which was attributed to the unsuitable ratio between the coupled semiconductors and to the poor visible light response of the composite. In another study, Shifu and co-workers reported that optimum amount of ZnO and g-C_3N_4 was 15 and 5 wt.% respectively, for the ZnO:g-C_3N_4 prepared from ball-milling and deposition-

precipitation methods respectively.[306,307] This was attributed to the balanced introduction of the trap sites for charge carriers that prolongs the carrier lifetime. The reaction kinetics with different radical scavengers declined in the order; benzoquinone > isopropyl alcohol > ammonium oxalate, confirming the pivotal role of superoxide radicals in the RhB decomposition mechanism. However, the hydroxyl radical generation as evidenced by PL spectroscopy indicates that superoxide radical so formed transforms to hydroxyl radicals by a series of reactions, and contributes to complete mineralization.[306,307] The holes generated in g-C_3N_4 cannot oxidize OH^- or H_2O to hydroxyl radicals, because the position VB of g-C_3N_4 (1.57 eV *vs* NHE) is more negative than the standard redox potential of $E^o(OH^{\cdot}/OH^-)$ = 1.99 eV *vs* NHE.

The ZnO:mesoporous g-C_3N_4 core-shell structure was also active for MB degradation under UV/visible light.[308] The activity was closely related to thickness of shell, heterojunction interfaces and core-shell structure induced by lattice match between the two components. The formation processes for the core–shell structure takes place through two steps: mesoporous g-C_3N_4 is exfoliated into sheet-like nanostructures *via* ultrasonication in methanol solvent, and later these sheets gets uniformly decorated on the ZnO surface to minimize the surface energy. The photoactivity increased with loading of g-C_3N_4 up to 4 wt. % under UV light, while activity increased up to 20 wt. % under visible light. The increase in shell thickness shields the UV light photons reaching the ZnO surface, while it improves the visible light absorption of the composite to benefit the charge transfer at heterojunction interfaces. The mesoporous structure easily permits the UV light to reach ZnO, compared to bulk g-C_3N_4. The optimal amount of ZnO in ZnO: mesoporous g-C_3N_4 was found to be 24.9 wt.% under visible and solar light towards MB degradation.[309] In this case, ZnO was allowed to nucleate and uniformly disperse on the mesoporous g-C_3N_4 sheets under solvothermal conditions (160 ˚C, 24 h). The holes were found

to be major oxidant responsible for pollutant degradation compared to hydroxyl and superoxide radicals. Instead of bulk g-C_3N_4 with a big sheet of lamellar structure, mesoporous g-C_3N_4 with an open crystalline pore wall and large surface area will be more beneficial in photocatalysis.[308,309] The C-ZnO:g-C_3N_4 showed high activity towards MB degradation under visible light, at 50.7 wt.% g-C_3N_4, corresponding to the homogeneous hybridization between ZnO and g-C_3N_4 (Fig. 24).[310] This is the first report to realize on simultaneous carbon doping and heterojunction formation of ZnO with g-C_3N_4. In this work, high temperature treatment of zinc nitrate and dicyandiamide initiated the formation of g-C_3N_4 and ZnO respectively through the thermal decomposition. Meanwhile, dicyandiamide adhering to the surface of ZnO NPs undergoes combustion and subsequent atomic rearrangements (Zn, C and O), enabled the substitution of carbon for oxygen in bulk of the lattice.

The electronic coupling of ZnO with g-C_3N_4 may be an ideal system to promote the charge carrier separation due to their well-matched overlapping band structure. The activity seems to be very sensitive on the content of both ZnO and g-C_3N_4 in the composite and preparative methods seems to be decisive factor in governing the photocatalytic pathways. The relative tuning of individual component and the decoration of g-C_3N_4 on varied morphologies of ZnO still requires further research.

8.4 Modification with CNTs, fullerenes and CQDs

The favourable bandgap energy level alignment in ZnO-MWCNTs-CdS resulted in the high photocurrent density (0.25 $mAcm^{-2}$) compared to ZNWs-MWCNTs (0.10 $mAcm^{-2}$) and CdS-ZNWs (0.20 $mAcm^{-2}$) under solar light.[311] In this bandgap configuration, unidirectional electron transfer takes place from CdS to ZNWs to MWCNTs to favour separation and the

photocurrent collection. The CdS serves as an electron sensitizer or relay, while ZNWs and MWCNTs acted as an electron sink (Fig. 25). The electrons from ZnO CB are trapped by MWCNTs *via* inductive effect that promotes the interfacial electron transfer process. Such a growth of ZNWs on MWCNTs improves the active surface area enhancing the photon absorption, while NW configuration affords conductive pathways towards the charge carrier transfer process. The MWCNTs possess more landing sites for the adhesive growth of NWs and the space between each NT would be beneficial for its dispersion. The photocurrent of ZNWs-MWCNTs was higher under UV light compared to solar light, as the extra excitons photogenerated at the nanocomposite-electrolyte interface intensifies electric field produced in the depletion layer, which further assists the electron transport processes.[312] The ZnO (34%)-MWCNTs was effective in cyanide removal under 355 nm UV light generated by the third harmonic of Nd:YAG laser.[313] The structural model proposed indicates that the zinc atom is aligned closer to the oxygen atom of carbonyl group, while an oxygen atom of ZnO remain close to the hydrogen atom of hydroxyl group on functionalized MWCNTs (Fig. 26). The former is possible as the electron density on oxygen atoms is shared with zinc which has electron affinity, while the latter is favoured because of hydrogen bond formation. In such kinds of hetero interphase interactions, attractive van der Waals forces play a significant role. The cyanide removal rate was enhanced with the laser energy (60 to 200 mJ), while declined with an increase in the pH values (4-12). When the laser energy is increased, the incident photon flux increases in the solution and facilitates the generation of more charge carriers. The PZC of functionalized MWCNTs was 4.9 and hence an efficient adsorption-degradation was observed at acidic pH. With an increase in pH, both MWCNTs and ZnO becomes negatively charged and the cyanide experiences repulsion from the catalyst surface.[313]

The increased light absorption and high surface energy of the ZnO-TiO_2-CNTs facilitated both adsorption and reduction of Cr(VI) ion.[314] The CNTs served as wires connecting different ZnO NS and the TiO_2 NPs, and also promotes the electrons to flow freely throughout the structure without any scattering from atoms or defects (ballistic transport).[315] The IEF at the surface of the composite and a stepwise structure of the band edge levels constructed leads to the electron transfer from ZnO to TiO_2 to CNTs, while hole traverse from TiO_2 to ZnO. The increase of CNTs loading (4 wt.%) competes with photon absorption with TiO_2 or ZnO and hampers the dispersion of metal oxides on CNTs surface, besides promoting the recombination process.[316] The fabrication of MWCNTs doped ZnO (Zn-O-C bond) by electrospinning method was positive for MB degradation under UV/visible light. Under UV light, electrons from ZnO CB move freely to MWCNTs, while MWCNTs serves as a sensitizer by absorbing the visible light and transfers the electrons to ZnO CB.[317] The positively charged MWCNTs remove an electron from VB of ZnO leaving a hole. The oxidation of MWCNTs with concentrated acid and the presence of surface alcohol, ketone and the acid groups enhanced the adsorption of dye on the composite surface, thus favouring an efficient photocatalysis. The ZnO:N-CNTs exhibits better activity compared to ZnO-CNTs for the degradation of benzoic acid and RhB under visible light.[318] The composite activity with respect to crystallite size of ZnO followed the sequence; 9.5>7.3>5.4>4.2 nm. The relative position in the CB of N-CNTs allowed transfer of electrons to ZnO, and that defects introduced by nitrogen doping might have separated the charge carriers. The Pd-ZnO:MWCNTs at an optimum ratio of 0.08:1.0:0.04 was successful in reducing Hg(II) with excellent recyclability under visible light.[319] The introduction of CNT and Pd prevented the ZnO NPs from agglomeration and that ZnO was strongly attached to the surface of CNTs

network. The Pd doping and CNT incorporation induced visible light response, while the large surface area of the composite provided more active sites for Hg(II) reduction.

The hybridization of C_{60} at a loading of 1.5% on the ZnO surface enhanced the activity for MB degradation and that the photocurrent generated remained constant even after prolonged UV illumination (20 – 35 h).[320] The CB energy level of ZnO (-0.5 V *vs* NHE at pH 7) thermodynamically favours electron transfer to the C_{60} molecules (E $C_{60/}$ C_{60}^{-} is -0.2 V) and a delocalized conjugated π-system of C_{60} promotes facile migration of electrons because of minimal changes in the structure and solvation associated with the process.[321,322] The crystal structure of ZnO was changed to $Zn_5(OH)_6(CO_3)_2$ after a prolonged illumination, while the pristine phase was retained for the composite suggesting that C_{60} inhibited the photocorrosion of ZnO *via* deactivating the surface oxygen atoms. The ZnO-CQDs were beneficial for the degradation of toxic gases (benzene and methanol) under the visible light.[323] The CQDs loaded on ZnO surface forms "dyade" structure providing an access to photoinduced charge transfer pathways. At the dyade structure, the photoinduced electrons are transferred to joint charge transfer states located at the CQDs, while holes accumulates electrically and structurally near ZnO. The electrons can be shuttled freely along the conducting network of CQDs and combines with adsorbed oxygen to produce superoxide and hydroxyl radicals in the solution. Also, the π-interaction between conjugated structure of CQDs and aromatic pollutant is beneficial to enrich its concentration on the composite surface.[324] In addition, CQDs with upconversion PL properties converts the longer wavelength light to a shorter wavelength resulting in the bandgap excitation of ZnO, consequently facilitating the generation of more charge carreirs (Fig. 27).

The modification of ZnO with various carbon nanostructures like activated carbon, amorphous carbon, graphitic carbon, CNFs, graphene, RGO, g-C_3N_4, fullerenes, CNTs and

CQDs improves both photoactivity and the stability of ZnO during photocatalytic reactions. In few cases, these carbon nanostructures serve as support for the growth of ZnO nanocrystallites or ZnO might act as substrate for the growth of these carbon forms. The excellent capacity of carbon nanostructures to enrich pollutant concentration on the catalyst surface and their robust capacity as electron conducting channels allows more carriers to participate in degradation reactions. These semiconductor-carbon composite nanostructures are expected to dominate in the wastewater purification in near future.

9.0 Reactivity of exposed polar and non-polar facets

It is widely accepted that the photocatalytic reaction occurs at the catalyst surface-pollutant interface. Thus, the morphology of catalyst affecting the surface atomic rearrangements and coordination, which modulates the crystal facets in different orientations play an important role in the photocatalysis.[325] The difference in the surface atomic configuration results in a distinct capacity to adsorb oxygenated species and the target molecules. Such a speculation has given the impetus to explore relationship between surface orientation of ZnO and their photocatalytic efficiency.

Compared with non-faceted ones, ZnO with hexagonal faceted prism (3 – 4 nm) showed a high performance for MB degradation, which was ascribed to the large surface area and the oxygen vacancy defects that promoted an efficient charge transfer process.[326] The ZnO with high degree of exposed {0001} facets embedded in flower-like matrix was active for RhB degradation compared to ZnO NRs (with fewer exposed {0001} facets) and platelets (with an equal number of Zn-{0001} and O-$\{000\bar{1}\}$ facets) under the visible light.[327] The origin of visible light activity was attributed to the polar surface induced oxygen defects like oxygen vacancies or interstitial

oxygen.[31] Furthermore, flower-like matrix possess a high degree of dispersion and prevented the aggregation of ZnO NPs, thereby improving the stability. The flower-like ZnO microarchitecture built by the self assembly of dense NS with ultrathin thickness of 5 nm and a large population of polar (0001) planes exhibit a high performance for MO degradation compared to other morphologies such as NPs, NRs, and NS.[328] These NS were obtained by citrate-mediated hydrothermal treatment in the presence of zinc nitrate and HMT. The addition of citric acid changes the orientation of ZnO from (0001) to $(10\bar{1}0)$, followed by morphological transformation from NR to NS and the main exposed surface changes from nonpolar to polar facets, attributed to its complexation on (0001) surface. This size quantized NS promoted the dye adsorption, enhanced the light harvesting capacity and efficiently channelized the carriers from bulk to surface.[329] The grid-like or net-like arrangement of NS retained their structural integrity even after vigorous ultrasonication (50 min).

The influence of ZnO morphology towards RhB degradation followed the order: cones > bullets > plates > rods, while the activity of exposed crystal facet shown the trend; $\{10\bar{1}1\} >> \{0001\}, \{10\bar{1}0\}$.[330] The morphologies and crystal facets was controlled by varying the reaction temperature and benzylamine/Zn^{2+} ratio, with benzyl amine serving as a reactant and the capping agent to stabilize $(10\bar{1}1)$ planes. Based on a model, it was proposed $\{10\bar{1}1\}$ facets possesses ridge-and-valley topography with oxygen termination, while the surface oxygen atoms alternate between two-coordinated and three-coordinated in nature. Since low coordinated oxygen atoms are generally saturated by hydrogen atoms *via* O….H-O-H hydrogen bond formation, they generate dense hydroxyl radicals in the solution. The ZnO nanoplatform with an exposed $\{0001\}$ facet showed a higher photocatalytic activity compared to humburger-like having $\{10\bar{1}0\}$ facet.[331]

The former was obtained by adding an aqueous solution of NaOH to zinc acetate, while an addition of sodium citrate resulted in latter morphology under the hydrothermal conditions (160 ˚C, 5 h). The concentration of growth units involved in the nucleation and growth was reduced by the complexation of citrate ion with Zn^{2+} ions.[332] In addition, a longer organic molecular chain of citrate anions makes ZnO growth units loosely spread in the reaction solution leading to the formation of a bigger and looser hamburger-like morphology. The ZnO nanoplates with a higher proportion of polar to nonpolar surfaces induced a rapid generation of H_2O_2 under UV irradiation lasting for 730 min compared to NRs, microrods and dumb-bell shaped, which is in consistent with their respective area of polar faces.[107] Recently, Bopella *et al.*[333] also reported that the performance of ZnO for MB degradation increased with increase in the proportion of polar to non-polar facets. The ZnO NRs with cone and small aspect ratio showed superior performance for MO degradation compared to the short-and-fat microrods and NRs with cone and large aspect ratio.[334] The control over the shape was achieved by varying the reaction temperature and time in the hydrothermal reaction of zinc foil-zinc acetate-H_2O sytem. The formation of NRs with a cone originates from the change of $V_{(0001)}$ and $V_{(01\bar{1}0)}$ during the growth. The crystalline nuclei grew into rod-like structure (120 °C, 2 h), as $V_{(0001)}$ will be larger than $V_{(01\bar{1}0)}$. The diffusion rate of zinc-hydroxyl complexes and zinc acetate in the solution will be slow and results in the concentration gradient between Zn-(0001) and O-$(000\bar{1})$ planes. As a consequence, the concentration of zinc-hydroxyl complexes and zinc acetate will be maximum around the top of NR and lower around the root. Thus, $V_{(01\bar{1}0)}$ on the top of NR was lower than that of its root, resulting in cone-like structure. With an increase in temperature (185 °C, 2 h), the diffusion rate between the reactants increases and the concentration gradient decreases resulting

in NR with a cone and large aspect ratio. The formation of a short-and-fat microrod (120 °C, 6 h) originates from the small difference between $V_{\{0001\}}$ and $V_{(01\bar{1}0)}$.[334]

The prismatic aggregates of ZnO calcined at 800 °C (4 h) with $\{10\bar{1}0\}$ facet demonstrated the highest activity for CH_3CHO decomposition.[335] The SEM results revealed that the surface exposed crystal faces or the ratios among the exposed crystal faces were evidently different following the self assembly of particles towards prismatic aggregates, with an increase in the calcination temperature. The driving force for the self assembly originated from the solid state diffusion and migration of grain boundaries in the ZnO. In addition, the ZnO single crystal with nonpolar $\{10\bar{1}0\}$ or $\{11\bar{2}0\}$ facets having O-Zn alternating atomic outermost layers performed better compared with polar $\{000\bar{1}\}$ or $\{0001\}$ single crystal with O-O or Zn-Zn monotonous atomic outermost layer.[335,336] This prismatic morphology transformed to sheet-shape after coupling with VO_x, that facilitated more exposure of $\{10\bar{1}0\}$ and consequently enhanced the activity. However, rod-like and no change in morphology was observed after coupling with CeO_x and WO_x respectively, which were not beneficial to photoactivity.[337]

The conical-like ZnO showed better photocatalytic activity compared to hourglass-like ZnO, although these morphologies exhibited similar crystal facets. This was attributed to: (i) conical-like ZnO exhibit large areas of (0001) planes, because the two halves of hourglass shaped crystals is attracted through (0001) planes; (ii) the interior cavities in conical-like ZnO allows multiple reflection of UV light that facilitates an efficient use of incident light. The ZnO with $\{\bar{1}101\}$ and $\{10\bar{1}0\}$ facets showed very least activity.[128] The activity of ZnO with hexagonal plate-like particle size was > 5 fold for MB degradation compared to rod shaped particles. The surface

of c-axis aligned rods mostly consists of nonpolar facet, while the dominant surface exposed on a hexagonal plate with same diameter are the polar facets.[127]

The ZnO superstructures for Orange-II degradation showed the following order; structure-I > structure-IV > structure-III > structure-II (Fig. 28).[338] The structure-II and -III had a six symmetric side walls enclosed by $\{10\bar{1}0\}$ surfaces, while structure-IV was composed of cone-like building blocks, of which the exposed crystal faces were $\{10\bar{1}1\}$, $\{0001\}$ and $\{10\bar{1}0\}$. Because of reduced areal proportion of low active $\{10\bar{1}0\}$ facet, structure-IV exhibited better performance than the structure II and III. Interestingly, size quantized structure-I had a main exposed plane $\{2\bar{1}\bar{1}0\}$, which has higher surface energy than $\{10\bar{1}0\}$ surface and close to polar (0001) surface.[339] These 3D superstructures were tailored by varying the concentration of zinc acetate and Na_2O_2 along with the reaction temperature without an organic additive. Under the reaction conditions (0.03 M zinc acetate and 0.1 M Na_2O_2 at pH 12.9), the adsorption of acetate anion and $Zn(OH)_3^-$ in the solution compete with $Zn(OH)_4^{2-}$ for the occupation of (0001) plane. Thus, the surplus nongrowth unit anions stabilized the surface charge and the structure of (0001) surfaces to some extent, allowing a fast growth along $<10\bar{1}0>$. Hence, ZnO crystals grew along <0001> and $<10\bar{1}0>$ directions (both are fast growth directions), resulting in ZnO NS with exposed $\{2\bar{1}\bar{1}0\}$ surface.

The ZnO nanodisks with $\{0001\}$ facet showed a high activity for dye degradation compared to the ZNWs with $\{01\bar{1}0\}$ planes.[340,341] Although, NWs surpassed in activity over nanodisk in the initial 4 h of illumination, the final degradation after 5 h was slower than nanodisks, which may be related to the formation of some long lived by products covered on the surface of NW that are resistant to react with hydroxyl radicals.[340] The heterostructure of ZnO-

disks with CdS improved the hydrogen evolution rate under the visible light by a factor of 2.8 times higher than the nonpolar ZnO-CdS.[342] It was concluded that the metallic features of polar surfaces promote the easy charge transfer at the interface between ZnO and CdS, while nonpolar $(01\bar{1}0)$ surfaces remains semiconducting in nature. In addition, the XPS VB spectra revealed that the VBM of the disk is lower than that of the rods, which reflects a strong oxidative power of photogenerated holes on the disks. Surprisingly, there was only a marginal difference in the hydrogen evolution rates between ZnO rod and disk samples. This result was against the hypothesis that the polar surfaces significantly promote the photodecomposition of organic pollutants.[127,340] This contradictory was due to: (i) polar function of the disk is restrained as they adsorb ions in the solution (Na^+, S^{2-} or SO_3^{2-}); (ii) ZnO itself is not a good candidate for hydrogen evolution as the bottom of its CB being little higher than H^+/H_2 potential.[343] The Z-scheme transfer of photogenerated charge carriers between ZnO and CdS mediated by Au NPs at the interface resulted in a significant hydrogen evolution (Fig. 29).[344] Both Au and CdS were selectively deposited on the oxygen-terminated $\{000\bar{1}\}$ surface, which is based on the rationale that the Au^{3+} and Cd^{2+} based complexes are electrostatically adsorbed on negatively charged surface. Thus, the CdS serves as a reductive site for the hydrogen evolution, while ZnO serves as an oxidative site. In Z-scheme, the recombination of photoexcited electrons from ZnO CB and holes from CdS VB occurs at the interface, and that photoexcited electrons and holes with high CB and VB potential respectively, can be retained for redox reactions. Huang *et al.*[345] suggested that Bi_2WO_6 crystal seeds can be used to tune the polar facets of ZnO and hence the photocatalytic activity. The ZnO morphology gradually changed from NRs to NS after the addition of Bi_2WO_6, due to the electrostatic interaction between these two semiconductors, consequently changing the ratio of polar facets. Compared with previous reports that used

organic additives extensively to tune the polar factets, this method has outlined the heterogeneous nucleation of ZnO on Bi_2WO_6 with specific crystal planes having minimal lattice mismatch (2.5%). The $(10\bar{1}0)$ planes of ZnO stack parallel to (200) planes of Bi_2WO_6, forming the heterojuction implying that ZnO NS grow epitaxially along the normal direction of (200) plane. In addition, the polar surfaces of ZnO was also found to be catalytically active for *N*-formylation of aninline and thermal decomposition of ammonium perchlorate.[346,347]

The internal electric field between the polar faces of Zn-$\{0001\}$ and $O-\{000\bar{1}\}$ arising from the spontaneous polarization drives the electrons and holes to migrate towards positive and negative polar planes, facilitating the reduction and oxidation to operate at different sites respectively.[348] Theoretically, strong preference of zinc ions for tetrahedral coordination geometry and coordinatively unsaturated environment of zinc ions on (0001) plane facilitates more H_2O_2 generation, adsorbs atmospheric oxygen through chemical or physical adsorption and hydroxyl anion (electrostatic attraction) to a larger extent on its surface. The Zn-$\{0001\}$ facet holds the highest chemisorptions ability and surface energy that enrich the dye adsorption on the surface and inherently more reactive than $O-\{000\bar{1}\}$ or nonpolar $\{10\bar{1}0\}$ plane.[107,331,340,349]

There is an urgent need to optimize the design and synthetic route to obtain the ZnO nanocrystallite with well defined facets. If the particle size with specific exposed crystal facets is tailored, the carrier separation efficiency can be maximized by considering the interdependence between surface structure and diffusion length of the charge carriers. The major drawback of particle aggregation during the photocatalytic reactions leads to a low dispersion and masks the exposed active facets.

10.0 Conclusion and future prospects

A significant challenge in the research of solar energy conversion and photocatalysis is the rational design of materials that can efficiently trap solar energy and to facilitate the active involvement of photogenerated charge carriers in redox reactions. Intense research efforts have led to a significant progress and as a result ZnO has emerged as a robust nanomaterial for the complete mineralization of organic pollutants under the light illumination. However, a fast recombination of photogenerated excitons, zero resistance to photoinduced corrosion and dissolution at an extreme pH values, aggregation of particles because of structural instability, and the large bandgap that remains inert for the visible light response remains as a barrier for its extended applicability.

In this context, this review aims to recognize the impressive strategies and modifications developed to overcome aforementioned drawbacks (Fig. 30), besides discussing on the mechanism of charge transfer, preparative methods, growth and their relative effects on the degradation reactions. Irrespective of the modifications, efficient interactions of charge carriers and free radicals with the pollutants ultimately determines the photocatalytic efficiency. It is clearly demonstrated that the photocatalytic activity is a complex function of several interdependent parameters and each modification has its own merits and demerits. Although, the modified ZnO has performed well against commercial ZnO or Degussa P25, the existing gap among the issues such as multifunctional property, photocatalytic performance, problems associated with their durability and the reaction selectivity for ZnO systems still needs to be bridged. The photoactivity of ZnO with biphasic crystal structure is largely unexplored in photocatalysis till date. The studies are still needed to be resolved the aforementioned drawbacks

in a single approach, and this could boost the application of ZnO based nanomaterials in many areas.

ACKNOWLEDGEMENTS Dr. S. Girish Kumar acknowledges financial support from Dr. Daulat Singh Kothari Post Doctoral Fellowship (University Grants Commission, New Delhi, INDIA) and the Department of Physics, IISc, Bangalore for providing the research facilities.

REFERENCES

(1) (a) L. G. Devi, S. G. Kumar, K. M. Reddy and C. Munikrishnappa, *J. Hazard. Mater.,* 2009, **164**, 459-467; (b) L. G. Devi, K. E. Rajashekhar, K. S. A. Raju and S. G. Kumar, *J. Mol. Catal. A: Chem.,* 2009, **314**, 88-94; (c) L. G. Devi, S. G. Kumar and K. M. Reddy, *Cent. Eur. J. Chem.,* 2009, **7**, 468-477; (d) A. S. Giri and A. K. Golder, *RSC Adv.,* 2014, **4**, 6738-6745.

(2) (a) P. V. Nidheesh, R. Gandhimathi, S. Velmathi and N. S. Sanjini, *RSC Adv.,* 2014, **4**, 5698-5708; (b) T. Han, L. Qu, Z. Luo, X. Wu and D. Zhang, *New J. Chem.,* 2014, **38**, 942-948; (c) L. G. Devi, K. S. A. Raju and S. G. Kumar, *J. Environ. Monit.,* 2009, **11**, 1397-1404; (d) I. Muthuvel and M. Swaminathan, *Catal. Commun.,* 2007, **8**, 981-986.

(3) (a) L. G. Devi, S. G. Kumar, K. S. A. Raju and K. E. Rajashekhar, *Chem. Pap.,* 2010, **64**, 378-385; (b) K. R. Naqvi, J. Marsh and V. Chechik, *Dalton Trans.,* 2014, **43**, 4745-4751; (c) L. Zhou, H. Zhang, L. Ji, Y. Shao and Y. Li, *RSC Adv.,* 2014, **4**, 24900-24908; (d) A. C. Pradhan, B. Nanda, K. M. Parida and M. Das, *Dalton Trans.,* 2013, **42**, 558-566.

(4) (a) Z. Huang, P. Wu, H. Li, W. Li, Y. Zhu and N. Zhu, *RSC Adv.,* 2014, **4**, 6500-6507; (b) J. M. Sanchez, L. H. Reyes, J. L. G. Mar, J. M. P. Hernandez and A. H. Ramirez, *Photochem. Photobiol. Sci.,* 2011, **10**, 332-337; (c) P. V. Nidheesh and R. Gandhimathi, *Desalination,* 2012, **299**, 1-15; (d) A. M. de Freitas, C. Sirtori, C. A. Lenz and P. G. P. Zamora, *Photochem. Photobiol. Sci.,* 2013, **12**, 696-702.

(5) R. Vinu and G. Madras, *J. Indian Inst. Sci.,* 2010, **90**, 189-230.

(6) (a) M. Wang, J. Ioccozia, L. Sun, C. Lin and Z. Lin, *Energy Environ. Sci.,* 2014, **7**, 2182-2202; (b) G. Zhang, G. Kim and W. Choi, *Energy Environ. Sci.,* 2014, **7**, 954-966; (c) K. Huo, B. Gao, J. Fu, L. Zhao and P. K. Chu, *RSC Adv.,* 2014, **4**, 17300-17324; (d) J. B. Joo, M. Dahl, N. Li, F. Zaera and Y. Yin, *Energy Environ. Sci.,* 2013, **6**, 2082-2092.

(7) (a) S. G. Kumar and L. G. Devi, *J. Phys. Chem. A,* 2011, **115**, 13211-13241; (b) L. G. Devi and S. G. Kumar, *Cent. Eur. J. Chem.,* 2011, **9**, 959-961; (c) K. Bourikas, C. Kordulis and A. Lycourghiotis, *Chem. Rev.,* 2014, **114**, 9754-9823; (d) L. Sang, Y. Zhao and C. Burda, *Chem. Rev.,* 2014, **114**, 9283-9318.

(8) (a) K. Lv, B. Cheng, J. Yu and G. Liu, *Phys. Chem. Chem. Phys.,* 2012, **14**, 5349-5362; (b) C. Aprile, A. Corma and H. Garcia, *Phys. Chem. Chem. Phys.,* 2008, **10**, 769-783; (c) G. Liu, L. Wang, H. G. Yang, H. M. Cheng and G. Q. Lu, *J. Mater. Chem.,* 2010, **20**, 831-843.

(9) (a) H. Zheng, J. Z. Ou, M. S. Strano, R. B. Kaner, A. Mitchell and K. K. Zadeh, *Adv. Funct. Mater.,* 2011, **21**, 2175-2196; (b) C. Janaky, K. Rajeshwar, N. R. de Tacconi, W. Chanmanee and M. N. Huda, *Catal. Today,* 2013, **199**, 53-64.

(10) (a) L. Zhu, B. Wei, L. Xu, Z. Lu, H. Zhang, H. Gao and J. Che, *CrystEngComm,* 2012, **14**, 5705-5709; (b) D. P. Dutta, M. Roy and A. K. Tyagi, *Dalton Trans.,* 2012, **41**, 10238-10248; (c) S. Balachandran and M. Swaminathan, *J. Phys. Chem. C,* 2012, **116**, 26306-26312.

(11) (a) T. K. Townsend, E. M. Sabio, N. D. Browning and F. E. Osterloh, *Energy Environ. Sci.,* 2011, **4**, 4270-4275; (b) D. K. Bora, A. Braun and E. C. Constable, *Energy Environ Sci.,* 2013, **6**, 407-425; (c) J. Sun, K. L. Wu, X. Z. Li, C. Dong, X. W. Wei, X. W. Wang, B. Zhang, Z. X. Zhang and J. R. Huang, *CrystEngComm,* 2014, **16**, 6873-6881; (d) K. Sivula, F. L. Formal and M. Gratzel, *ChemSusChem.,* 2011, **4**, 432-449.

(12) (a) K. Pirkanniemi and M. Sillanpaa, *Chemosphere,* 2002, **48**, 1047-1060; (b) H. Zhang, G. Chen and D. W. Bahnemann, *J. Mater. Chem.,* 2009, **19**, 5089-5121.

(13) (a) L. Ye, Y. Su, X. Jin, H. Xie and C. Zhang, *Environ. Sci.:Nano,* 2014, **1**, 90-112; (b) J. Li, Y. Yu and L. Zhang, *Nanoscale,* 2014, **6**, 8473-8488; (c) H. Cheng, B. Huang and Y. Dai, *Nanoscale,* 2014, **6**, 2009-2026.

(14) (a) F. Dong, Q. Li, Y. Zhou, Y. Sun, H. Zhang and Z. Wu, *Dalton Trans.,* 2014, **43**, 9468-9480; (b) F. Dong, Y. Sun, W. K. Ho and Z. Wu, *Dalton Trans.,* 2012, **41**, 8270-8284; (c) F. Dong, A. Zheng, Y. Sun, M. Fu, B. Jiang, W. K. Ho, S. C. Lee and Z. Wu, *CrystEngComm,* 2012, **14**, 3534-3544.

(15) (a) D. Zhang and F. Zeng, *Res. Chem. Intermed.,* 2010, **36**, 1055-1063; (b) D. Zhang, *Transition Met. Chem.,* 2010, **35**, 689-694; (c) D. Zhang and F. Zeng, *J. Mater. Sci.,* 2012, **47**, 2155-2161; (d) D. Zhang, *Russ. J. Phys. Chem. A,* 2013, **87**, 137-144.

(16) P. V. Kamat, R. Huehn and R. Nicolaescu, *J. Phys. Chem. B,* 2002, **106**, 788-794.

(17) (a) D. C. Look, D. C. Reynolds, J. R. Sizelove, R. L. Jones, C. W. Litton, G. Cantwell and W. C. Harsch, *Solid State Commun.,* 1998, **105**, 399-401; (b) A. K. Chandiran, M. A. Jalebi, M. K. Nazeeruddin and M. Gratzel, *ACS Nano,* 2014, **8**, 2261-2268.

(18) (a) M. Quintana, T. Edvinsson, A. Hagfeldt and G. Boschloo, *J. Phys. Chem. C,* 2007, **111**, 1035-1041; (b) J. A. Anta, E. Guillen and R. T. Zaera, *J. Phys. Chem. C,* 2012, **116**, 11413-11425; (c) S. Cho, J. W. Jang, S. H. Lim, H. J. Kang, S. W. Rhee, J. S. Lee and K. H. Lee, *J. Mater. Chem.,* 2011, **21**, 17816-17822.

(19) (a) G. Marci, V. Augugliaro, M. J. L. Munoz, C. Martin, L. Palmisano, V. Rives, M. Schiavello, R. J. D. Tilley and A. M. Venezia, *J. Phys. Chem. B,* 2001, **105**, 1033-1040; (b) P. V. Kamat, I. Bedja and S. Hotchandanit, *J. Phys. Chem.,* 1994, **98**, 9137-9142.

(20) N. Daneshvar, D. Salari and A. R. Khataee, *J. Photochem. Photobiol. A: Chem.,* 2004, **162**, 317-322.

(21) (a) A. A. Khodja, T. Sehili, J. F. Pilichowski and P. Boule, *J. Photochem. Photobiol. A: Chem.,* 2001, **141**, 231-239; (b) C. Tian, Q. Zhang, A. Wu, M. Jiang, Z. Liang, B. Jiang and H. Fu, *Chem. Commun.,* 2012, 2858-2860.

(22) (a) J. P. Percherancier, R. Chapelon and B. Pouyet, *J. Photochem. Photobiol. A: Chem.,* 1995, **87**, 261-266; (b) C. Hariharan, *Appl. Catal. A: Gen.,* 2006, **304**, 55-61.

(23) (a) I. Poulios, M. Kositzi and A. Kouras, *J. Photochem. Photobiol. A: Chem.,* 1998, **115**, 175-183; (b) A. Akyol, H. C. Yatmaz and M. Bayramoglu, *Appl. Catal. B: Environ.,* 2004, **54**, 19-24.

(24) (a) P. R. Shukla, S. Wang, H. M. Ang and M. O. Tade, *Sep. Purif. Technol.,* 2010, **70**, 338-344; (b) G. Colon, M. C. Hidalgo, J. A. Navio, E. P. Melian, O. G. Diaz and J. M. D. Rodriguez, *Appl. Catal. B: Environ.,* 2008, **83**, 30-38.

(25) (a) C. Lizama, J. Freer, J. Baeza and H. D. Mansilla, *Catal. Today,* 2002, **76**, 235-246; (b) J. Fenoll, P. Sabater, G. Navarro, G. P. Lucas and S. Navarro, *J. Hazard. Mater.,* 2013, **244-245**, 370-379.

(26) (a) V. Kandavelu, H. Kastien and K. R. Thampi, *Appl. Catal. B: Environ.,* 2004, **48**, 101-111; (b) Y. Liao, C. Xie, Y. Liu and Q. Huang, *J. Alloys Compd.,* 2013, **550**, 190-197.

(27) J. Liqiang, W. Dejun, W. Baiqi, L. Shudan, X. Baifu, F. Honggang and S. Jiazhong, *J. Mol. Catal. A: Chem.,* 2006, **244**, 193-200.

(28) (a) S. S. Warule, N. S. Chaudhari, B. B. Kale and M. A. More, *CrystEngComm,* 2009, **11**, 2776-2783; (b) E. Evgenidou, K. Fytianos and I. Poulios, *Appl. Catal. B: Environ.,* 2005, **59**, 81-89.

(29) (a) S. Baruah, S. S. Sinha, B. Ghosh, S. K. Pal, A. K. Raychaudhuri and J. Dutta, *J. Appl. Phys.,* 2009, **105**, 074308; (b) Y. Lv, C. Pan, X. Ma, R. Zong, X. Bai and Y. Zhu, *Appl. Catal. B: Environ.,* 2013, **138-139**, 26-32.

(30) (a) D. Chen, Z. Wang, T. Ren, H. Ding, W. Yao, R. Zong and Y. Zhu, *J. Phys. Chem. C,* 2014, **118**, 15300-15307; (b) Z. Pei, L. Ding, J. Hu, S. Weng, Z. Zheng, M. Huang and P. Liu, *Appl. Catal. B: Environ.,* 2013, **142-143**, 736-743.

(31) (a) F. Kayaci, S. Vempati, I. Donmez, N. Biyikli and T. Uyar, *Nanoscale,* 2014, **6**, 10224-10234; (b) Y. Lv, W. Yao, X. Ma, C. Pan, R. Zong and Y. Zhu, *Catal. Sci. Technol.,* 2013, **3**, 3136-3146; (c) Y. Zheng, C. Chen, Y. Zhan, X. Lin, Q. Zheng, K. Wei, J. Zhu and Y. Zhu, *Inorg. Chem.,* 2007, **46**, 6675-6682.

(32) (a) H. W. Jeong, S. Y. Choi, S. H. Hong, S. K. Lim, D. S. Han, A. A. Wahab and H. Park, *J. Phys. Chem. C,* 2014, **118**, 21331-21338; (b) X. Xu, X. Duan, Z. Yi, Z. Zhou, X. Fan and Y. Wang, *Catal. Commun.,* 2010, **12**, 169-172; (c) M. Y. Guo, A. M. C. Ng, F. Liu, A. B. Djurisic and W. K. Chan, *Appl. Catal. B: Environ.,* 2011, **107**, 150-157.

(33) (a) J. Han, Y. Liu, N. Singhal, L. Wang and W. Gao, *Chem. Eng. J,* 2012, **213**, 150-162; (b) Y. Peng, Y. Wang, Q. G. Chen, Q. Zhu and A. W. Xu, *CrystEngComm,* 2014, **16**, 7906-7913.

(34) (a) S. C. Pillai, J. M. Kelly, R. Ramesh and D. E. McCormack, *J. Mater. Chem. C,* 2013, **1**, 3268-3281; (b) J. Li, Q. Sun, C. Jin and J. Li, *Ceram. Int.,* 2014, DOI: 10.1016/j.ceramint.2014.09.010

(35) A. B. Djurisic, A. M. C. Ng, X. Y. Chen, *Prog. Quant. Electron.,* 2010, **34**, 191-259.

(36) Y. Tu, L. Zhou, Y. Z. Jin, C. Gao, Z. Z. Ye, Y. F. Yang and Q. L. Wang, *J. Mater. Chem.,* 2010, **20**, 1594-1599.

(37) (a) Z. L. Wang and J. Song, *Science,* 2006, **312**, 242-246; (b) L. S. Mende and J. L. M. Driscoll, *Mater. Today,* 2007, **10**(5), 40-48.

(38) (a) A. E. Lavat, C. C. Wagner and J. E. Tasca, *Ceram. Int.,* 2008, **34**, 2147-2153; (b) K. Ghule, A. V. Ghule, B. J. Chen and Y. C. Ling, *Green Chem.,* 2006, **8**, 1034-1041.

(39) (a) G. Heiland and H. Ibach, *Solid State Commun.,* 1966, **4**, 353-356; (b) H. Liu, F. Zeng, S. Gao, G. Wang, C. Song and F. Pan, *Phys. Chem. Chem. Phys.,* 2013, **15**, 13153-13161.

(40) (a) P. Spathis and I. Poulios, *Corros. Sci.,* 1995, **37**, 673-680; (b) J. Han, W. Qiu and W. Gao, *J. Hazard. Mater.,* 2010, **178**, 115-122.

(41) A. L. Rudd and C. B. Breslin, *Electrochim. Acta,* 2000, **45**, 1571-1579.

(42) (a) A. Moezzi, A. M. McDonagh and M. B. Cortie, *Chem. Eng. J.,* 2012, **185-186**, 1-22; (b) J. C. Fan, K. M. Sreekanth, Z. Xie, S. L. Chang and K. V. Rao, *Prog. Mater. Sci.,* 2013, **58**, 874-985; (c) J. L. Gomez and O. Tigli, *J. Mater. Sci.,* 2013, **48**, 612-624.

(43) (a) A. Janotti and C. G. V. de Walle, *Rep. Prog. Phys.,* 2009, **72**, 126501; (b) Y. Kozuka, A. Tsukazaki and M. Kawasaki, *Appl. Phys. Rev.,* 2014, **1**, 011303; (c) J. J. Chen, X. R. Deng and H. Deng, *J. Mater. Sci.,* 2013, **48**, 532-542.

(44) (a) M. D. McCluskey and S. J. Jokela, *J. Appl. Phys.,* 2009, **106**, 071101; (b) B. Ludi and M. Niederberger, *Dalton Trans.,* 2013, **42**, 12554-12568; (c) J. Li, S. Ma, X. Liu, Z. Zhou and C. Q. Sun, *Chem. Rev.,* 2012, **112**, 2833-2852.

(45) (a) X. Wang, J. Song and Z. L. Wang, *J. Mater. Chem.,* 2007, **17**, 711-720; (b) C. Klingshirn, J. Fallert, H. Zhou, J. Sartor, C. Thiele, F. M. Fliag, D. Schneider and H. Kalt, *Phys. Status Solidi B,* 2010, **247**, 1424-1447.

(46) (a) U. Ozgur, Y. I. Alivov, C. Liu, A. Teke, A. Reshchikov, S. Dogan, V. Avrutin, S. J. Cho and H. Morkoc, *J. Appl. Phys.,* 2005, **98**, 041301; (b) B. Weintraub, Z. Zhou, Y. Li and Y. Deng, *Nanoscale,* 2010, **2**, 1573-1587.

(47) (a) A. B. Djurisic, X. Chen, Y. H. Leung and A. M. C. Ng, *J. Mater. Chem.,* 2012, **22**, 6526-6535; (b) S. Dutta, S. Chattopadhyay, A. Sarkar, M. Chakrabarti, D. Sanyal and D. Jana, *Prog. Mater. Sci.,* 2009, **54**, 89-136.

(48) (a) A. D. Paola, E. G. Lopez, G. Marci and L. Palmisano, *J. Hazard. Mater.,* 2012, **211-212**, 3-29; (b) I. Udom, M. K. Ram, E. K. Stefanakos, A. F. Hepp and D. Y. Goswami, *Mater. Sci. Semicond. Process.,* 2013, **16**, 2070-2083; (c) Y. Zhang, M. K. Ram, E. K. Stefanakos and D. Y. Goswami, *J. Nanomater.,* 2012, 624520.

(49) (a) S. M. Lam, J. C. Sin, A. Z. Abdullah and A. R. Mohamed, *Desalin. Water Treat.,* 2012, **41**, 131-169; (b) S. H. S. Chan, T. Y. Wu, J. C. Juan and C. Y. Teh, *J. Chem. Technol. Biotechnol.,* 2011, **86**, 1130-1158; (c) R. Kumar, G. Kumar and A. Umar, *Nanosci. Nanotechnol. Lett.,* 2014, **6**, 631-650.

(50) (a) M. D. H. Alonso, F. Fresno, S. Suarez and J. M. Coronado, *Energy Environ. Sci.,* 2009, **2**, 1231-1257; (b) M. Montazer and M. M. Amiri, *J. Phys. Chem. B,* 2014, **118**, 1453-1470.

(51) (a) S. Rehman, R. Ullah, A. M. Butt and N. D. Gohar, *J. Hazard. Mater.,* 2009, **170**, 560-569; (b) A. K. Radzimska and T. Jesionowski, *Materials,* 2014, **7**, 2833-2881.

(52) (a) M. R. Hoffmann, S. T. Martin, W. Choi and D. W. Bahnemann, *Chem. Rev.,* 1995, **95**, 69-96; (b) A. Ajmal, I. Majeed, R. N. Malik, H. Idriss and M. A. Nadeem, *RSC Adv.,* 2014, **4**, 37003-37026.

(53) (a) J. Schneider, M. Matsuoka, M. Takeuchi, J. Zhang, Y. Horiuchi, M. Anpo and D. Bahnemann, *Chem. Rev.,* 2014, **114**, 9919-9986; (b) D. Friedmann, C. Mendive and D. Bahnemann, *Appl. Catal. B: Environ.,* 2010, **99**, 398-406.

(54) Y. Li, W. Xie, X. Hu, G. Shen, X. Zhou, Y. Xiang, X. Zhao and P. Fang, *Langmuir,* 2010, **26**, 591-597.

(55) (a) Z. Li, Y. Fang, X. Zhan and S. Xu, *J. Alloys Compd.,* 2013, **564**, 138-142; (b) D. Chatterjee and S. Dasgupta, *J. Photochem. Photobiol. C: Photochem. Rev.,* 2005, **6**, 186-205.

(56) (a) R. Vinu, S. Polisetti and G. Madras, *Chem. Eng. J,* 2010, **165**, 784-797; (b) Y. C. Hsiao, T. F. Wu, Y. S. Wang, C. C. Hu and C. Huang, *Appl. Catal. B: Environ.,* 2014, **148-149**, 250-257.

(57) X. Li, Y. Cheng, S. Kang and J. Mu, *Appl. Surf. Sci.,* 2010, **256**, 6705-6709.

(58) Y. Li, X. Zhou, X. Hu, X. Zhao and P. Fang, *J. Phys. Chem. C,* 2009, **113**, 16188-16192.

(59) R. Comparelli, E. Fanizza, M. L. Curri, P. D. Cozzoli, G. Mascolo and A. Agostiano, *Appl. Catal. B: Environ.,* 2005, **60**, 1-11.

(60) H. Wang and C. Xie, *J. Phys. Chem. Solids,* 2008, **69**, 2440-2444.

(61) D. S. Bohle and C. J. Spina, *J. Am. Chem. Soc.,* 2009, **131**, 4397-4404.

(62) J. Becker, K. R. Raghupathi, J. St. Pierre, D. Zhao and R. T. Koodali, *J. Phys. Chem. C,* 2011, **115**, 13844-13850.

(63) H. Wang, C. Xie, W. Zhang, S. Cai, Z. Yang and Y. Gui, *J. Hazard. Mater.,* 2007, **141**, 645-652.

(64) A. C. Dodd, A. J. McKinley, M. Saunders and T. Tsuzuki, *J. Nanopart. Res.,* 2006, **8**, 43-51.

(65) (a) L. G. Devi and S. G. Kumar, *Appl. Surf. Sci.,* 2012, **261**, 137-146; (b) L. G. Devi and S. G. Kumar, *Appl. Surf. Sci.,* 2011, **257**, 2779-2790; (c) L. G. Devi, N. Kottam and S. G. Kumar, *J. Phys. Chem. C,* 2009, **113**, 15593-15601; (d) L. G. Devi, N. Kottam, B. N. Murthy and S. G. Kumar, *J. Mol. Catal. A: Chem.,* 2010, **328**, 44-52.

(66) P. S. Casey, C. J. Rossouw, S. Boskovic, K. A. Lawrence and T. W. Turney, *Superlatt. Microstruct.,* 2006, **39**, 97-106.

(67) T. R. Giraldi, G. V. F. Santos, V. R. de Mendonca, C. Ribeiro and I. T. Weber, *Mater. Chem. Phys.,* 2012, **136**, 505-511.

(68) S. Sakthivel, B. Neppolian, M. V. Shankar, B. Arabindoo, M. Palanichamy and V. Murugesan, *Solar Energy Mater. Sol. Cells,* 2003, **77**, 65-82.

(69) Y. Huang, Y. Wei, J. Wu, C. Guo, M. Wang, S. Yin and T. Sato, *Appl. Catal. B: Environ.,* 2012, **123-124**, 9-17.

(70) S. K. Pardeshi and A. B. Patil, *Sol. Energy,* 2008, **82**, 700-705.

(71) (a) D. W. Bahnemann, C. K. Kormann and M. R. Hoffmann, *J. Phys. Chem.,* 1987, **91**, 3789-3798; (b) G. A. Parks, *Chem. Rev.,* 1995, **65**, 177-198; (c) H. Yin and P. S. Casey, *RSC Adv.,* 2014, **4**, 26149-26157.

(72) A. N. Rao, B. Sivasankar and V. Sadasivam, *J. Hazard. Mater.,* 2009, **166**, 1357-1361.

(73) E. Evgenidou, I. Konstantinou, K. Fytianos, I. Poulios and T. Albanis, *Catal. Today,* 2007, **124**, 156-162.

(74) (a) L. G. Devi, K. S. A. Raju, S. G. Kumar and K. E. Rajashekhar, *J. Taiwan Inst. Chem. Eng.,* 2011, **42**, 341-349; (b) X. Wang, L. Wang, J. Li, J. Qiu, C. Cai and H. Zhang, *Sep. Purif. Technol.,* 2014, **122**, 41-46; (c) N. Sobana and M. Swaminathan, *Sep. Purif. Technol.,* 2007, **56**, 101-107.

(75) G. K. Prasad, P. V. R. K. Ramacharyulu, B. Singh, K. Batra, A. R. Srivastava, K. Ganesan and R. Vijayaraghavan, *J. Mol. Catal. A: Chem.,* 2011, **349**, 55-62.

(76) C. Lu, Y. Wu, F. Mai, W. Chung, C. Wu, W. Lin and C. Chen, *J. Mol. Catal. A: Chem.,* 2009, **310**, 159-165.

(77) C. Chen, *J. Mol. Catal. A: Chem.,* 2007, **264**, 82-92.

(78) D. Mijin, M. Savic, P. Snezana, A. Smiljanic, O. Glavaski, M. Jovanovic and S. Petrovic, *Desalination,* 2009, **249**, 286-292.

(79) C. Karunakaran, S. Senthilvelan, S. Karuthapandain and K. Balaraman, *Catal. Commun.,* 2004, **5**, 283-290.

(80) M. Iranifam, M. Zarei and A. R. Khataee, *J. Electroanal. Chem.,* 2011, **659**, 107-112.

(81) J. Wang, P. Liu, X. Fu, Z. Li, W. Han and X. Wang, *Langmuir,* 2009, **25**, 1218-1223.

(82) J. Wang, P. Liu, S. Wang, W. Han, X. Wang and X. Fu, *J. Mol. Catal. A: Chem.,* 2007, **273**, 21-25.

(83) P. Liu, J. Bandara, Y. Lin, D. Elgin, L. F. Allard and Y. P. Sun, *Langmuir,* 2002, **18**, 10398-10401.

(84) S. Wang, P. Liu, X. Wang and X. Fu, *Langmuir,* 2005, **21**, 11969-11973.

(85) P. Pathak, M. J. Meziani, Y. Li, L. T. Cureton and Y. P. Sun, *Chem. Commun.,* 2004, 1234-1235.

(86) H. Zhang, R. Zong and Y. Zhu, *J. Phys. Chem. C,* 2009, **113**, 4605-4611.

(87) Z. Pei, L. Ding, M. Lu, Z. Fan, S. Weng, J. Hu and P. Liu, *J. Phys. Chem. C,* 2014, **118**, 9570-9577.

(88) J. Wang, Z. Wang, B. Huang, Y. Ma, Y. Liu, X. Qin, X. Zhang and Y. Dai, *ACS Appl. Mater. Interfaces,* 2012, **4**, 4024-4030.

(89) R. W. Matthews and S. R. McEvoy, *J. Photochem. Photobiol. A: Chem.,* 1992, **66**, 355-366.

(90) A. M. Ali, E. A. C. Emanuelsson and D. A. Patterson, *Appl. Catal. B: Environ.,* 2011, **106**, 323-336.

(91) R. A. Reichle, K. G. McCurdy and L. G. Hepler, *Can. J. Chem.,* 1975, **53**, 3841-3845.

(92) A. Moezzi, M. Cortie and A. McDonagh, *Dalton Trans.,* 2011, **40**, 4871-4878.

(93) (a) S. Yamabi and H. Imai, *J. Mater. Chem.,* 2002, **12**, 3773-3778; (b) A. Moezzi, M. B. Cortie and A. M. McDonagh, *Dalton Trans.,* 2013, **42**, 14432-14437; (c) W. J. Li, E. W. Shi, W. Z. Zhong and Z. W. Yin, *J. Cryst. Growth,* 1999, **203**, 186-196.

(94) S. G. Kumar and K. S. R. K. Rao, *Nanoscale,* 2014, **6**, 11574-11632.

(95) N. C. S. Selvam, J. J. Vijaya and L. J. Kennedy, *Ind. Eng. Chem. Res.,* 2012, **51**, 16333-16345.

(96) (a) J. H. Qian, L. W. Zhu and R. Guo, *J. Chin. Chem. Soc.,* 2005, **52**, 1245-1252; (b) N. C. S. Selvam, J. J. Vijaya and L. J. Kennedy, *J. Colloid Interface Sci.,* 2013, **407**, 215-224.

(97) J. Y. Dong, Y. J. Hsu, D. S. H. Wong and S. Y. Lu, *J. Phys. Chem. C*, 2010, **114**, 8867-8872.

(98) K. J. M. Bishop, C. E. Wilmer, S. Soh and B. A. Grzybowski, *Small*, 2009, **5**, 1600-1630.

(99) S. S. Shinde, P. S. Shinde, C. H. Bhosale and K. Y. Rajpure, *J. Photochem. Photobiol. B: Biol.,* 2011, **104**, 425-433.

(100) P. R. Potti and V. C. Srivastava, *Ind. Eng. Chem. Res.,* 2012, **51**, 7948-7956.

(101) C. C. Hwang and T. Y. Wu, *Mater. Sci. Eng. B,* 2004, **111**, 197-206.

(102) K. M. Fang, Z. Z. Wang, M. Zhang, A. J. Wang, Z. Y. Meng and J. J. Feng, *J. Colloid Interface. Sci.,* 2013, **402**, 68-74.

(103) H. Liu, J. Yang, J. Liang, Y. Huang and C. Tang, *J. Am. Ceram. Soc.,* 2008, **91**, 1287-1291.

(104) M. Y. Guo, A. M. C. Ng, F. Liu, A. B. Djurisic, W. K. Chan, H. Su and K. S. Wong, *J. Phys. Chem. C,* 2011, **115**, 11095-11101.

(105) Q. Wan, T. H. Wang and J. C. Zhao, *Appl. Phys. Lett.,* 2005, **87**, 083105.

(106) Y. Wang, X. Li, G. Lu, X. Quan and G. Chen, *J. Phys. Chem. C,* 2008, **112**, 7332-7336.

(107) E. S. Jang, J. H. Won, S. J. Hwang and J. H. Choy, *Adv. Mater.,* 2006, **18**, 3309-3312.

(108) (a) X. Zou, H. Fan, Y. Tian and S. Yan, *CrystEngComm,* 2014, **16**, 1149-1156; (b) P. D. Cozzoli, A. Kornowski and H. Weller, *J. Am. Chem. Soc.,* 2003, **125**, 14539-14548.

(109) Y. Liu, J. Shi, Q. Peng and Y. Li, *J. Mater. Chem.,* 2012, **22**, 6539-6541.

(110) B. Liu, J. Xu, S. Ran, Z. Wang, D. Chen and G. Shen, *CrystEngComm,* 2012, **14,** 4582-4588.

(111) Z. Peng, Y. Jiang, Y. Song, C. Wang and H. Zhang, *Chem. Mater.,* 2008, **20**, 3153-3162.

(112) (a) A. Subramania, G. V. Kumar, A. R. S. Priya and T. Vasudevan, *Nanotechnology,* 2007, **18**, 225601; (b) L. H. Zhao and S. Q. Sun, *CrystEngComm,* 2011, **13**, 1864-1869.

(113) J. Yu and X. Yu, *Environ. Sci. Technol.,* 2008, **42**, 4902-4907.

(114) (a) H. Yu, J. Yu, S. Liu and S. Mann, *Chem. Mater.,* 2007, **19**, 4327-4334; (b) C. Zhu, B. Lu, Q. Su, E. Xie and W. Lan, *Nanoscale,* 2012, **4**, 3060-3064. (c) J. Yu and J. Zhang, *Dalton Trans.,* 2010, **39**, 5860-5867; (d) H. Li, Z. Bian, J. Zhu, D. Zhang, G. Li, Y. Huo, H. Li and Y. Lu, *J. Am. Chem. Soc.,* 2007, **129**, 8406-8407.

(115) E. Yassitepe, H. C. Yatmaz, C. Ozturk, K. Ozturk and C. Duran, *J. Photochem. Photobiol. A: Chem.,* 2008, **198**, 1-6.

(116) (a) A. V. Dijken, A. H. Janssen, M. H. P. Smitsmans, D. Vanmaekelbergh and A. Meijerink, *Chem. Mater.,* 1998, **10**, 3513-3522; (b) R. I. Bickley and F. S. Stone, *J. Catal.,* 1973, **31**, 389-397.

(117) Q. Xie, J. Li, Q. Tian and R. Shi, *J. Mater Chem.,* 2012, **22**, 13541-13547.

(118) (a) H. C. Zeng, *Curr. Nanosci.,* 2007, **3**, 177-181; (b) X. Chen, X. Jing, J. Wang, J. Liu, D. Song and L. Liu, *CrystEngComm,* 2013, **15**, 7243-7249; (c) W. Ostwald, *Z. Phys. Chem.,* 1897, **22**, 289-330; (d) W. Ostwald, *Z. Phys. Chem.,* 1900, **34**, 495-503.

(119) F. Lu, W. Cai and Y. Zhang, *Adv. Funct. Mater.,* 2008, **18**, 1047-1056.

(120) C. Ye, Y. Bando, G. Shen and D. Golberg, *J. Phys. Chem. B,* 2006, **110**, 15146-15151.

(121) J. Gupta, K. C. Barick and D. Bahadur, *J. Alloys Compd.,* 2011, **509**, 6725-6730.

(122) I. Altln, I. Polat, E. Bacakslz and M. Sokmen, *Appl. Surf. Sci.,* 2012, **258**, 4861-4865.

(123) J. Xie, H. Wang, M. Duan and L. Zhang, *Appl. Surf. Sci.,* 2011, **257**, 6358-6363.

(124) D. Chen, D. Yang, Q. Wang and Z. Jiang, *Ind. Eng. Chem. Res.,* 2006, **45**, 4110-4116.

(125) H. Wang, S. Dong, Y. Chang, X. Zhou and X. Hu, *Appl. Surf. Sci.,* 2012, **258**, 4288-4293.

(126) L. Sun, R. Shao, Z. Chen, L. Tang, Y. Dai and J. Ding, *Appl. Surf. Sci.,* 2012, **258**, 5455-5461.

(127) A. Mclaren, T. V. Solis, G. Li and S. C. Tsang, *J. Am. Chem. Soc.,* 2009, **131**, 12540-12541.

(128) L. Xu, Y. L. Hu, C. Pelligra, C. H. Chen, L. Jin, H. Huang, S. Sithambaram, M. Aindow, R. Joesten and S. L. Suib, *Chem. Mater.,* 2009, **21**, 2875-2885.

(129) (a) M. Wang, Y. Zhang, Y. Zhou, F. Yang, E. J. Kim, S. H. Hahn and S. G. Seong, *CrystEngComm,* 2013, **15**, 754-763; (b) S. Das and S. Ghosh, *Dalton Trans.,* 2013, **42**, 1645-

1656; (c) S. Das, K. Dutta and A. Pramanik, *CrystEngComm,* 2013, **15**, 6349-6358; (d) M. Raula, M. Biswas and T. K. Mandal, *RSC Adv.,* 2014, **4**, 5055-5064.

(130) W. Choi, A. Termin and M. R. Hoffmann, *J. Phys. Chem.,* 1994, **98**, 13669-13679; (b) C. M. Teh and A. R. Mohamed, *J. Alloys Compd.,* 2011, **509**, 1648-1660; (c) L. G. Devi, N. Kottam, S. G. Kumar and K. S. A. Raju, *Catal. Lett.,* 2009, **131**, 612-617; (d) J. Choi, H. Park and M. R. Hoffmann, *J. Phys. Chem. C,* 2010, **114**, 783-792.

(131) H. Benhebal, M. Chaib, C. Malengreaux, S. D. Lambert, A. Leonard, M. Crine and B. Heinrichs, *J. Taiwan Inst. Chem. Eng.,* 2014, **45**, 249-253.

(132) V. Etacheri, R. Roshan and V. Kumar, *ACS Appl. Mater. Interfaces,* 2012, **4**, 2717-2725.

(133) (a) B. E. Sernelius, K. F. Berggren, Z. C. Jin, I. Hamberg and C. G. Granqvist, *Phys. Rev. B,* 1988, **37**, 10244; (b) Z. Li, W. Shen, S. Xue and X. Zu, *Colloids Surf. A: Physicochem. Eng. Aspects,* 2008, **320**, 156-160.

(134) J. Z. Kong, A. D. Li, X. Y. Li, H. F. Zhai, W. Q. Zhang, Y. P. Gong, H. Li and D. Wu, *J. Solid State Chem.,* 2010, **183**, 1359-1364.

(135) J. Z. Kong, A. D. Li, H. F. Zhai, Y. P. Gong, H. Li and D. Wu, *J. Solid State Chem.,* 2009, **182**, 2061-2067.

(136) (a) A. Janotti and C. G. V. de Walle, *Appl. Phys. Lett.,* 2005, **87**, 122102; (b) A. Janotti and C. G. V. de Walle, *J. Cryst. Growth,* 2006, **287**, 58-65.

(137) C. Wu, L. Shen, Y. C. Zhang and Q. Huang, *Mater. Lett.,* 2011, **65**, 1794-1796.

(138) C. Xu, L. Cao, G. Su, W. Liu, X. Qu and Y. Yu, *J. Alloys Compd.,* 2010, **497**, 373-376.

(139) K. Jayanthi, S. Chawla, A. G. Joshi, Z. H. Khan and R. K. Kotnala, *J. Phys. Chem. C,* 2010, **114**, 18429-18434.

(140) R. Ullah and J. Dutta, *J. Hazard. Mater.,* 2008, **156**, 194-200.

(141) F. Tuomisto, K. Sarrinen, D. C. Look and G. C. Farlow, *Phys. Rev. B,* 2005, **72**, 085206.

(142) M. A. Mahmood, S. Baruah and J. Dutta, *Mater. Chem. Phys.,* 2011, **130**, 531-535.

(143) L. X. Zhang, P. Liu and Z. X. Su, *Mater. Res. Bull.,* 2006, **41**, 1631-1637.

(144) A. Dodd, A. McKinley, T. Tsuzuki and M. Saunders, *Mater. Chem. Phys.,* 2009, **114**, 382-386.

(145) K. C. Barick, S. Singh, M. Aslam and D. Bahadur, *Microporous Mesoporous Mater.,* 2010, **134**, 195-202.

(146) B. M. Rajbongshi and S. K. Samdarshi, *Appl. Catal. B: Environ.,* 2014, **144**, 435-441.

(147) N. V. Kaneva, D. T. Dimitrov and C. D. Dushkin, *Appl. Surf. Sci.,* 2011, **257**, 8113-8120.

(148) K. Sato and H. K. Yoshida, *Semicond. Sci. Technol.,* 2002, **17**, 367-376.

(149) J. Zhao, L. Wang, X. Yan, Y. Yang, Y. Lei, J. Zhou, Y. Huang, Y. Gu and Y. Zhang, *Mater. Res. Bull.,* 2011, **46**, 1207-1210.

(150) J. B. Zhong, J. Z. Li, X. Y. He, J. Zeng, Y. Lu, W. Hu and K. Lin, *Curr. Appl. Phys.,* 2012, **12**, 998-1001.

(151) (a) L. G. Devi, N. Kottam, S. G. Kumar and K. E. Rajashekhar, *Cent. Eur. J. Chem.,* 2009, **8**, 142-148. (b) K. E. Karakitsou and X. E. Verykios, *J. Phys. Chem.,* 1993, **97**, 1184-1189; (c) A. W. Xu, Y. Gao and H. Q. Liu, *J. Catal.,* 2002, **207**, 151-157.

(152) M. Fu, Y. Li, S. Wu, P. Lu, J. Liu and F. Dong, *Appl. Surf. Sci.,* 2011, **258**, 1587-1591.

(153) H. Ma, L. Yue, C. Yu, X. Dong, X. Zhang, M. Xue, X. Zhang and Y. Fu, *J. Mater. Chem.,* 2012, **22**, 23780-23788.

(154) (a) B. Donkova, D. Dimitrov, M. Kostadinov, E. Mitkova and D. Mehandjiev, *Mater. Chem. Phys.,* 2010, **123**, 563-568; (b)Y. Kanai, *Jpn. J. Appl. Phys.,* 1991, **30**, 703-707.

(155) (a) X. Zhang, M. Zhou and L. Lei, *Carbon*, 2005, **43**, 1700-1708; (b) G. L. Puma, A. Bono, D. Krishnaiah and J. G. Collin, *J. Hazard. Mater.,* 2008, **157**, 209-219; (c) A. E. Eliyas, L. Ljutzkanov, I. D. Stambolova, V. N. Blaskov, S. V. Vassilev, E. N. R. Velkova and D. R. Mehandjiev, *Cent. Eur. J. Chem.,* 2013, **11**, 464-470.

(156) N. M. Jacob, G. Madras, N. Kottam and T. Thomas, *Ind. Eng. Chem. Res.,* 2014, **53**, 5895-5904.

(157) O. Yayapao, T. Thongtem, A. Phuruangrat and S. Thongtem, *Mater. Lett.,* 2013, **90**, 83-86.

(158) M. Khatamian, A. A. Khandar, B. Divband, M. Haghighi and S. Ebrahimiasl, *J. Mol. Catal. A: Chem.,* 2012, **365**, 120-127.

(159) S. Suwanboon, P. Amornpitoksuk, A. Sukolrat and N. Muensit, *Ceram. Int.,* 2013, **39**, 2811-2819.

(160) S. Anandan, A. Vinu, T. Mori, N. Gokulakrishnan, P. Srinivasu, V. Murugesan and K. Ariga, *Catal. Commun.,* 2007, **8**, 1377-1382.

(161) S. Anandan, A. Vinu, K. L. P. S. Lovely, N. Gokulakrishnan, P. Srinivasu, T. Mori, V. Murugesan, V. Sivamurugan and K. Ariga, *J. Mol. Catal. A: Chem.,* 2007, **266**, 149-157.

(162) M. Rezaei and A. H. Yangjeh, *Appl. Surf. Sci.,* 2013, **265**, 591-596.

(163) B. Subash, B. Krishnakumar, R. Velmurugan, M. Swaminathan and M. Shanthi, *Catal. Sci. Technol.,* 2012, **2**, 2319-2326.

(164) (a) M. V. Dozzi and E. Selli, *J. Photochem. Photobiol. C: Photochem. Rev.,* 2013, **14**, 13-28; (b) J. Zhang, Y. Wu, M. Xing, S. A. K. Leghari and S. Sajjad, *Energy Environ. Sci.,* 2010, **3**, 715-726; (c) L. G. Devi and R. Kavitha, *Appl. Catal. B: Environ.,* 2013, **140-141**, 559-587; (d) L. G. Devi and R. Kavitha, *RSC Adv.,* 2014, **4**, 28265-28299; (e) R. Asahi, T. Morikawa, H. Irie and T. Ohwaki, *Chem. Rev.,* 2014, **114**, 9824-9852.

(165) S. Sun, X. Chang, X. Li and Z. Li, *Ceram. Int.,* 2013, **39**, 5197-5203.

(166) Y. Qiu, M. Yang, H. Fan, Y. Xu, Y. Shao, X. Yang and S. Yang, *Mater. Lett.,* 2013, **99**, 105-107.

(167) C. Shifu, Z. Wei, Z. Sujuan and L. Wei, *Chem. Eng. J.,* 2009, **148**, 263-269.

(168) (a) K. Chen, G. H. Fan, Y. Zhang and S. F. Ding, *Acta Phys. Chim. Sin.,* 2008, **24**, 61-66; (b) J. Li, R. Kykyneshi, J. Tate and A. W. Sleight, *Solid State Sci.,* 2007, **9**, 613-618.

(169) D. Zhang, J. Gong, J. Ma, G. Han and Z. Wong, *Dalton Trans.,* 2013, **42**, 16556-16561.

(170) Z. Yu, L. C. Yin, Y. Xie, G. Liu, X. Ma and H. M. Cheng, *J. Colloid Interface Sci.,* 2013, **400**, 18-23.

(171) X. Zong, C. Sun, H. Yu, Z. G. Chen, Z. Xing, D. Ye, G. Q. Lu, X. Li and L. Wang, *J. Phys. Chem. C,* 2013, **117**, 4937-4942.

(172) P. Gu, X. Wang, T. Li and H. Meng, *Mater. Res. Bull.,* 2013, **48**, 4699-4703.

(173) H. Qin, W. Li, Y. Xia and T. He, *ACS Appl. Mater. Interfaces,* 2011, **3**, 3152-3156.

(174) D. Li and H. Haneda, *J. Photochem. Photobiol. A: Chem.,* 2003, **155**, 171-178.

(175) D. Li and H. Haneda, *J. Photochem. Photobiol. A: Chem.,* 2003, **160**, 203-212.

(176) D. Li, H. Haneda, N. Ohashi, S. Hishita and Y. Yoshikawa, *Catal. Today,* 2004, **93-95**, 895-901.

(177) D. Li and H. Haneda, *Chemosphere,* 2004, **54**, 1099-1110.

(178) K. Tennakone, O. A. IIeperuma, J. M. S. Bandara and W. C. B. Kiridena, *Semicond. Sci. Technol.,* 1992, **7**, 423-424.

(179) J. S. Lee, O. S. Kwon and J. Jang, *J. Mater. Chem.,* 2012, **22**, 14565-14572.

(180) (a) H. Yoo, C. Bae, Y. Yang, S. Lee, M. Kim, H. Kim, Y. Kim and H. Shin, *Nano Lett.,* 2014, **14**, 4413-4417; (b) Y. Yang, M. Nogami, J. Shi, H. Chen, Y. Liu and S. Qian, *J. Mater.*

Chem., 2003, **13**, 3026-3032; (c) N. Zhang, S. Liu and Y. J. Xu, *Nanoscale,* 2012, **4**, 2227-2238. (d) A. Ayati, A. Ahmadpour, F. F. Bamoharram, B. Tanhaei, M. Manttari and M. Sillanpaa, *Chemosphere,* 2014, **107**, 163-174; (e) R. G. Chaudhuri and S. Paria, *Chem. Rev.,* 2012, **112**, 2373-2433; (f) A. Primo, A. Corma and H. Garcia, *Phys. Chem. Chem. Phys.,* 2011, **13**, 886-910; (g) A. Bumajdad and M. Madkour, *Phys. Chem. Chem. Phys.,* 2014, **16**, 7146-7158; (h) M. Jakob, H. Levanon and P. V. Kamat, *Nano Lett.,* 2003, **3**, 353-358; (i) H. Tada, T. Mitsui, T. Kiyonaga, T. Akita and K. Tanaka, *Nat. Mater.,* 2006, **5**, 782-786.

(181) (a) H. Zhu, X. Chen, Z. Zheng, X. Ke, E. Jaatinen, J. Zhao, C. Guo, T. Xie and D. Wang, *Chem. Commun.,* 2009, 7524-7526; (b) S. Sarina, E. R. Waclawik and H. Zhu, *Green Chem.,* 2013, **15**, 1814-1833; (c) S. Linic, P. Christopher and D. B. Ingram, *Nat. Mater.,* 2011, **10**, 911-921; (d) X. Zhou, G. Liu, J. Yu and W. Fan, *J. Mater. Chem.,* 2012, **22**, 21337-21354.

(182) V. Subramanian, E. E. Wolf and P. V. Kamat, *J. Am. Chem. Soc.,* 2004, **126**, 4943-4950.

(183) Y. Zheng, C. Chen, Y. Zhan, X. Lin, Q. Zheng, K. Wei and J. Zhu, *J. Phys. Chem. C,* 2008, **112**, 10773-10777.

(184) M. M. Montero, A. Borras, Z. Saghi, P. R. Gomez, J. R. S. Valencia. J. C. Gonzalez, A. Barranco, P. Midgley, J. Cotrino and A. R. G. Elipe, *J. Mater. Chem.,* 2012, **22**, 1341-1346.

(185) Q. Deng, X. Duan, D. H. L. Ng, H. Tang, Y. Yang, M. Kong, Z. Wu, W. Cai and G. Wang, *ACS Appl. Mater. Interfaces,* 2012, **4**, 6030-6037.

(186) Y. Zheng, L. Zheng, Y. Zhan, X. Lin, Q. Zheng and K. Wei, *Inorg. Chem.,* 2007, **46**, 6980-6986.

(187) C. Ren, B. Yang, M. Wu, J. Xu, Z. Fu, Y. Lv, T. Guo, Y. Zhao and C. Zhu, *J. Hazard. Mater.,* 2010, **182**, 123-129.

(188) C. Tian, W. Li, K. Pan, Q. Zhang, G. Tian, W. Zhou and H. Fu, *J. Solid State Chem.,* 2010, **183**, 2720-2725.

(189) W. Xie, Y. Li, W. Sun, J. Huang, H. Xie and X. Zhao, *J. Photochem. Photobiol. A: Chem.,* 2010, **216**, 149-155.

(190) (a) A. Sclafani and J. M. Hermann, *J. Photochem. Photobiol. A: Chem.,* 1998, **113**, 181-188. (b) C. Yu, K. Yang, Y. Xie, Q. Fan, J. C. Yu, Q. Shu and C. Wang, *Nanoscale,* 2013, **5**, 2142-2151; (c) B. Chai, X. Wang, S. Cheng, H. Zhou and F. Zhang, *Ceram. Int.,* 2014, **40**, 429-435.

(191) Y. Zhang and J. Mu, *J. Colloid Interface Sci.,* 2007, **309**, 478-484.

(192) R. Georgekutty, M. K. Serry and S. C. Pillai, *J. Phys. Chem. C,* 2008, **112**, 13563-13570.

(193) Q. Simon, D. Barreca, D. Bekermann, A. Gasparotto, C. Maccato, E. Comini, V. Gombac, P. Fornasiero, O. I. Lebedev, S. Turner, A. Devi, R. A. Fischer and G. V. Tendeloo, *Int. J. Hydrogen Energy,* 2011, **36**, 15527-15537.

(194) (a) K. Lalitha, J. K. Reddy, M. V. P. Sharma, V. D. Kumari and M. Subrahmanyam, *Int. J. Hydrogen Energy,* 2010, **35**, 3991-4001; (b) S. Ma, J. Xue, Y. Zhou and Z. Zhang, *J. Mater. Chem. A,* 2014, **2**, 7272-7280; (c) S. M. Lam, J. C. Sin, A. Z. Abdullah and A. R. Mohamed, *Chem. Pap.,* 2013, **67**, 1277-1284; (d) M. Wu, J. Yan, M. Zhao and Q. Jiang, *ChemPlusChem,* 2012, **77**, 931-935.

(195) H. R. Liu, G. X. Shao, J. F. Zhao, Z. X. Zhang, Y. Zhang, J. Liang, X. G. Liu, H. S. Jia and B. S. Xu, *J. Phys. Chem. C,* 2012, **116**, 16182-16190.

(196) C. Gu, C. Cheng, H. Huang, T. Wong, N. Wang and T. Y. Zhang, *Cryst. Growth Des.,* 2009, **9**, 3278-3285.

(197) J. Liqiang, W. Baiqi, X. Baifu, L. Shudan, S. Keying, C. Weimin and F. Honggang, *J. Solid State Chem.,* 2004, **177**, 4221-4227.

(198) B. Tian, J. Zhang, T. Tong and F. Chen, *Appl. Catal. B: Environ.,* 2008, **79**, 394-401.; (b) M. Sadeghi, W. Liu, T. G. Zhang, P. Stavropoulos and B. Levy, *J. Phys. Chem.,* 1996, **100**, 19466-19474.

(199) H. Zeng, P. Liu, W. Cai, S. Yang and X. Xu, *J. Phys. Chem. C,* 2008, **112**, 19620-19624.

(200) P. Li, Z. Wei, T. Wu, Q. Peng and Y. Li, *J. Am. Chem. Soc.,* 2011, **133**, 5660-5663.

(201) (a) Y. Chen, M. Kim, G. Lian, M. B. Johnson and X. Peng, *J. Am. Chem. Soc.,* 2005, **127**, 13331-13337; (b) F. Li, Y. Ding, P. Gao, X. Xin and Z. L. Wang, *Angew. Chem., Int. Ed.,* 2004, **43**, 5238-5242; (c) Z. L. Wang, X. Y. Kong and J. M. Zuo, *Phys. Rev. Lett.,* 2003, **91**, 185502.

(202) M. Ahmad, S. Yingying, A. Nisar, H. Sun, W. Shen, M. Wei and J. Zhu, *J. Mater. Chem.,* 2011, **21**, 7723-7729.

(203) E. C. H. Sykes, F. J. Williams, M. S. Tikhov and R. M. Lambert, *J. Phys. Chem. B,* 2002, **106**, 5390-5394.

(204) Q. Wang, B. Geng and S. Wang, *Environ. Sci. Technol.,* 2009, **43**, 8968-8973.

(205) N. Udawatte, M. Lee, J. Kim and D. Lee, *ACS Appl. Mater. Interfaces,* 2011, **3**, 4531-4538.

(206) (a) M. Lee, P. Amaratunga, J. Kim and D. Lee, *J. Phys. Chem. C,* 2010, **114**, 18366-18371; (b) P. Amaratunga, M. Lee, J. Kim and D. Lee, *Can. J. Chem.,* 2011, **89**, 1001-1009.

(207) J. Lee, H. S. Shim, M. Lee, J. K. Song and D. Lee, *J. Phys. Chem. Lett.,* 2011, **2**, 2840-2845.

(208) P. Pawinrat, O. Mekasuwandumrong and J. Panpranot, *Catal. Commun.,* 2009, **10**, 1380-1385.

(209) A. Wood, M. Giersig and P. Mulvaney, *J. Phys. Chem. B,* 2001, **105**, 8810-8815.

(210) V. Subramanian, E. E. Wolf and P. V. Kamat, *J. Phys. Chem. B,* 2003, **107**, 7479-7485.

(211) (a) A. J. Bard and M. A. Fox, *Acc. Chem. Res.,* 1995, **28**, 141-145; (b) M. Ashokkumar, *Int. J. Hydrogen Energy,* 1998, **23**, 427-438.

(212) J. J. Wu and C. H. Tseng, *Appl. Catal. B: Environ.,* 2006, **66**, 51-57.

(213) W. I. Park, G. C. Yi, J. W. Kim and S. M. Park, *Appl. Phys. Lett.,* 2003, **82**, 4358-4360.

(214) S. Chen, R. S. Ingram, M. J. Hostetler, J. J. Pietron, R. W. Murray, T. G. Schaaff, J. T. Khoury, M. M. Alvarez and R. L. Whetten, S*cience,* 1998, **280**, 2098-2101.

(215) (a) B. Divband, M. Khatamian, G. R. K. Eslamian and M. Darbandi, *Appl. Surf. Sci.,* 2013, **284**, 80-86; (b) D. Lin, H. Wu, R. Zhang and W. Pan, *Chem. Mater.,* 2009, **21**, 3479-3484; (c) Z. Zhang, H. Liu, H. Zhang, H. Dong, X. Liu, H. Jia and B. Xu, *Superlatt. Microstruct.,* 2014, **65**, 134-145; (d) C. Tian, Q. Zhang, B. Jiang, G. Tian and H. Fu, *J. Alloys Compd.,* 2011, **509**, 6935-6941.

(216) (a) R. Marschall, *Adv. Funct. Mater.,* 2014, **24**, 2421-2440; (b) P. Zhou, J. Yu and M. Jaroniec, *Adv. Mater.,* 2014, **26**, 4920-4935; (c) S. G. Kumar and K. S. R. K. Rao, *Energy Environ. Sci.,* 2014, **7**, 45-102; (d) H. Wang, L. Zhang, Z. Chen, J. Hu, S. Li, Z. Wang, J. Liu and X. Wang, *Chem. Soc. Rev.,* 2014, **43**, 5234-5244.

(217) (a) H. Ma, J. Han, Y. Fu, Y. Song, C. Yu and X. Dong, *Appl. Catal. B: Environ.,* 2011, **102**, 417-423; (b) H. G. Kim, P. H. Borse, W. Choi and J. S. Lee, *Angew. Chem., Int. Ed.,* 2005, **44**, 4585-4589; (c) X. Wu, S. Yin, Q. Dong, B. Liu, Y. Wang, T. Sekino, S. W. Lee and T. Sato, *Sci. Rep.,* 2013, **3**, 2918; (d) Y. Chen, J. C. Crittenden, S. Hackney, L. Sutter and D. W. Hand, *Environ. Sci. Technol.,* 2005, **39**, 1201-1208; (e) S. Ida, A. Takashiba, S. Koga, H. Hagiwara and T. Ishihara, *J. Am. Chem. Soc.,* 2014, **136**, 1872-1878.

(218) D. Chen, H. Zhang, S. Hu and J. Li, *J. Phys. Chem. C,* 2008, **112**, 117-122.

(219) (a) M. Law, L. E. Greene, A. Radenovic, T. Kuykendall, J. Liphardt and P. Yang, *J. Phys. Chem. B,* 2006, **110**, 22652-22663; (b) J. Tian, Z. Zhao, A. Kumar, R. I. Boughton and H. Liu, *Chem. Soc. Rev.,* 2014, **43**, 6920-6937; (c) B. Weng, S. Liu, Z. R. Tang and Y. J. Xu, *RSC Adv.,* 2014, **4**, 12685-12700.

(220) Q. Zhang, W. Fan and L. Gao, *Appl. Catal. B: Environ.,* 2007, **76**, 168-173.

(221) J. Tian, L. Chen, Y. Yin, X. Wang, J. Dai, Z. Zhu, X. Liu and P. Wu, *Surf. Coat. Technol.,* 2009, **204**, 205-214.

(222) J. Tian, J. Wang, J. Dai, X. Wang and Y. Yin, *Surf. Coat. Technol.,* 2009, **204**, 723-730.

(223) J. Mani, H. Sakeek, S. Habouti, M. Dietze and M. E. Souni, *Catal. Sci. Technol.,* 2012, **2**, 379-385.

(224) (a) K. Mallick and M. S. Scurrell, *Appl. Catal. A: Gen.,* 2003, **253**, 527-536; (b) C. H. Wu, *Chemosphere,* 2004, **57**, 601-608.

(225) S. Liao, H. Donggen, D. Yu, Y. Su and G. Yuan, *J. Photochem. Photobiol. A: Chem.,* 2004, **168**, 7-13.

(226) M. Konyar, H. C. Yatmaz and K. Ozturk, *Appl. Surf. Sci.,* 2012, **258**, 7440-7447.

(227) G. Yang, Z. Yan and T. Xiao, *Appl. Surf. Sci.,* 2012, **258**, 8704-8712.

(228) C. Wang, B. Q. Xu, X. Wang and J. Zhao, *J. Solid State Chem.,* 2005, **178**, 3500-3506.

(229) Y. Wei, Y. Huang, J. Wu, M. Wang, C. Guo, Q. Dong, S. Yin and T. Sato, *J. Hazard. Mater.,* 2013, **248-249**, 202-210.

(230) (a) J. Yang and J. H. Swisher, *Mater. Charact.,* 1996, **37**, 153-159; (b) C. L. Wang, W. S. Hwang, H. L. Chu, C. S. Hsi, H. H. Ko, K. M. Chang, X. Zhao, M. C. Wang and W. L. Li,

Ceram. Int., 2014, **40**, 7407-7415; (c) Y. L. Chai, Y. S. Chang, G. J. Chen and Y. J. Hsiao, *Mater. Res. Bull.,* 2008, **43**, 1066-1073.

(231) Z. Zhang, C. Shao, X. Li, L. Zhang, H. Xue, C. Wang and Y. Liu, *J. Phys. Chem. C,* 2010. **114**, 7920-7925.

(232) L. Zheng, Y. Zheng, C. Chen, Y. Zhan, X. Lin, Q. Zheng, K. Wei and J. Zhu, *Inorg. Chem.,* 2009, **48**, 1819-1825.

(233) Md. T. Uddin, Y. Nicolas, C. Olivier, T. Toupance, L. Servant, M. M. Muller, H. J. Kleebe, J. Ziegler and W. Jaegermann, *Inorg. Chem.,* 2012, **51**, 7764-7773.

(234) D. Y. T. Martinez, R. C. Perez, G. T. Delgado and O. Z. Angel, *J. Photochem. Photobiol. A: Chem.,* 2012, **235**, 49-55.

(235) C. Wang, X. Wang, B. Q. Xu, J. Zhao, B. Mai, P. Peng, G. Sheng and J. Fu, *J. Photochem. Photobiol. A: Chem.,* 2004, **168**, 47-52.

(236) (a) T. Hashemi, H. M. Al-Allak, J. Illingsworth, A. W. Brinkman and J. Woods, *J. Mater. Sci. Lett.,* 1990, **9**, 776-778; (b) F. Belliard, P. A. Connor and J. T. S. Irvine, *Solid State Ionics,* 2000, **135**, 163-167; (c) J. Fang, A. Huang, P. Zhu, N. Xu, J. Xie, J. Chi, S. Feng, R. Xu and M. Wu, *Mater. Res. Bull.,* 2001, **36**, 1391-1397.

(237) X. Huang, L. Shang, S. Chen, J. Xia, X. Qi, X. Wang, T. Zhang and X. M. Meng, *Nanoscale,* 2013, **5**, 3828-3833.

(238) K. Tennakone and J. Bandara, *Appl. Catal. A: Gen.,* 2001, **208**, 335-341.

(239) (a) Q. Kuang, Z. Y. Jiang, Z. X. Xie, S. C. Lin, Z. W. Lin, S. Y. Xie, R. B. Huang and L. S. Zheng, *J. Am. Chem. Soc.,* 2005, **127**, 11777-11784; (b) M. Davis, W. M. Hikal, C. Gumeci and L. J. H. Weeks, *Catal. Sci. Technol.,* 2012, **2**, 922-924; (c) M. Li, Y. Hu, S. Xie, Y. Huang, Y. Tong and X. Lu, *Chem. Commun.,* 2014, 4341-4343; (d) S. Balachandran, K. Selvam, B.

Babu and M. Swaminathan, *Dalton Trans.,* 2013, **42**, 16365-16374; (e) H. Wang, S. Baek, J. Lee and S. Lim, *Chem. Eng. J,* 2009, **146**, 355-361.

(240) Z. L. Liu, J. C. Deng, J. J. Deng and F. F. Li, *Mater. Sci. Eng. B,* 2008, **150**, 99-104.

(241) R. Saravanan, S. Karthikeyan, V. K. Gupta, G. Sekaran, V. Narayanan and A. Stephen, *Mater. Sci. Eng. C,* 2013, **33**, 91-98.

(242) C. C. Hsu and N. L. Wu, *J. Photochem. Photobiol. A: Chem.,* 2005, **172**, 269-274.

(243) C. Shifu, Z. Wei, L. Wei, Z. Huaye and Y. Xiaoling, *Chem. Eng. J.,* 2009, **155**, 466-473.

(244) (a) C. Shifu, C. Lei, G. Shen and C. Gengyu, *Mater. Chem. Phys.,* 2006, **98**, 116-120; (b) C. Shifu, Z. Wei, L. Wei, Z. Huaye, Y. Xiaoling and C. Yinghao, *J. Hazard. Mater.,* 2009, **172**, 1415-1423.

(245) N. V. Kaneva and C. D. Dushkin, *Colloids Surf. A: Physicochem. Eng. Aspects,* 2011, **382**, 211-218.

(246) X. Guo, H. Zhu and Q. Li, *Appl. Catal. B: Environ.,* 2014, **160-161**, 408-414.

(247) W. Liu, M. Wang, C. Xu, S. Chen and X. Fu, *Mater. Res. Bull.,* 2013, **48**, 106-113.

(248) Z. Yi, J. Ye, N. Kikugawa, T. Kako, S. Ouyang, H. S. Williams, H. Yang, J. Cao, W. Luo, Z. Li, Y. Liu and R. L. Withers, *Nat. Mater.,* 2010, **9**, 559-564; (b) Y. Bi, S. Ouyang, J. Cao and J. Ye, *Phys. Chem. Chem. Phys.,* 2011, **13**, 10071-10075.

(249) Z. Zhan, Y. Wang, Z Lin, J. Zhang and F. Huang, *Chem. Commun.,* 2011, 4517-4519.

(250) J. M. Khoshman and M. E. Kordesch, *Thin Solid Films,* 2007, **515**, 7393-7399.

(251) F. Zhou, X. Li, J. Shu and J. Wang, *J. Photochem. Photobiol. A: Chem.,* 2011, **219**, 132-138.

(252) (a) L. Gai, L. Ma, H. Jiang, Y. Ma, Y. Tian and H. Liu, *CrystEngComm,* 2012, **14**, 7479-7486; (b) Z. Wang, B. Huang, Y. Dai, X. Qin, X. Zhang, P. Wang, H. Liu and J. Yu, *J. Phys. Chem. C,* 2009, **113**, 4612-4617.

(253) W. Wu, S. Zhang, X. Xiao, J. Zhou, F. Ren, L. Sun and C. Jiang, *ACS Appl. Mater. Interfaces,* 2012, **4**, 3602-3609.

(254) Z. Zhang, C. Shao, X. Li, C. Wang, M. Zhang and Y. Liu, *ACS Appl. Mater. Interfaces,* 2010, **2**, 2915-2923.

(255) (a) H. Ohta, M. Hirano, K. Nakahara, H. Maruta, T. Tanabe, M. Kamiya, T. Kamiya and H. Hosono, *Appl. Phys. Lett.,* 2003, **83**, 1029-1031; (b) M. J. Ma, B. Lu, T. T. Zhou, Z. Z. Ye, J. G. Lu and X. H. Pan, *J. Appl. Phys.,* 2013, **113,** 163704; (c) J. Wang, C. Lee, Y. Chen, C. Chen, Y. Chen, C. Lin and Y. Chen, *Appl. Phys. Lett.,* 2009, **95**, 131117.

(256) B. Li and Y. Wang, *J. Phys. Chem. Solids,* 2011, **72**, 1165-1169.

(257) X. Cao, P. Chen and Y. Guo, *J. Phys. Chem. C,* 2008, **112**, 20560-20566.

(258) (a) Y. Tak, S. J. Hong, J. S. Lee and K.Yong, *J. Mater. Chem.,* 2009, **19**, 5945-5951; (b) Y. Choi, M. Beak and K. Yong, *Nanoscale,* 2014, **6**, 8914-8918.

(259) F. Xu, Y. Yuan, H. Han, D. Wu, Z. Gao and K. Jiang, *CrystEngComm,* 2012, **14**, 3615-3622.

(260) P. Kundu, P. A. Deshpande, G. Madras and N. Ravishankar, *J. Mater. Chem.,* 2011, **21**, 4209-4216.

(261) M. Villani, D. Calestani, L. Lazzarini, L. Zanotti, R. Mosca and A. Zappettini, *J. Mater. Chem.,* 2012, **22**, 5694-5699.

(262) H. M. Pathan and C. D. Lokhande, *Bull. Mater. Sci.,* 2004, **27**, 85-111.

(263) S. Khanchandani, S. Kundu, A. Patra and A. K. Ganguli, *J. Phys. Chem. C,* 2012, **116**, 23653-23662.

(264) S. Hotchandani and P. V. Kamat, *J. Phys. Chem.,* 1992, **96**, 6834-6839.

(265) J. Nayak, S. N. Sahu, J. Kasuya and S. Nozaki, *Appl. Surf. Sci.,* 2008, **254**, 7215-7218.

(266) C. Li, T. Ahmed, M. Ma, T. Edvinsson and J. Zhu, *Appl. Catal. B: Environ.,* 2013, **138-139**, 175-183.

(267) H. X. Sang, X. T. Wang, C. C. Fan and F. Wang, *Int. J. Hydrogen Energy,* 2012, **37**, 1348-1355.

(268) M. Basu, N. Garg and A. K. Ganguli, *J. Mater. Chem. A,* 2014, **2**, 7517-7525.

(269) (a) P. Zhang, C. Shao, Z. Zhang, M. Zhang, J. Mu, Z. Guo and Y. Liu, *Nanoscale,* 2011, **3**, 2943-2949; (b) P. Zhang, C. Shao, Z. Zhang, M. Zhang J. Mu, Z. Guo, Y. Sun and Y. Liu, *J. Mater. Chem.,* 2011, **21**, 17746-17753; (c) V. Kiran and S. Sampath, *Nanoscale,* 2013, **5**, 10646-10652.

(270) X. Zhou, Y. Li, T. Peng, W. Xie and X. Zhao, *Mater. Lett.,* 2009, **63**, 1747-1749.

(271) S. Liu, C. Li, J. Yu and Q. Xiang, *CrystEngComm,* 2011, **13**, 2533-2541.

(272) S. Cho, J. W. Jang, J. S. Lee and K. H. Lee, *CrystEngComm,* 2010, **12**, 3929-3935.

(273) S. Cho, H. Jeong, D. H. Park, S. H. Jung, H. J. Kim and K. H. Lee, *CrystEngComm,* 2010, **12**, 968-976.

(274) S. T. Kochuveedu, Y. H. Jang, Y. J. Jang and D. H. Kim, *J. Mater. Chem. A*, 2013, **1**, 898-905.

(275) M. Zhou, X. Gao, Y. Hu, J. Chen and X. Hu, *Appl. Catal. B: Environ.,* 2013, **138-139**, 1-8.

(276) F. Waltz, G. Wißmann, J. Lippke, A. M. Schneider, H. C. Schwarz, A. Feldhoff, S. Eiden and P. Behrens, *Cryst. Growth Des.,* 2012, **12**, 3066-3075.

(277) J. Mu, C. Shao, Z. Guo, Z. Zhang, M. Zhang, P. Zhang, B. Chen and Y. Liu, *ACS Appl. Mater. Interfaces,* 2011, **3**, 590-596.

(278) (a) L. Zhang, D. Austin, V. I. Merkulov, A. Meleshko, K. L. Klein, M. A. Guillorn, D. H. Lowndes and M. L. Simpson, *Appl. Phys. Lett.,* 2004, **84**, 3972-3974; (b) H. E. Unalan, D. Wei, K. Suzuki, S. Dalal, P. Hiralal, H. Matsumoto, S. Imaizumi, M. Minagawa, A. Tanioka, A. J. Flewitt, W. I. Milne and G. A. Amaratunga, *Appl. Phys. Lett.,* 2008, **93**, 133116.

(279) N. Sobana and M. Swamtinathan, *Solar Energy Mater. Sol. Cells,* 2007, **91**, 727-734.

(280) Y. Gao, H. Wang, C. He, L. Qiu and X. Cao, *Langmuir,* 2009, **25**, 4678-4684.

(281) S. Ma, J. Xue, Y. Zhou, Z. Zhang and X. Wu, *CrystEngComm,* 2014, **16**, 4478-4484.

(282) H. F. Yu and H. Y. Chou, *Powder Technol.,* 2013, **233**, 201-207.

(283) S. Lian, H. Huang, J. Zhang, Z. Kang and Y. Liu, *Solid State Commun.,* 2013, **155**, 53-56.

(284) L. Zhang, H. Cheng, R. Zong and Y. Zhu, *J. Phys. Chem. C,* 2009, **113**, 2368-2374.

(285) (a) G. Yu, J. Gao, J. C. Hummelen, F. Wudl and A. J. Heeger, *Science,* 1995, **270**, 1789-1791; (b) W. J. D. Beenken, *Chem. Phys.,* 2009, **357**, 144-150; (c) L. Zhao, X. Chen, X. Wang, Y. Zhang, W. Wei and Y. Sun, M Antonietti and M. M. Titirici, *Adv. Mater.,* 2010, **22**, 3317-3321.

(286) (a) S. Chowdhury and R. Balasubramanian, *Appl. Catal. B: Environ.,* 2014, **160-161**, 307-324; (b) N. Zhang, Y. Zhang and Y. J. Xu, *Nanoscale,* 2012, **4**, 5792-5813; (c) D. Chen, H. Zhang, Y. Liu and J. Li, *Energy Environ. Sci.,* 2013, **6**, 1362-1387; (d) X. An and J. C. Yu, *RSC Adv.,* 2011, **1**, 1426-1434; (e) Q. Xiang, J. Yu and M. Jaroniec, *Chem. Soc. Rev.,* 2012, **41**, 782-796; (f) R. Leary and A. Westwood, *Carbon,* 2011, **49**, 741-772.

(287) Q. Zhang, C. Tian, A. Wu, T. Tan, L. Sun, L. Wang and H. Fu, *J. Mater. Chem.,* 2012, **22**, 11778-11784.

(288) Y. Yang, L. Ren, C. Zhang, S. Huang and T. Liu, *ACS Appl. Mater. Interfaces,* 2011, **3**, 2779-2785.

(289) B. Li, T. Liu, Y. Wang and Z. Wang, *J. Colloid Interface Sci.,* 2012, **377**, 114-121.

(290) B. Li and H. Cao, *J. Mater. Chem.,* 2011, **21**, 3346-3349.

(291) (a) Z. Xiong, L. L. Zhang, J. Ma and X. S. Zhao, *Chem. Commun.,* 2010, 6099-6101; (b) N. Yang, J. Zhai, D. Wang, Y. Chen and L. Jiang, *ACS Nano,* 2010, **4**, 887-894; (c) T. Lv, L. Pan, X. Liu and Z. Sun, *Catal. Sci. Technol.,* 2012, **2**, 2297-2301.

(292) P. V. Kamat, *Chem. Rev.,* 1993, **93**, 267-300.

(293) X. Liu, L. Pan, T. Lv, T. Lu, G. Zhu, Z. Sun and C. Sun, *Catal. Sci. Technol.,* 2011, **1**, 1189-1193.

(294) (a) Y. B. Tang, C. S. Lee, J. Xu, Z. T. Liu, Z. H. Chen, Z. He, Y. L. Cao, G. Yuan, H. Song, L. Chen, L. Luo, H. M. Cheng, W. J. Zhang, I. Bello and S. T. Lee, *ACS Nano,* 2010, **4**, 3482-3488; (b) Z. Chen, N. Zhang and Y. J. Xu, *CrystEngComm,* 2013, **15**, 3022-3030; (c) D. Fu, G. Han, F. Yang, T. Zhang, Y. Chang and F. Liu, *Appl. Surf. Sci.,* 2013, **283**, 654-659.

(295) D. Fu, G. Han, Y. Chang and J. Dong, *Mater. Chem. Phys.,* 2012, **132**, 673-681.

(296) T. Xu, L. Zhang, H. Cheng and Y. Zhu, *Appl. Catal. B: Environ.,* 2011, **101**, 382-387.

(297) S. Gayathri, P. Jayabal, M. Kottaisamy and V. Ramakrishnan, *J. Appl. Phys.,* 2014, **115**, 173504.

(298) Y. Liu, Y. Hu, M. Zhou, H. Qian and X. Hu, *Appl. Catal. B: Environ.,* 2012, **125**, 425-431.

(299) X. Liu, L. Pan, Q. Zhao, T. Lv, G. Zhu, T. Chen, T. Lu, Z. Sun and C. Sun, *Chem. Eng. J.,* 2012, **183**, 238-243.

(300) J. Wang, T. Tsuzuki, B. Tang, X. Hou, L. Sun and X. Wang, *ACS Appl. Mater. Interfaces,* 2012, **4**, 3084-3090.

(301) (a) S. Cao and J. Yu, *J. Phys. Chem. Lett.,* 2014, **5**, 2101-2107; (b) F. Dong, L. Wu, Y. Sun, M. Fu, Z. Wu and S. C. Lee, *J. Mater. Chem.,* 2011, **21**, 15171-15174; (c) F. Dong, Z. Zhao, T. Xiong, Z. Ni, W. Zhang, Y. Sun and W. K. Ho, *ACS Appl. Mater. Interfaces,* 2013, **5**, 11392-11401; (d) Y. Cao, Z. Zhang, J. Long, J. Liang, H. Lin, H. Lin and X. Wang, *J. Mater. Chem. A,* 2014, **2**, 17797-17807.

(302) (a) F. Dong, Y. Sun, L. Wu, M. Fu and Z. Wu, *Catal. Sci. Technol.,* 2012, **2**, 1332-1335; (b) W. Zhang, Y. Sun, F. Dong, W. Zhang, S. Duan and Q. Zhang, *Dalton Trans.,* 2014, **43**, 12026-12036; (c) Z. Zhao, Y. Sun and F. Dong, *Nanoscale,* 2014, **DOI:** 10.1039/C4NR03008G; (d) A. Thomas, A. Fischer, F. Goettmann, M. Antonietti, J. O. Muller, R. Schlogl and J. M. Carlsson, *J. Mater. Chem.,* 2008, **18**, 4893-4908; (e) Y. Zheng, J. Liu, J. Liang, M. Jaroniec and S. Z. Qiao, *Energy Environ. Sci.,* 2012, **5**, 6717-6731.

(303) Y. Wang, R. Shi, J. Lin and Y. Zhu, *Energy Environ. Sci.,* 2011, **4**, 2922-2929.

(304) S. C. Yan, S. B. Lv, Z. S. Li and Z. G. Zou, *Dalton Trans.,* 2010, **39**, 1488-1491.

(305) J. X. Sun, Y. P. Yuan, L. G. Qiu, X. Jiang, A. J. Xie, Y. H. Shen and J. F. Zhu, *Dalton Trans.,* 2012, **41**, 6756-6763.

(306) W. Liu, M. Wang, C. Xu, S. Chen and X. Fu, *J. Mol. Catal. A: Chem.,* 2013, **368-369**, 9-15.

(307) W. Liu, M. Wang, C. Xu and S. Chen, *Chem.Eng. J,* 2012, **209**, 386-393.

(308) D. Chen, K. Wang, D. Xiang, R. Zong, W. Yao and Y. Zhu, *Appl. Catal. B: Environ.,* 2014, **147**, 554-561.

(309) D. Chen, K. Wang, T. Ren, H. Ding and Y. Zhu, *Dalton Trans.,* 2014, **43**, 13105-13114.

(310) Y. P. Zhu, M. Li, Y. L. Liu, T. Z. Ren and Z. Y. Yuan, *J. Phys. Chem. C,* 2014, **118**, 10963-10971.

(311) L. Jiang, W. Zhang, Y. Yu and J. Wang, *Electrochem. Commun.,* 2011, **13**, 627-630.

(312) W. Zhang, L. Jiang and J. Ye, *J. Phys. Chem. C,* 2009, **113**, 16247-16253.

(313) T. A. Saleh, M. A. Gondal and Q. A. Drmosh, *Nanotechnology,* 2010, **21**, 495705.

(314) X. Liu, L. Pan, T. Lv, Z. Sun and C. Sun, *J. Mol. Catal. A: Chem.,* 2012, **363-364**, 417-422.

(315) (a) K. Woan, G. Pyrgiotakis and W. Sigmund, *Adv. Mater.,* 2009, **21**, 2233-2239; (b) G. Zhu, L. Pan, T. Lu, T. Xu and Z. Sun, *J. Mater. Chem.,* 2011, **21**, 14869-14875; (c) H. Chu, L. Wei, R. Cui, J. Wang and Y. Li, *Coord. Chem. Rev.,* 2010, **254**, 1117-1134; (d) Y. Yu, J. C. Yu, J. Yu, Y. Kwok, Y. Che, J. Zhao, L. Ding, W. Ge and P. Wong, *Appl. Catal. A: Gen.,* 2005, **289**, 186-196.

(316) (a) O. Akhavan, R. Azimirad, S. Safa and M. M. Larijani, *J. Mater. Chem.,* 2010, **20**, 7386-7392; (b) I. Shakir, J. H. Choi, M. Shahid, Z. Ali and D. J. Kang, *J. Mater. Chem.,* 2012, **22**, 20549-20553; (c) L. Tian, L. Ye, J. Liu and L. Zan, *Catal. Commun.,* 2012, **17**, 99-103.

(317) M. Samadi, H. A. Shivaee, M. Zanetti, A. Pourjavadi and A. Moshfegh, *J. Mol. Catal. A: Chem.,* 2012, **359**, 42-48.

(318) C. Yu, Y. Wang, Y. Liu, C. Guo and Y. Hu, *Mater. Lett.,* 2013, **100**, 278-281.

(319) R. M. Mohamed and M. A. Salam, *Mater. Res. Bull.,* 2014, **50**, 85-90.

(320) H. Fu, T. Xu, S. Zhu and Y. Zhu, *Environ. Sci. Technol.,* 2008, **42**, 8064-8069.

(321) P. V. Kamat, *J. Am. Chem. Soc.,* 1991, **113**, 9705-9707.

(322) T. Hasobe, S. Hattori, P. V. Kamat and S. Fukuzumi, *Tetrahedron,* 2006, **62**, 1937-1946.

(323) H. Yu, H. Zhang, H. Huang, Y. Liu, H. Li, H. Ming and Z. Kang, *New J. Chem.,* 2012, **36**, 1031-1035.

(324) (a) H. Zhang, H. Ming, S. Lian, H. Huang, H. Li, L. Zhang, Y. Liu, Z. Kang and S. T. Lee, *Dalton Trans.,* 2011, **40**, 10822-10825; (b) H. Li, X. He, Z. Kang, H. Huang, Y. Liu, J. Liu, S. Lian, C. H. A. Tsang, X. Yang and S. T. Lee, *Angew. Chem., Int. Ed.,* 2010, **49**, 4430-4434; (c) X. Yu, J. Liu, Y. Yu, S. Zuo and B. Li, *Carbon,* 2014, **68**, 718-724; (d) H. Wang, Z. Wei, H. Matsui and S. Zhou, *J. Mater. Chem. A,* 2014, **2**, 15740-15745; (e) C. Han, M. Q. Yang, B. Weng and Y. J. Xu, *Phys. Chem. Chem. Phys.,* 2014, **16**, 16891-16903.

(325) (a) W. J. Ong, L. L. Tan, S. P. Chai, S. T. Yong, A. R. Mohamed, *Nanoscale,* 2014, **6**, 1946-2008; (b) G. Liu, H. G. Yang, J. Pan Y. Q. Yang, G. Q. Lu and H. M. Cheng, *Chem. Rev.,* 2014, **114**, 9559-9612; (c)Y. Xia, Y. Xiong, B. Lim and S. E. Skrabalak, *Angew. Chem., Int. Ed.,* 2008, **48**, 60-103; (d) W. J. Ong, L. L. Tan, S. P. Chai, S. T. Yong and A. R. Mohamed, *ChemSusChem.,* 2014, **7**, 690-719; (e) W. Q. Fang, X. Q. Gong and H. G Yang, *J. Phys. Chem. Lett.,* 2011, **2**, 725-734; (f) E. Grabowska, M. Diak, M. Marchelek and A. Zaleska, *Appl. Catal. B: Environ.,* 2014, **156-157**, 213-235.

(326) L. Zhang, L. Yin, C. Wang, N. Lun and Y. Qi, *ACS Appl. Mater. Interfaces,* 2010, **2**, 1769-1773.

(327) S. He, S. Zhang, J. Lu, Y. Zhao, J. Ma, M. Wei, D. G. Evans and X. Duan, *Chem. Commun.,* 2011, 10797-10799.

(328) H. Lu, S. Wang, L. Zhao, J. Li, B. Dong and Z. Xu, *J. Mater. Chem.,* 2011, **21**, 4228-4234.

(329) (a) X. Wang, J. C. Yu, C. Ho, Y. Hou and X. Fu, *Langmuir,* 2005, **21**, 2552-2559; (b) L. Zhang and J. C. Yu, *Chem. Commun.,* 2003, 2078-2079.

(330) J. Chang and E. R. Waclawik, *CrystEngComm,* 2012, **14**, 4041-4048.

(331) J. Yang, J. Wang, X. Li, J. Lang, F. Liu, L. Yang, H. Zhai, M. Gao and X. Zhao, *J. Alloys Compd.,* 2012, **528**, 28-33.

(332) L. Jia, W. Cai, H. Wang and H. Zeng, *Cryst. Growth Des.,* 2008, **8**, 4367-4371.

(333) R. Boppella, K. Anjaneyulu, P. Basak and S. V. Manorama, *J. Phys. Chem. C,* 2013, **117**, 4597-4605.

(334) L. Zhang, H. Yang, J. Ma, L. Li, X. Wang, L. Zhang, S. Tian and X. Wang, *Appl. Phys. A,* 2010, **100**, 1061-1067.

(335) D. Li, V. Balek, N. Ohashi, T. Mitsuhashi, S. Hishita and H. Haneda, *J. Colloid Interface Sci.,* 2005, **289**, 472-478.

(336) Y. Yamaguchi, M. Yamazaki, S. Yoshihara and T. Shirakashi, *J. Electroanal. Chem.,* 1998, **442**, 1-3.

(337) D. Li, H. Haneda, N. Ohashi, N. Saito and S. Hishita, *Thin Solid Films,* 2005, **486**, 20-23.

(338) S. Cho, J. W. Jang, J. S. Lee and K. H. Lee, *Langmuir,* 2010, **26**, 14255-14262.

(339) A. Wander and N. M. Harrison, *Surf. Sci.,* 2000, **468**, L851-L855.

(340) J. H. Zeng, B. B. Jin and Y. F. Wang, *Chem. Phys. Lett.,* 2009, **472**, 90-95.

(341) M. Farbod and E. Jafarpoor, *Mater. Lett.,* 2012, **85**, 47-49.

(342) X. Wang, L. Yin, G. Liu, L. Wang, R. Saito, G. Q. Lu and H. M. Cheng, *Energy Environ. Sci.,* 2011, **4**, 3976-3979.

(343) U. Rau and M. Schmidt, *Thin Solid Films,* 2001, **387**, 141-146.

(344) Z. B. Yu, Y. P. Xie, G. Liu, G. Q. Lu, X. L. Ma and H. M. Cheng, *J. Mater. Chem. A,* 2013, **1**, 2773-2776.

(345) M. Huang, Y. Yan, W. Feng, S. Weng, Z. Zheng, X. Fu and P. Liu, *Cryst. Growth Des.,* 2014, **14**, 2179-2186.

(346) G. R. Li, T. Hu, G. L. Pan, T. Y. Yan, X. P. Gao and H. Y. Zhu, *J. Phys. Chem. C,* 2008, **112**, 11859-11864.

(347) G. Tang, S. Tian, Z. Zhou, Y. Wen, A. Pang, Y. Zhang, D. Zeng, H. Li, B. Shan and C. Xie, *J. Phys. Chem. C,* 2014, **118**, 11833-11841.

(348) Y. Chen, H. Zhao, B. Liu and H. Yang, *Appl. Catal. B: Environ.,* 2015, **163**, 189-197.

(349) X. G. Han, H. Z. He, Q. Kuang, X. Zhou, X. H. Zhang, T. Xu, Z. X. Xie and L. S. Zheng, *J. Phys. Chem. C,* 2009, **113**, 584-589.

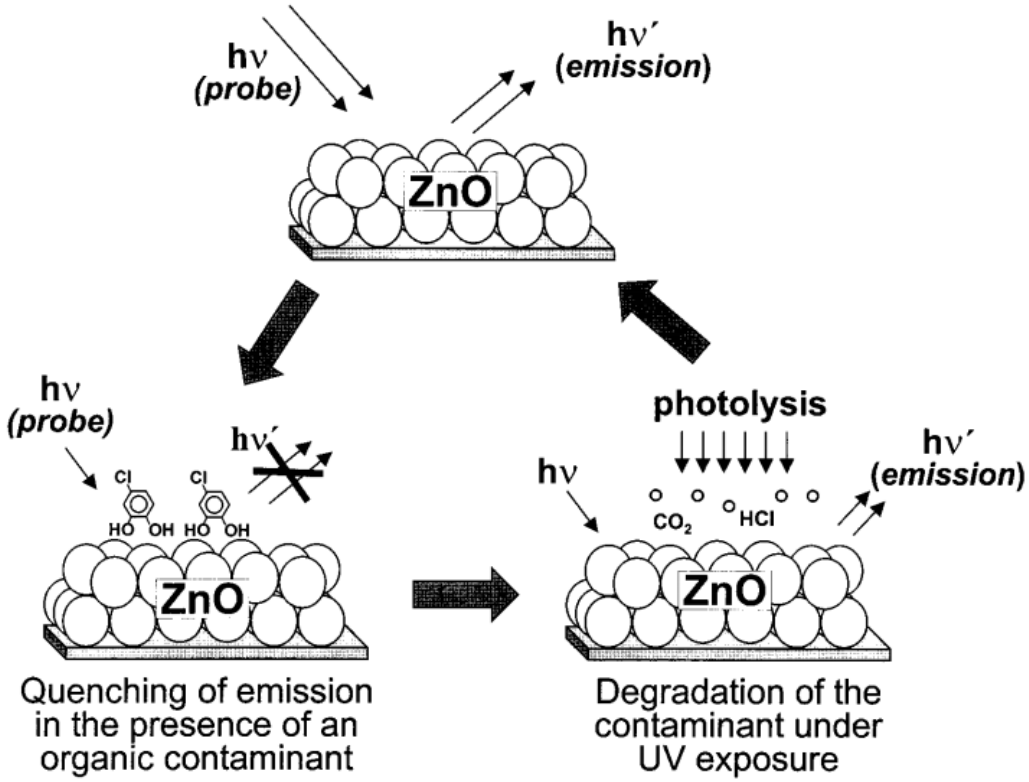

Fig. 1 Illustrating the 'sense and shoot' approach in photocatalysis (reprinted with permission from ref. 16; Copyright 2002 @ American Chemical Society).

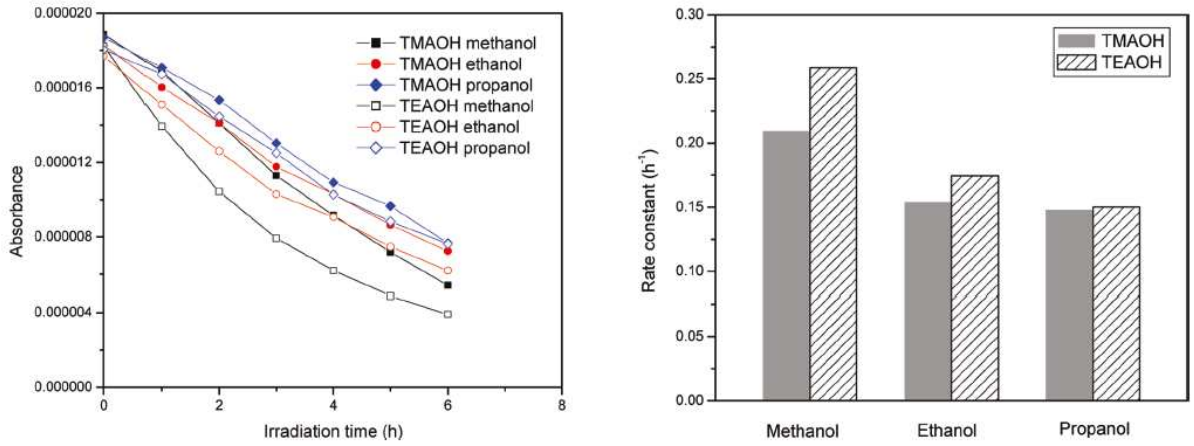

Fig. 2 Degradation kinetics of RhB (left) and rate constants (right) with ZnO synthesized with different solvents (reprinted with permission from ref. 62; Copyright 2011 @ American Chemical Society).

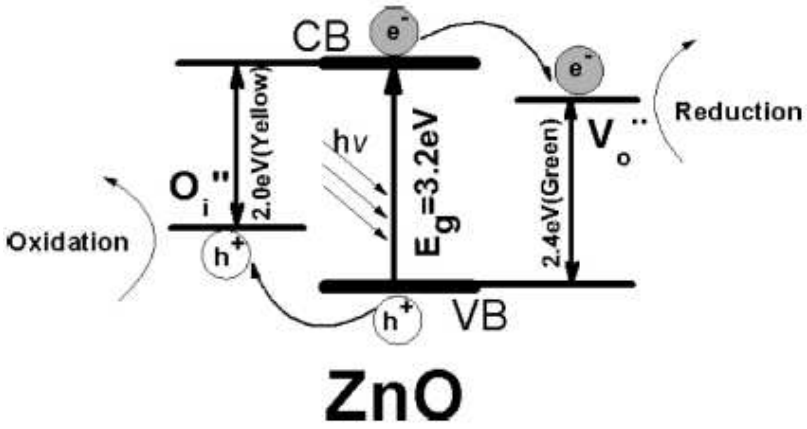

Fig. 3 Band structure and charge transfer pathways of ZnO nanocrystal with oxygen defects (reprinted with permission from ref. 81; Copyright 2009 @ American Chemical Society).

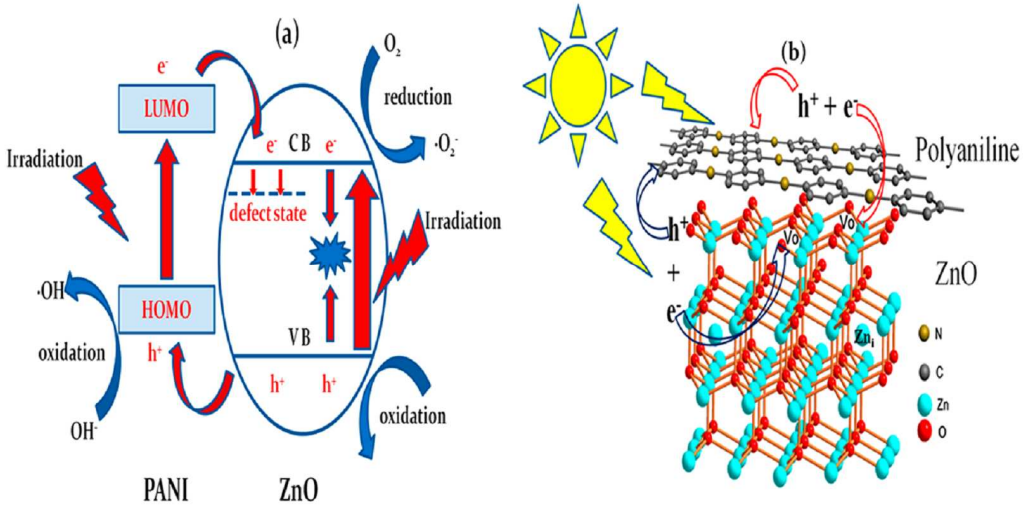

Fig. 4 (a) Proposed photocatalytic mechanism; (b) atomic level illustration of ZnO-PANI hybrids (reprinted with permission from ref. 87; Copyright 2014 @ American Chemical Society).

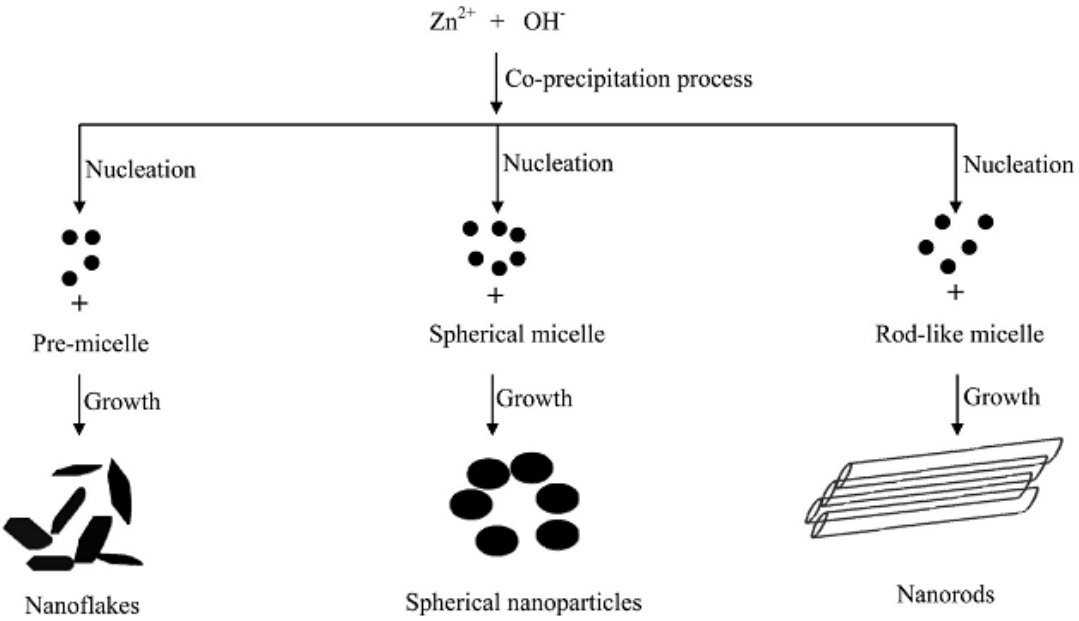

Fig. 5 Formation mechanism of ZnO nanostructures with different morphologies (reprinted with permission from ref. 95; Copyright 2012 @ American Chemical Society).

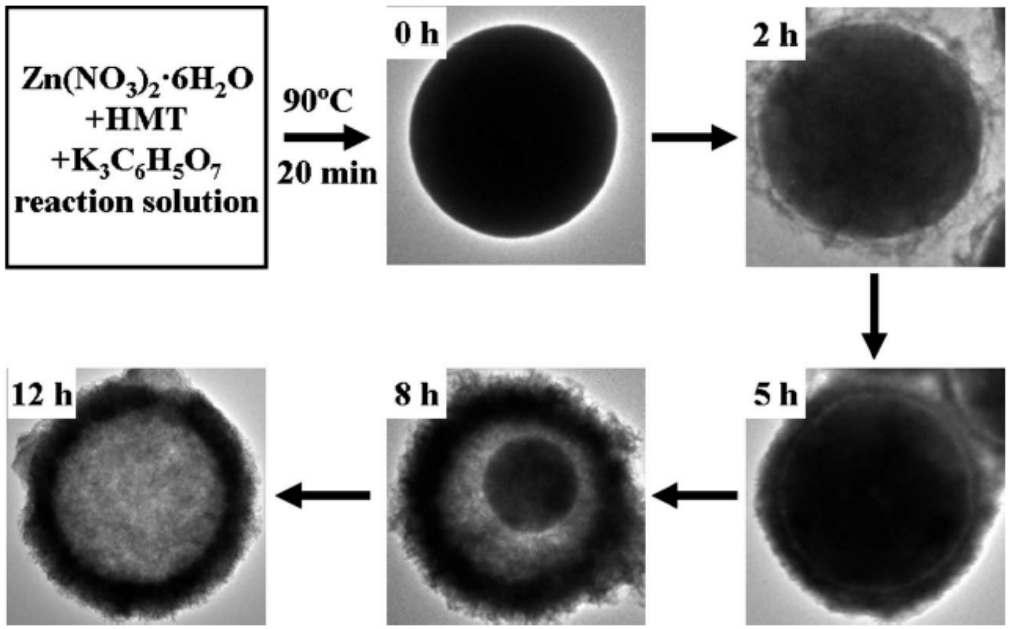

Fig. 6 Morphology evolution for zinc citrate microspheres with aging time (reprinted with permission from ref. 117; Copyright 2012 @ Royal Society of Chemistry).

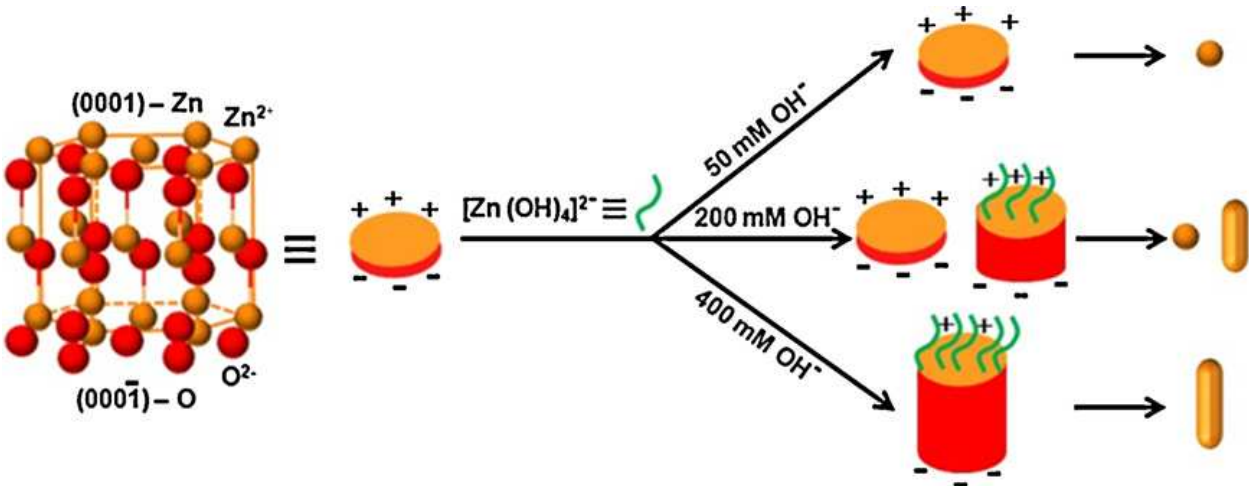

Fig. 7 Formation mechanism for different ZnO nanostructures under the influence of hydroxyl anions (reprinted with permission from ref. 121; Copyright 2011 @ Elsevier).

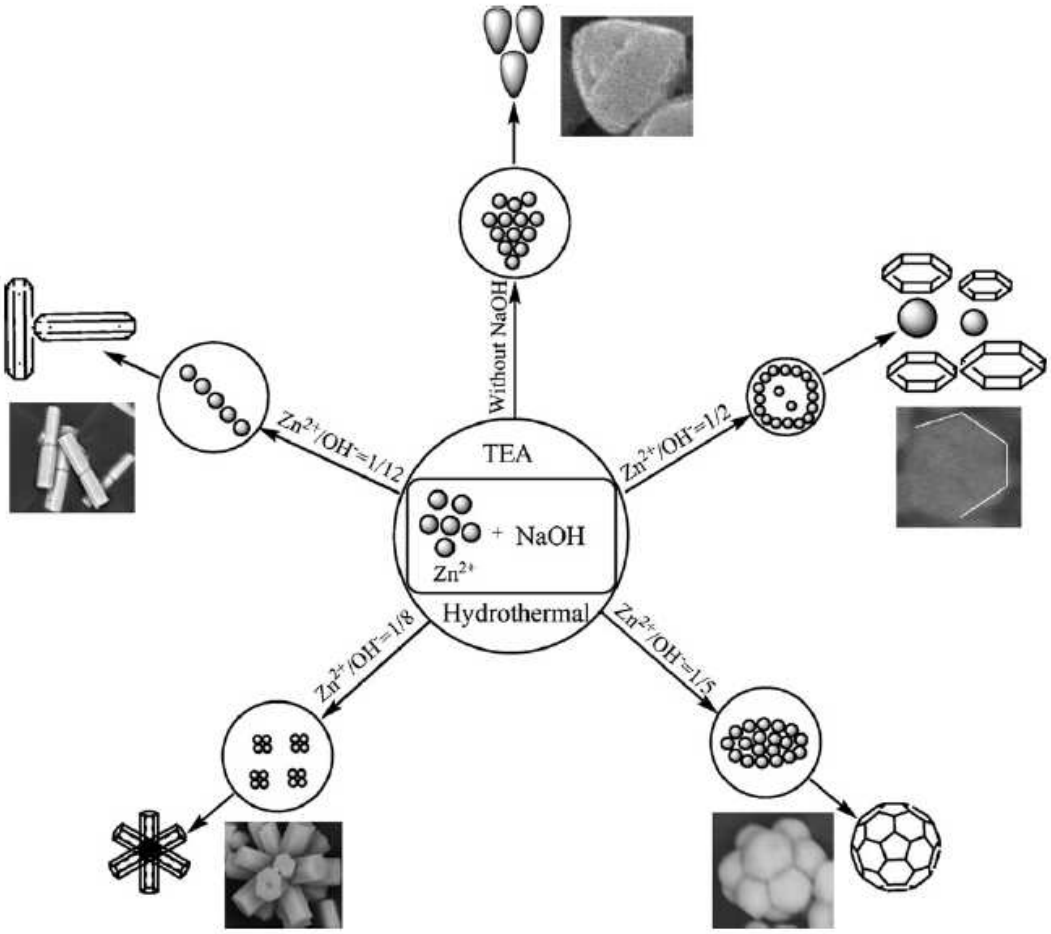

Fig. 8 Formation mechanism of ZnO microstructures (reprinted with permission from ref. 126; Copyright 2012 @ Elsevier).

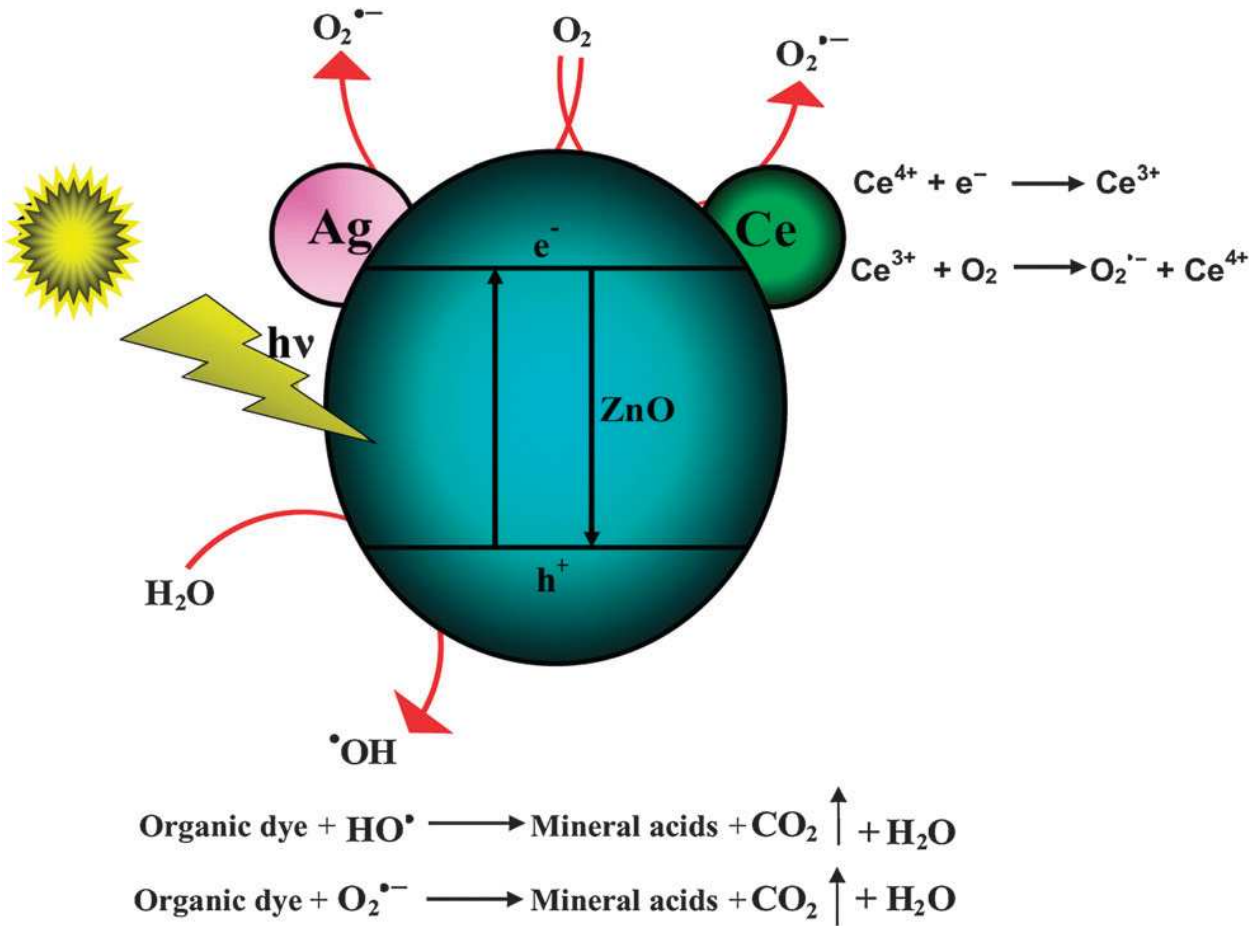

Fig. 9 Charge transfer pathways in Ce–Ag–ZnO (reprinted with permission from ref. 163; Copyright 2012 @ Royal Society of Chemistry).

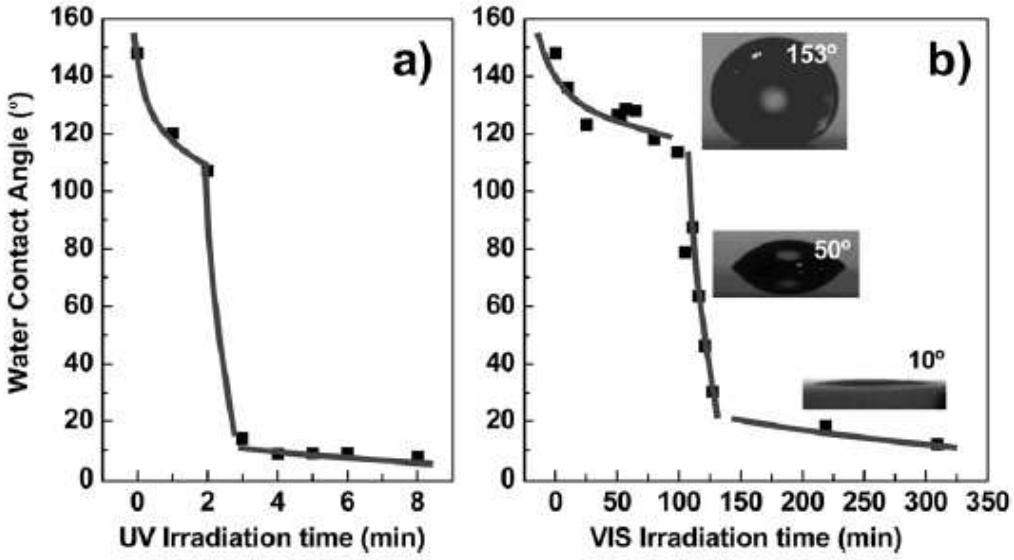

Fig. 10 Switching the Ag-ZnO surface from superhydrophobic to superhydrophilic under UV (a) and visible light (b) illumination (reprinted with permission from ref. 184; Copyright 2012 @ Royal Society of Chemistry).

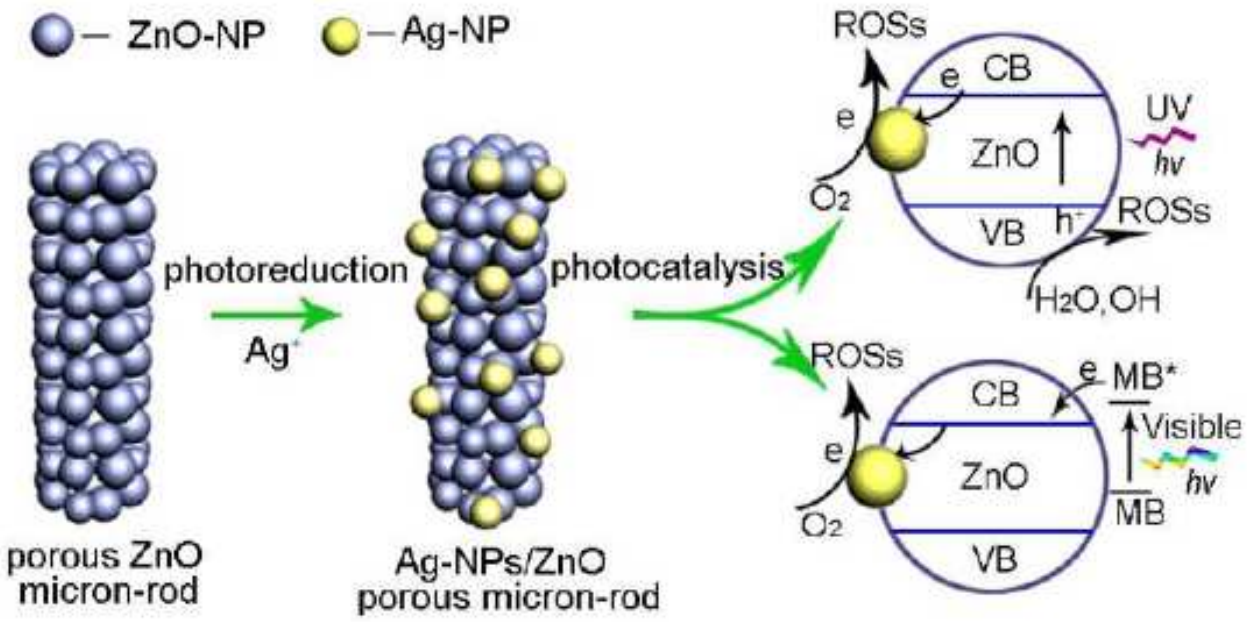

Fig. 11 Illustrating the process of MB degradation by using Ag -ZnO microrods under UV and solar light irradiation (reprinted with permission from ref. 185; Copyright 2012 @ American Chemical Society).

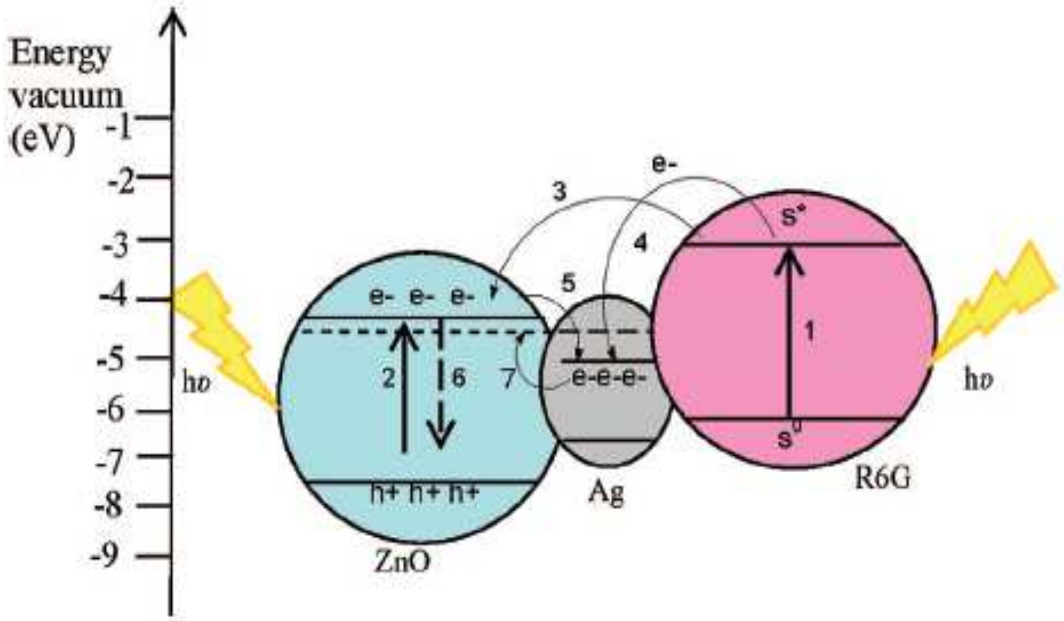

Fig. 12 Electron transfer events of Ag-ZnO system in presence of R6G; (1) an excitation of R6G from ground singlet to excited singlet; (2) bandgap excitation of ZnO to generate electron-hole pair; (3) a sensitized electron transfer from dye to ZnO CB; (4) sensitized electron migration from dye or Ag islands; (5) electron transfer from ZnO CB to Ag; (6) charge carrier recombination; (7) shifting of Fermi level of silver (reprinted with permission from ref. 192; Copyright 2008 @ American Chemical Society).

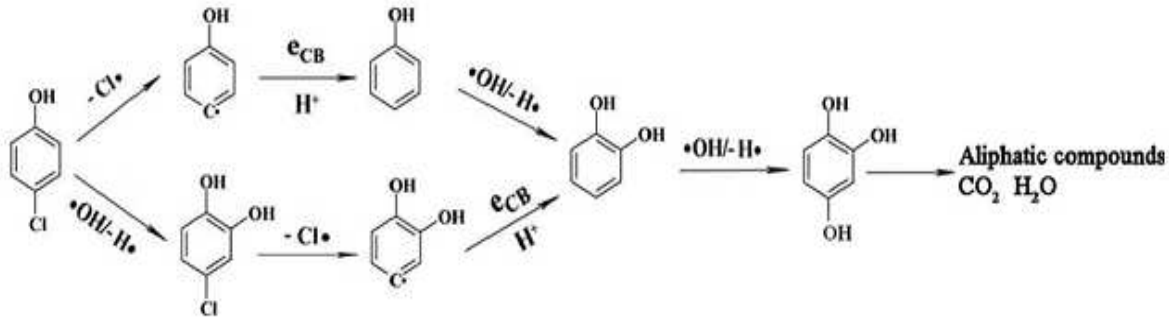

Fig. 13 Photodegradation pathways of 4-CP (reprinted with permission from ref. 204; Copyright 2009 @ American Chemical Society).

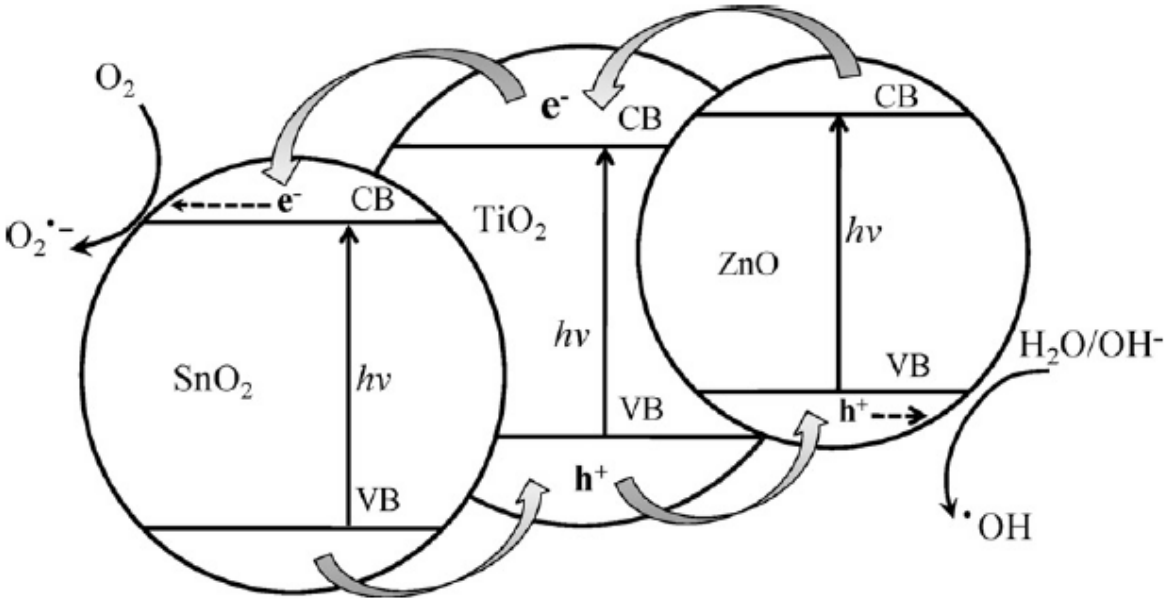

Fig. 14 Energy band structure and electron-hole separation process of tri-component SnO_2-TiO_2-ZnO system (reprinted with permission from ref. 227; Copyright 2012 @ Elsevier).

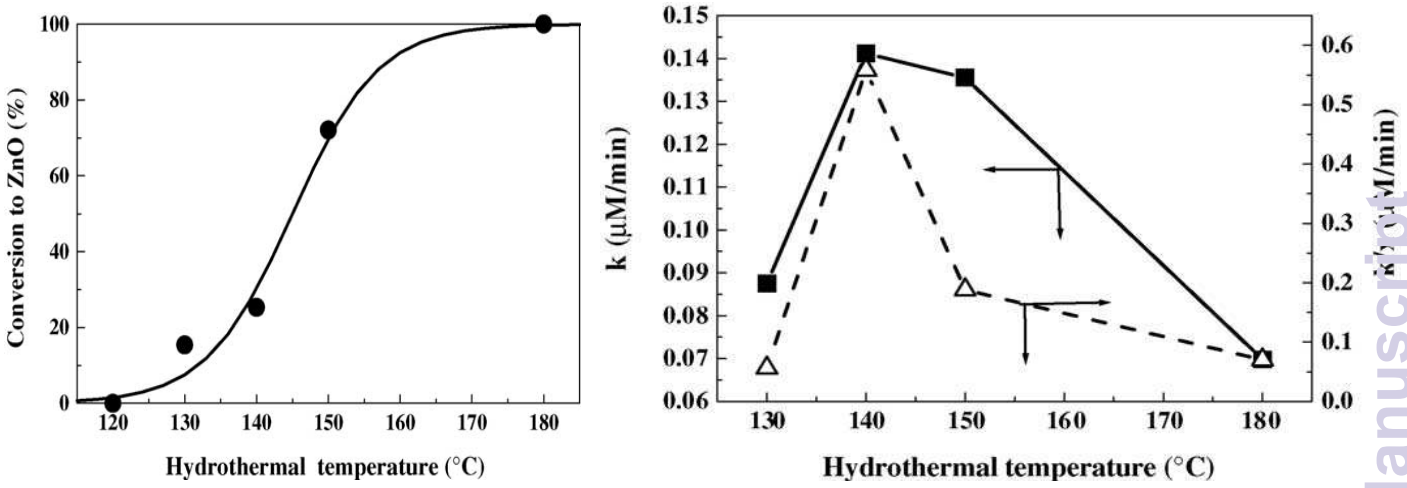

(a) **(b)**

Fig. 15 (a) Phase transformation from ZnO_2 to ZnO; (b) rate constant (k) and normalized rate constant (k/x) *vs* hydrothermal temperature (x is the ZnO_2-to-ZnO conversion) for MO degradation (reprinted with permission from ref. 242; Copyright 2005 @ Elsevier).

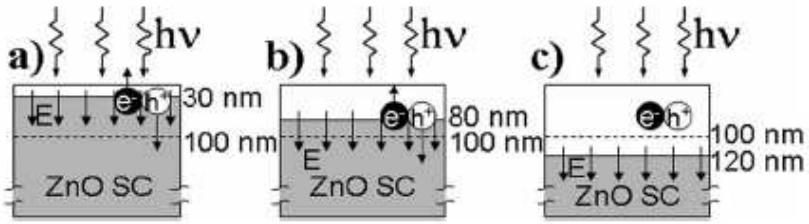

Fig. 16 The relationship between IEF and effective UV-light absorption layer (about 100 nm, from the surface to the dotted line), when the thickness of AZO TF is about (a) 30, (b) 80 and (c) 100 nm (reprinted with permission from ref. 249; Copyright 2011 @ Royal Society of Chemistry).

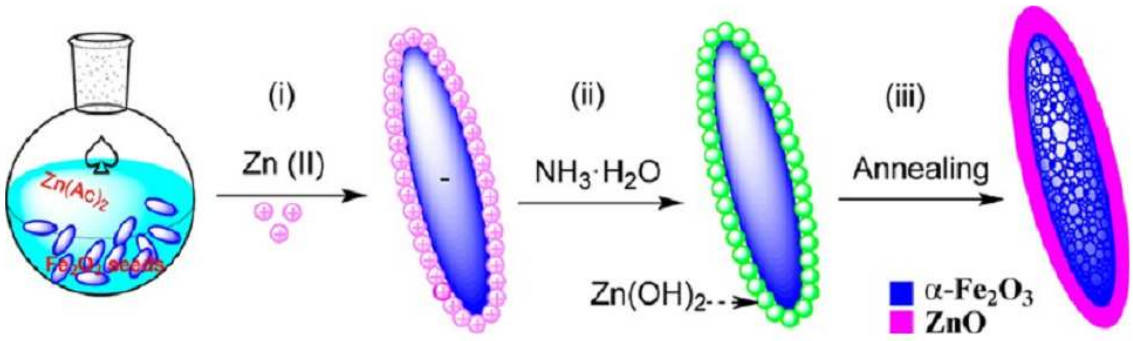

Fig. 17 Stepwise formation of Fe_2O_3@ZnO heterostructure; (i) adsorption of zinc species on hematite seeds; (ii) addition of ammonia to form $Zn(OH)_2$; (iii) the $Zn(OH)_2$ decomposes to form ZnO layer (reprinted with permission from ref. 253; Copyright 2012 @ American Chemical Society).

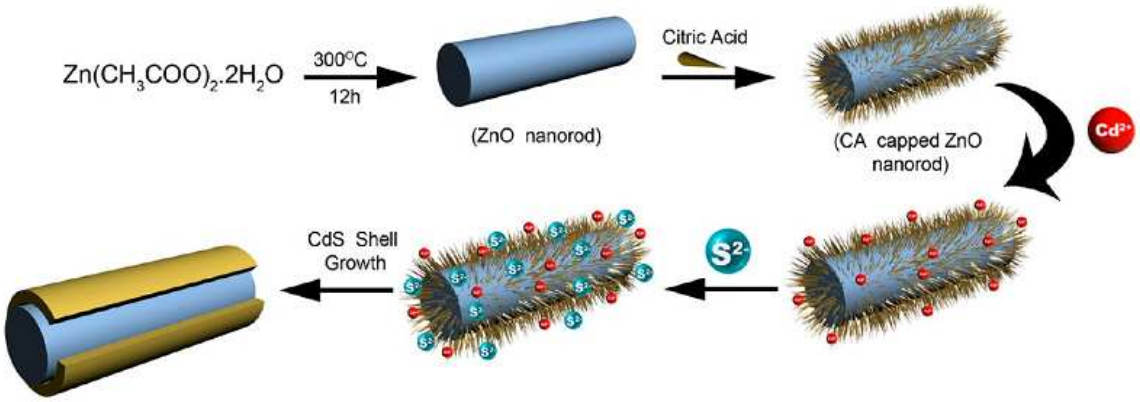

Fig. 18 Formation mechanism of ZnO-CdS core-shell nanorod arrays from surface-functionalization method (reprinted with permission from ref. 263; Copyright 2012 @ American Chemical Society).

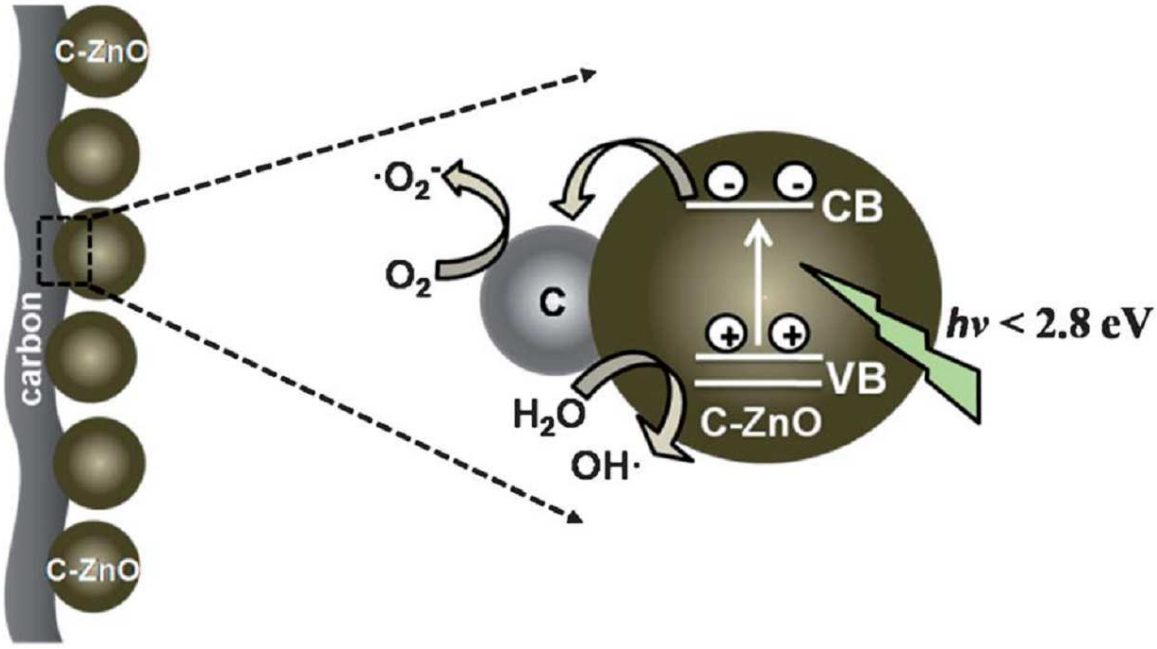

Fig. 19 The schematic presentation of doped and surface carbon in C–ZnO. The grey color part indicates that the polymer nanowires turned into carbon and olive color spheres represent C–ZnO (reprinted with permission from ref. 274; Copyright 2013 @ Royal Society of Chemistry).

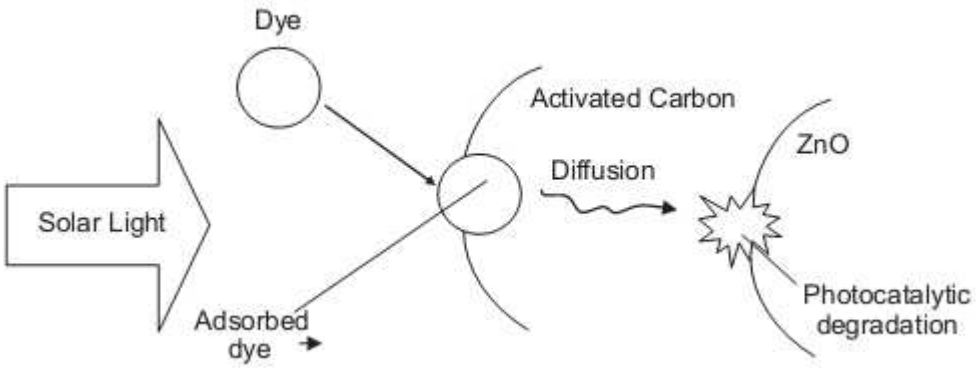

Fig. 20 Adsorption and diffusion of dye molecules towards ZnO and their degradation (reprinted with permission from ref. 279; Copyright 2007 @ Elsevier).

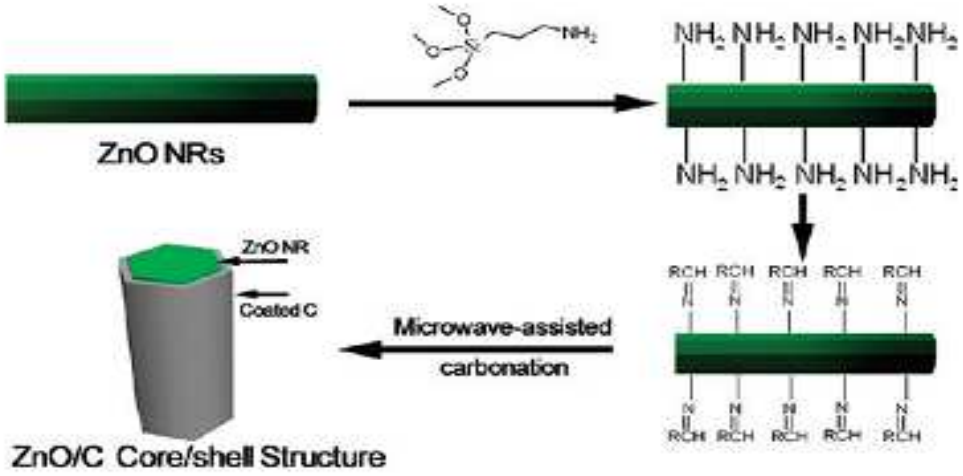

Fig. 21 Formation mechanism of carbon coated ZnO core-shell structure (reprinted with permission from ref. 280; Copyright 2009 @ American Chemical Society).

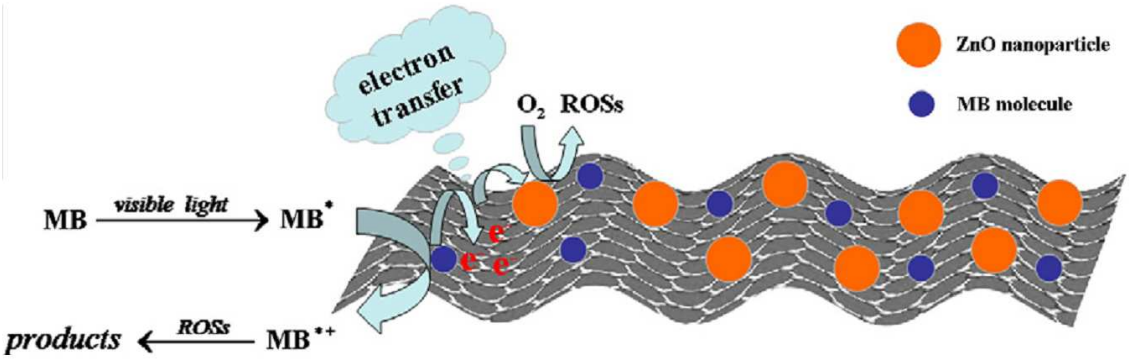

Fig. 22 Photosensitized degradation of MB over ZnO-GO under visible light (reprinted with permission from ref. 289; Copyright 2012 @ Elsevier).

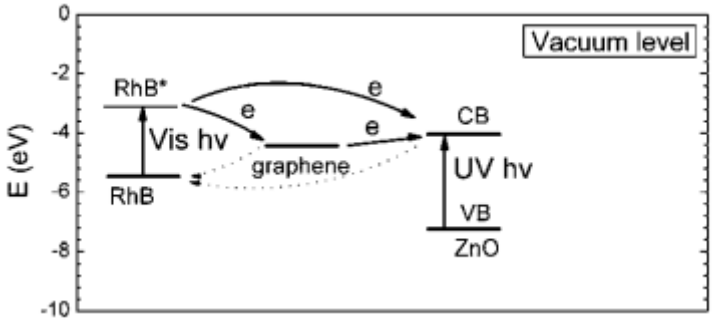

Fig. 23 Charge transfer mechanism for ZnO-graphene sensitized by dye molecule (reprinted with permission from ref. 290; Copyright 2011 @ Royal Society of Chemistry).

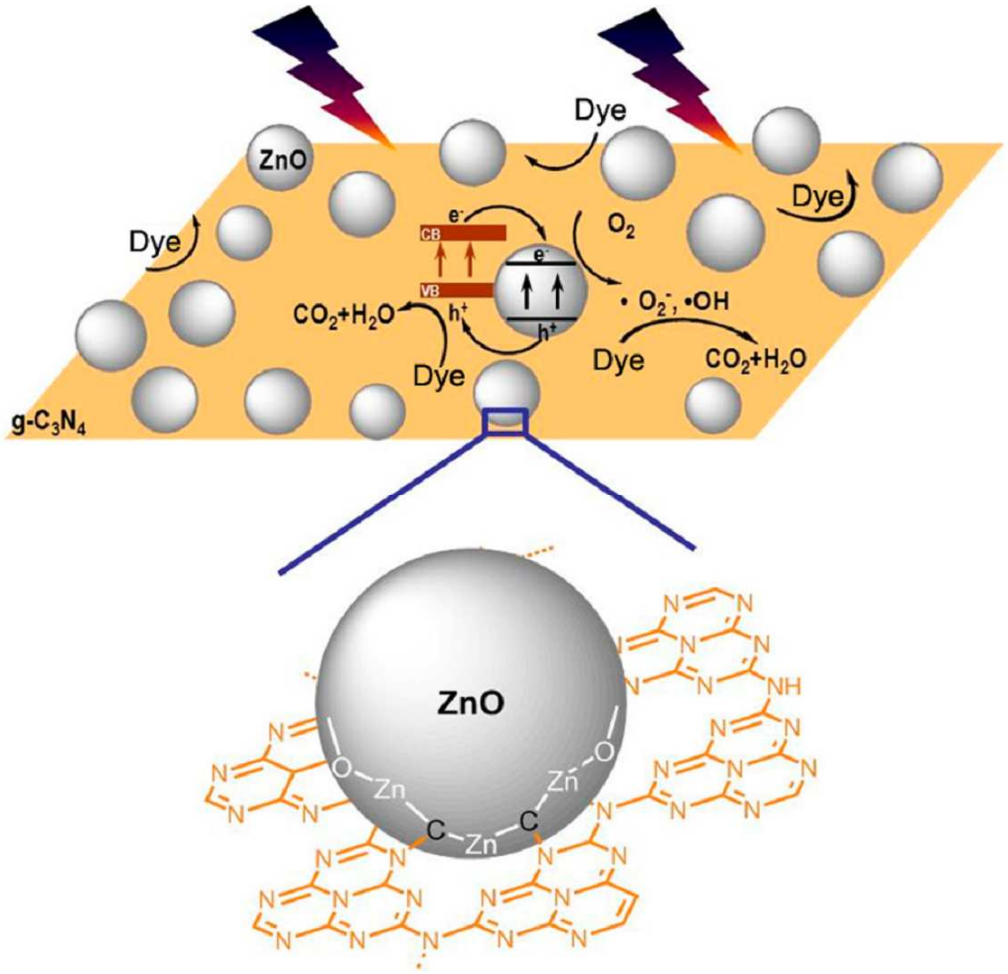

Fig. 24 Illustrating the electron−hole separation, transport, and photocatalytic progress of the C-ZnO:g-C_3N_4 under visible light (reprinted with permission from ref. 310; Copyright 2014 @ American Chemical Society).

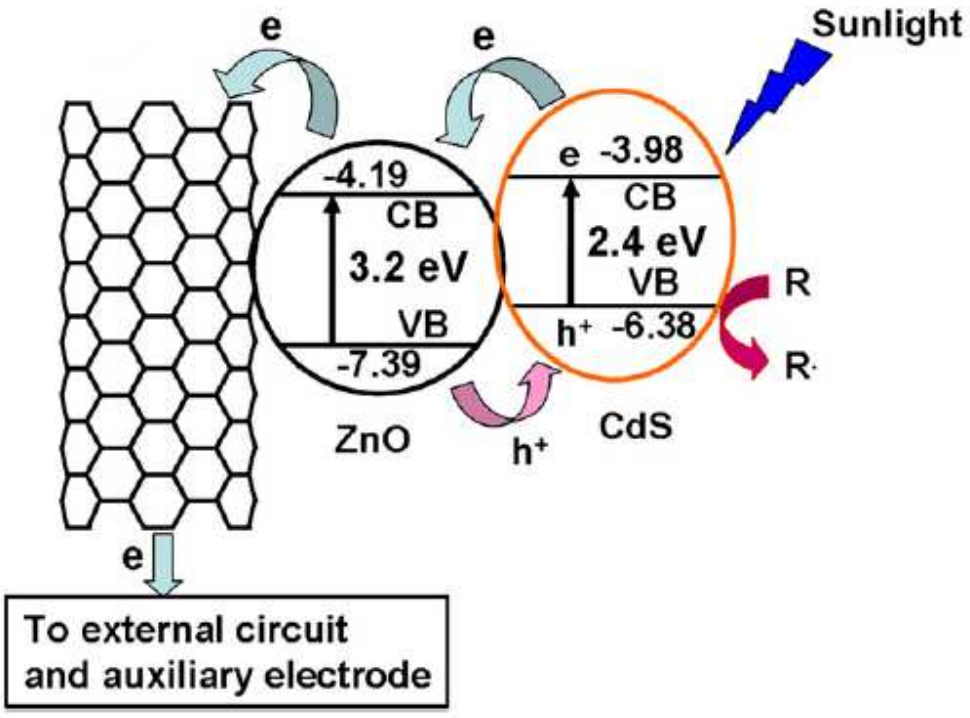

Fig. 25 Charge carrier separation and transportation in CdS-ZNWs-MWCNTs heterojunction (reprinted with permission from ref. 311; Copyright 2011 @ Elsevier).

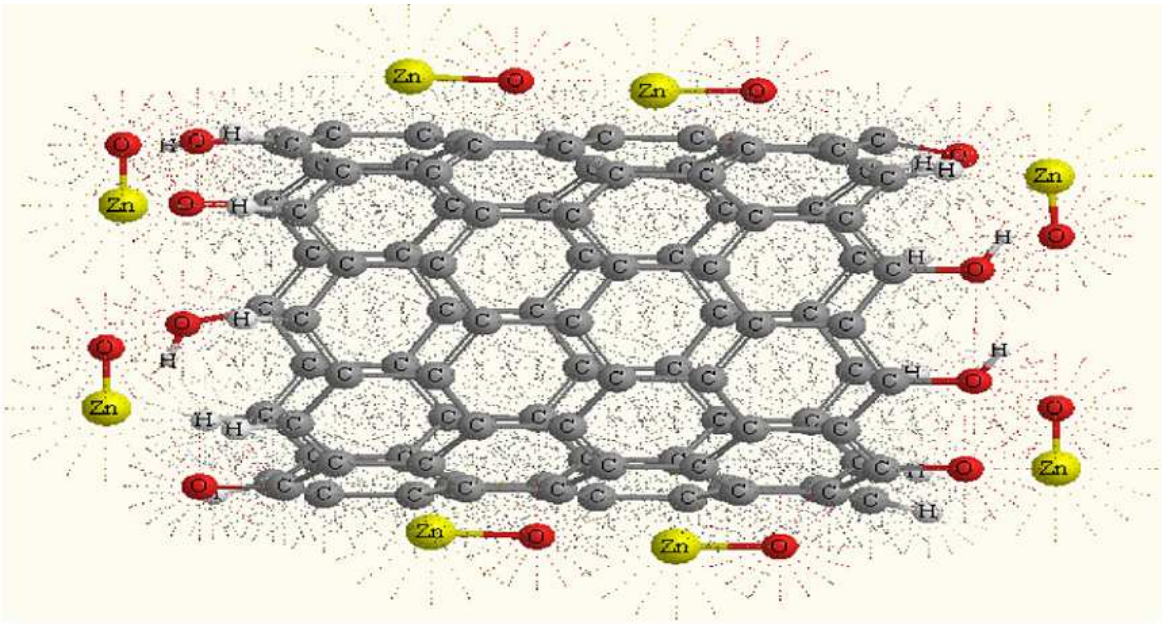

Fig. 26 Ball and stick representative diagram of MWCNT-ZnO composite (reprinted with permission from ref. 313; Copyright 2010 @ IOP Science).

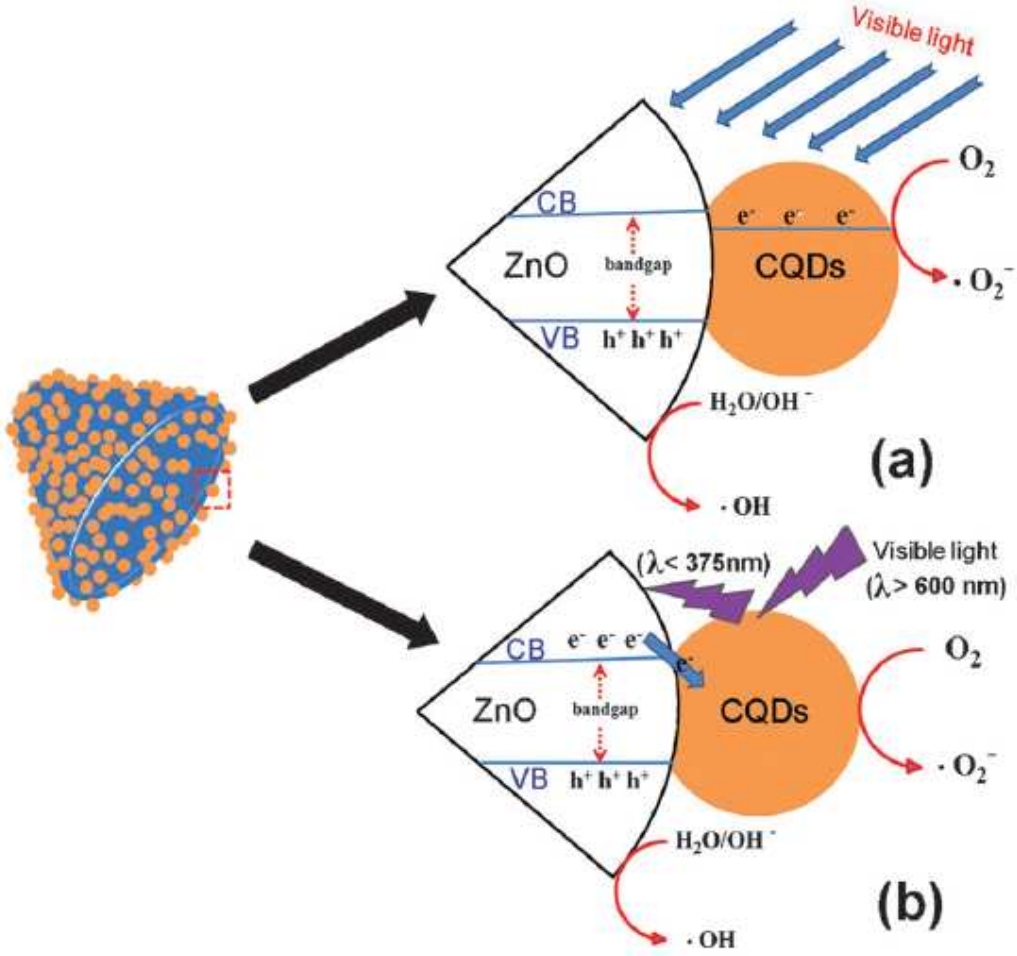

Fig. 27 Photocatalytic process of ZnO-CQDs under visible light (reprinted with permission from ref. 323; Copyright 2012 @ Royal Society of Chemistry).

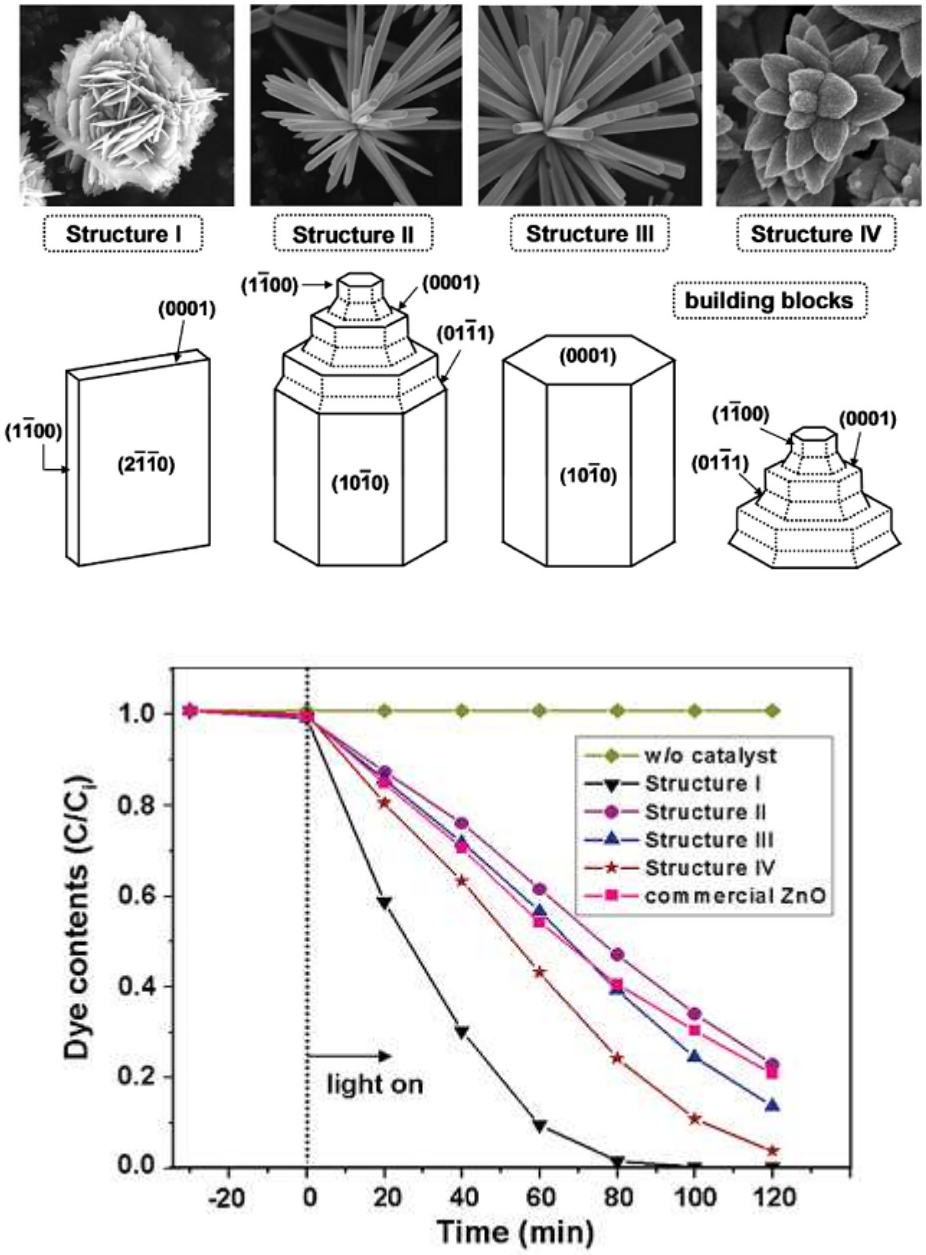

Fig. 28 The 3D ZnO superstructures with their building blocks and their photocatalytic activity (reprinted with permission from ref. 338; Copyright 2010 @ American Chemical Society).

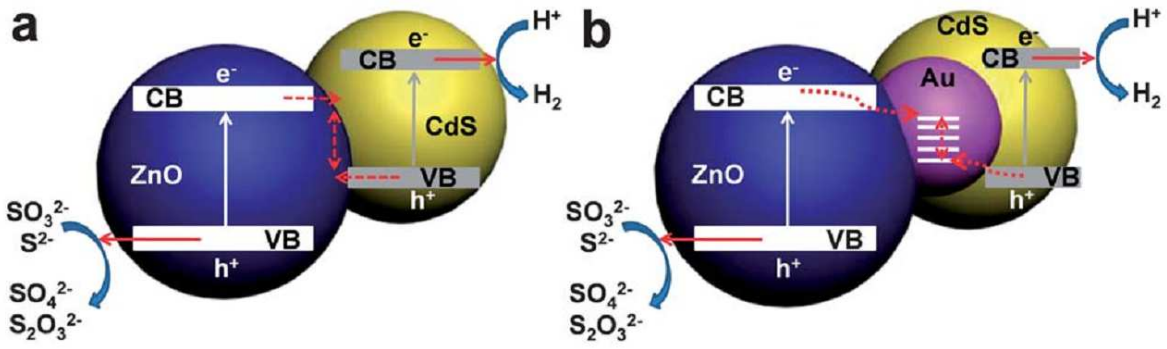

Fig. 29 Schematic presentation: (a) the direct Z-scheme charge-carrier transfer process in the CdS-ZnO and (b) the vectorial Z-scheme charge-carrier transfer process in the CdS-Au-ZnO (reprinted with permission from ref. 344; Copyright 2013 @ Royal Society of Chemistry).

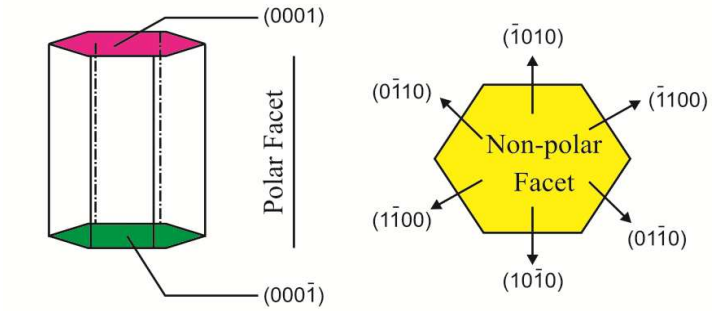

Exposed facets

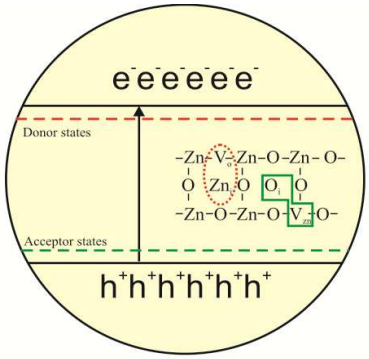

Defects rich ZnO

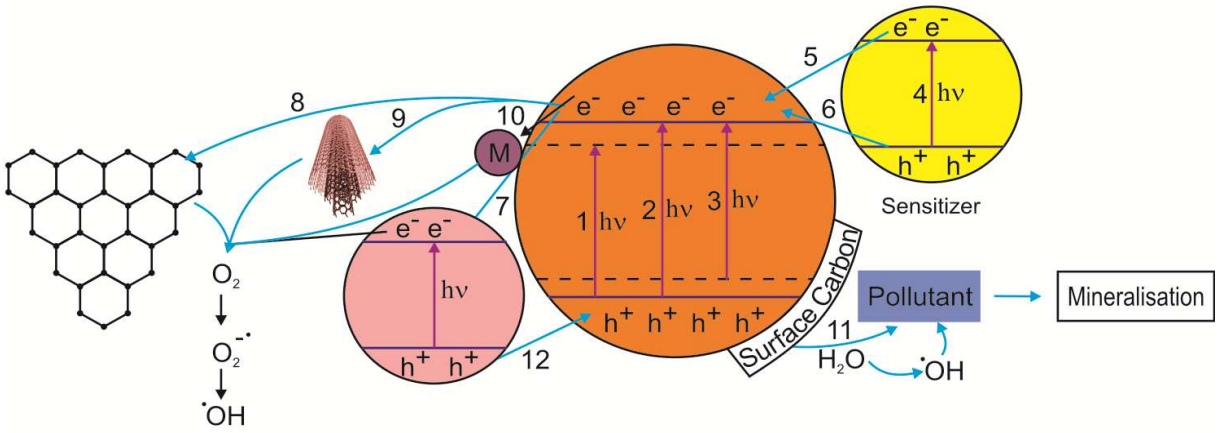

Surface - Bulk modifications of ZnO

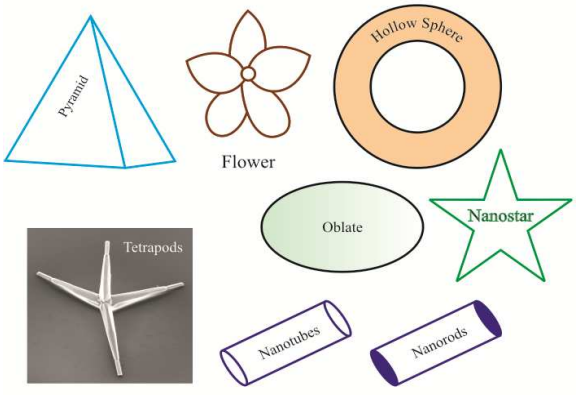

Hierarchical morphology

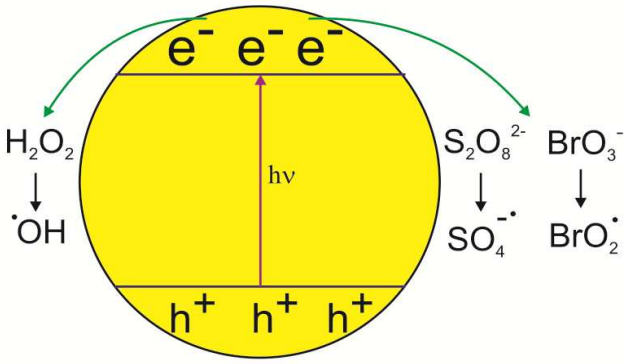

Addition of electron acceptors

Fig. 30 Overall view of ZnO based photocatalysis. The scheme at the four corners is reactive facets (top left), intrinsic defects (top right), nanostructured morhopology (bottom left) and generation of free radicals with electron acceptors (bottom right). The centre image represents the charge transfer pathways in the surface-bulk modification of zinc oxide that are reported to improve the photoactivity.

Path 1-excitation from VB to dopant level (metal ions);

Path 2-bandgap excitation of ZnO;

Path 3: excitation from impurity level (nitrogen or carbon doping) to CB;

Path 4: excitation of sensitizer (for instance, CdS, CuS, g-C_3N_4, inorganic complexes);

Path 5: transfer of excited electrons to ZnO CB;

Path 6: direct excitation of electron from sensitizer to CB of ZnO (as observed in surface complex formation between 4-CP and ZnO);

Path 7&12: transfer of electrons and holes in bicomponent system (for instance ZnO-SnO_2);

Path 8-10: electron trapping from graphene, MWCNTs and metal islands on ZnO surface respectively;

Path 11: surface carbon enriches pollutant adsorption on ZnO surface, facilitating direct attack of hole or hole oxidizes water molecules to generate hydroxyl radicals.